2020

Modeling Volcanic Ash Particle Impingement In The Hot Sections Of A Gas Turbine Engine

Drue Seksinsky
University of Vermont

MODELING VOLCANIC ASH PARTICLE IMPINGEMENT IN THE HOT SECTIONS OF A GAS TURBINE ENGINE

A Thesis Presented

by

Drue Seksinsky

to

The Faculty of the Graduate College

of

The University of Vermont

In Partial Fulfillment of the Requirements
for the Degree of Master of Science
Specializing in Mechanical Engineering

August, 2020

Defense Date: April 23, 2020
Thesis Examination Committee:

Jeffrey S. Marshall, Ph.D., Advisor
Clelia L. Marti, Ph.D., Chairperson
William Louisos, Ph.D.
Cynthia J. Forehand, Ph.D., Dean of the Graduate College

ABSTRACT

A computational study was conducted of axisymmetric droplet impingement on a flat surface at low droplet Reynolds numbers. The study was motivated by deposition of melted volcanic ash particles within gas turbine engines, which can pose significant safety risk for jet aircraft encountering volcanic ash clouds. The computations were performed using the combined level-set volume-of-fluid method for Reynolds numbers Re in range $0.05 \leq Re \leq 10$, typical of volcanic ash impingement problems. Computational results were compared to typical assumptions for approximate droplet impact models at high Reynolds number. The computational predictions were validated using existing experimental data. The computations indicate that contact radius increases over short time in proportion to the square root of time, in agreement with short-time analytical predictions. The droplet shape was well approximated by a truncated spherical cap, which spread on the substrate surface an increasing amount as Re was increased. The axial velocity component was approximately independent of radius over most of the droplet, and the radial velocity component was observed to vary log-normally with axial distance. The dissipation rate was distributed throughout the droplet for low Reynolds numbers cases, but became increasingly localized near the contact line as the Reynolds number increased past unity.

ACKNOWLEDGEMENTS

I would like to thank my advisor Jeffrey Marshall. Without his guidance or expertise this research could not have been completed. Your teaching style was consistently challenging and rewarding and drove me toward success. Because of your mentorship I am leaving UVM with a passion for fluid mechanics and computational methods, and the skills to succeed in whatever comes next.

I appreciate the effort put forth by my committee members William Louisos and Clelia Marti. I know serving on a committee is a time-consuming task and I appreciate your willingness to do so for me. Your comments and questions were invaluable.

To my mom Arlene, thank you for the constant support. The groceries, dinner outings, and frequent phone calls helped me through the process of this Master's degree. None of this would have been possible without you. I couldn't have asked for a better mom.

And finally thank you to Cora and Bailey. The two of you were truly bonedogs through this whole experience.

Funding for this work has been provided by a Vermont NASA EPSCoR/Vermont Space Grant Graduate Fellowship grant NNX15AK55A

TABLE OF CONTENTS

Page

LIST OF TABLES

Table Page

LIST OF FIGURES

Figure Page

CHAPTER 1

INTRODUCTION

1.1. Motivation

During the 21st century there has so far been 18 major volcanic eruptions around the world, and during the 20th century there were 64 major volcanic eruptions, all classified as a four or higher on the Volcanic Explosivity Index (VEI). The VEI is a logarithmic scale describing the destructive power of an eruption based on criteria such as amount of ejected material, height of ejected ash cloud, and impact on infrastructure. Volcanic eruptions release lava, gases, and tephra. Tephra is a generic term for fragmented material released during an eruption, including ash. Ash particles released during an eruption can have a wide range of size and composition. For example, the Eyjafjallajökull volcano in Iceland emitted large ash clouds containing particles ranging in size from 1-100 micrometers (Dacre et al., 2013). Small particles can remain suspended in the atmosphere for weeks and can travel many hundreds of kilometers from the volcanic source. Figure 1.1 shows a schematic of volcanic ash deposition and sedimentation. Larger particles tend to settle out closer to the source eruption and not remain suspended long, while smaller particles can be transported thousands of kilometers in the atmosphere over the course of several weeks.

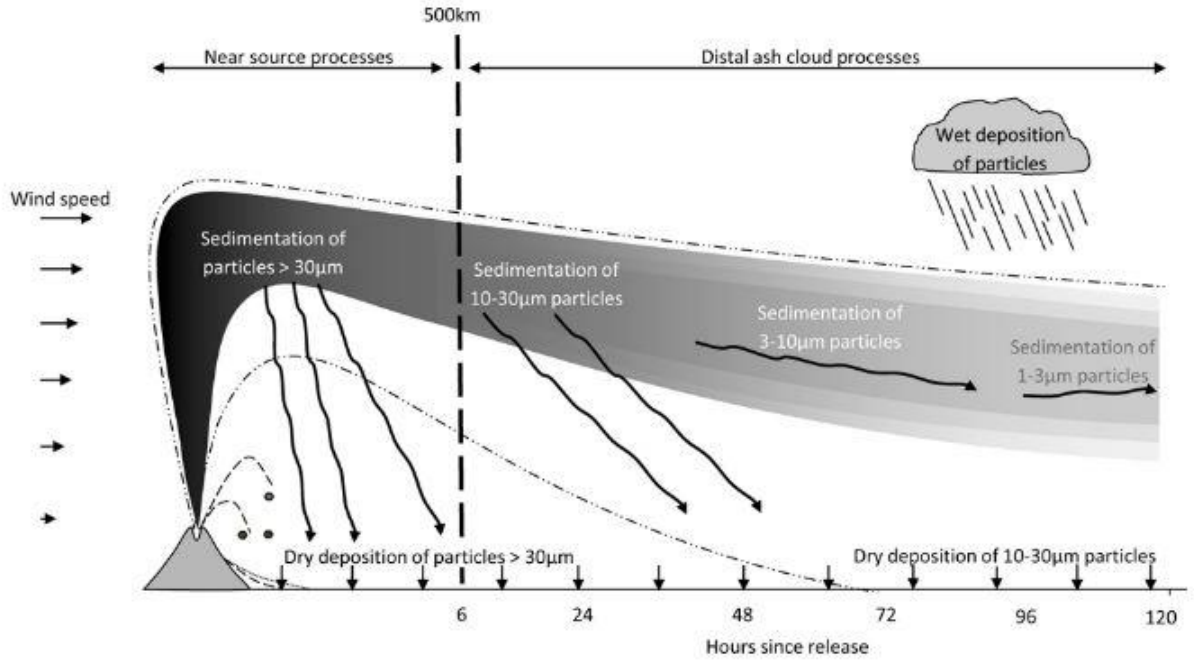

Figure 1.1: Volcanic ash and sedimentation and deposition after a volcanic event. The grey scale indicates the concentration of the ash. The x-axis simultaneously shows the time after the eruption and the distance from the source. The y-axis shows the height of the ash cloud after eruption. Near source eruption process are defined as six hours after the eruption and 500 kilometers from the source. Reproduced from Ojovan (2008).

Approximately nine percent of the world's population lives within 100 kilometers of an active volcano (Horwell & Baxter, 2006). Particle size and concentration in ash clouds decay exponentially with distance from the volcanic source (Pyle, 1989). Ash deposits can negatively impact residential homes, agricultural land, municipalities, and aircraft infrastructure located at large distances from the volcanic source (Wilson et al., 2012). Roughly one-fifth of airports world-wide are located within 500 kilometers of an active volcano (Guffanti et al., 2009). Ingestion of volcanic ash particles into aircraft gas

turbine engines at high particle concentrations and over long exposure times can cause significant engine damage (Dunn, 2012). Between the years of 1953 and 2009, over one-hundred incidents of airplanes flying through volcanic ash clouds have been recorded, including 26 incidents resulting in severe damage (Guffanti et al., 2010). Nine of these incidents resulted in total engine failure. Additional related incidents have occurred with entrainment of small sand particles into gas turbine engines, which is particularly problematic for military aircraft operating in desert locations.

Volcanic ash is primarily composed of silicon dioxide (SiO_2) and is considered an amorphous solid (Chen & Zhao, 2015). Amorphous solids have the unique characteristic that their viscosity depends logarithmically on temperature. The Vogel-Fulcher-Tammann (VFT) equation models the logarithmic temperature dependence of viscosity well. When amorphous, or glassy, solids experience a large temperature change the viscosity of the substances rapidly changes, and can vary anywhere from 10^{24} to $10^{-4.6}$ (Angell, 1991, 1996; Russell et al., 2003). The rapid change in the viscosity leads to a rapid change in the mechanics of the material. For instance, an amorphous solid at a relatively low temperature will resist shear and exhibit constitutive behavior more similar to an elastic solid. If the same material experiences the same shear, but at much higher temperature, the reaction will be different. The material may instead be prone to plastically deforming, or undergoing continuous deformation like a fluid (Ojovan, 2008). An aircraft gas turbine engine (GTE) may have a temperature peak as high as 2000 ºC, which is high enough to cause volcanic ash to heat past its melting point (Giordano et al.,

2008; Song et al., 2016). This melting will lead to adhesion and deposition of material on the surfaces inside of the GTE (Chen & Zhao, 2015; Taltavull et al., 2016).

Engine damage from ingestion of small volcanic ash and sand particles is of two types. The first occurs due to erosion of compressor blades by collision with solid particles traveling at high speeds, as shown in figure 1.2 (Chen & Zhao, 2015; Dunn, 2012; Taltavull et al., 2016).

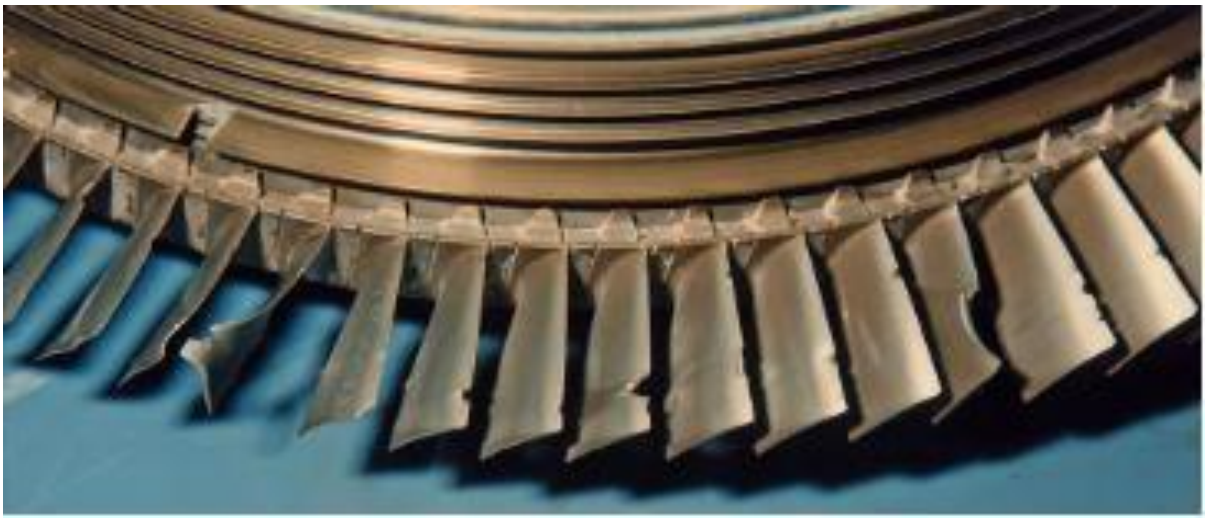

Figure 1.2: Damage done to the ninth stage compressor blades of a P/W F100 engine, S/N P580043. The engine was subjected to continuous feeds of dust for varying particle size distributions and concentrations. The average particle size feed into the engine was 37 microns. Reproduced from Dunn (2012).

The particle-induced erosion will cause significant change in the shape of the compressor blade, leading to reduced blade efficiency. Particles passing through the engine combustion section are exposed to high temperatures, with turbine inlet temperature often in excess of 1000 °C Song et al. (2016). Exposure to high temperatures causes an ash

particle to become soft, leading either to material sintering or melting into a highly viscous liquid droplet (Song et al., 2016). The second type of GTE damage is due to deposition of molten ash material on the hot section components of the engine, including plugging of film cooling channels and deposition on turbine nozzle guide vanes, shown in figures 3 and 4 (Bonilla, 2012; Walsh et al., 2006). Upon impact on a downstream surface, a melted particle spreads on the surface while exchanging heat with the underlying substrate. The melted particle will eventually reach an equilibrium resting state driven by the balance of surface tension and viscous forces, while at the same time the droplet is cooling via contact with the substrate. This process results over time in formation of a glassy deposit on the turbine nozzle blades and guide vanes, which can plug film cooling holes and cause cracking of ceramic coating used for heat protection of hot section components (Chen & Zhao, 2015).

It has been shown that particles larger than 100 microns in diameter are less likely to melt and adhere upon a collision, while particles less than approximately three microns in diameter are unlikely to collide with any surface at all (Dunn, 2012). The primary area of interest, in terms of melting and colliding potential, is particles with diameters in the range 10-30 microns and is shown in figure 1.3 (Taltavull et al., 2016).

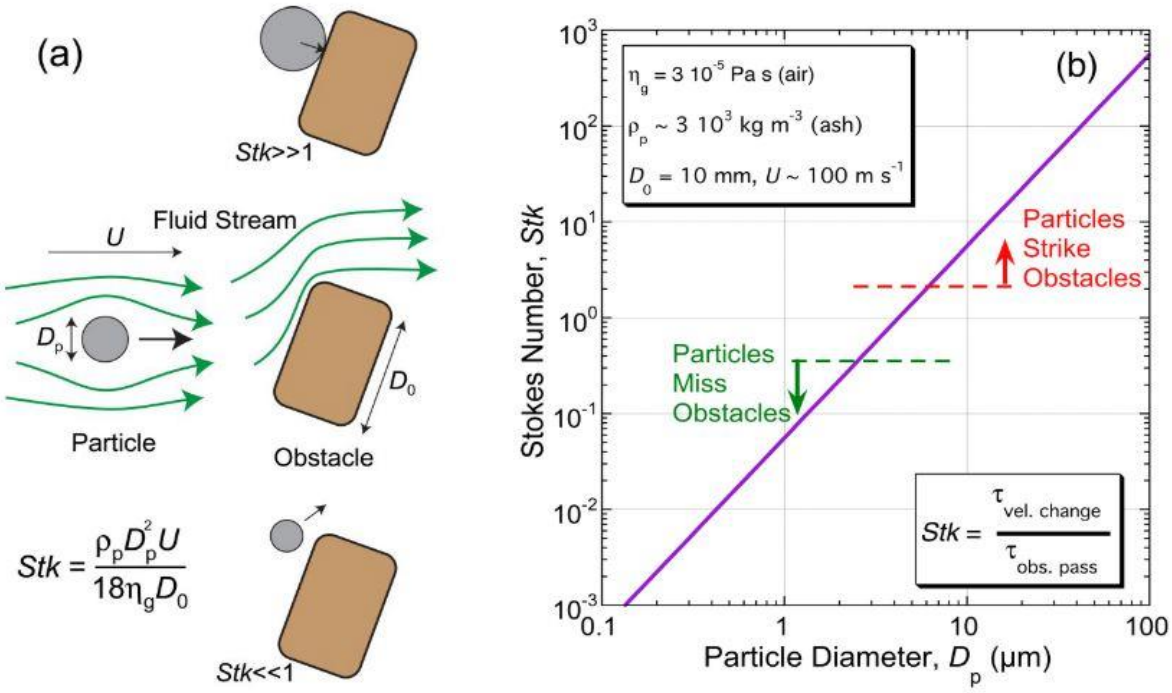

Figure 1.3: (a) A diagram of how a spherical particle, with some diameter D_p, may collide with a solid object, with a characteristic length scale D_o. The particle is advected by a velocity U in a carrier fluid, in this case air. The particle density and carrier fluid viscosity are given by ρ_p and η_g, respectively. In this figure, both (a) and (b), Stk refers to the stokes number between the particle and carrier fluid. (b) Is the calculated stokes number assuming values for the, particle density, characteristic length scale, and velocity, with varying particle diameters. Reproduced from Taltavull et al. (2016).

When softened, or molten, volcanic ash particles that collide with turbine blades will adhere and spread out on the impacting surface. The turbine blades feature cooling holes which are necessary to keep the blades at a safe operating temperature. If the film cooling holes become blocked by deposited material, they can no longer supply sufficient heat transfer, effectively not performing the task for which they were designed. Without sufficient heat transfer the blade will melt and completely fail, as seen in figure 1.4.

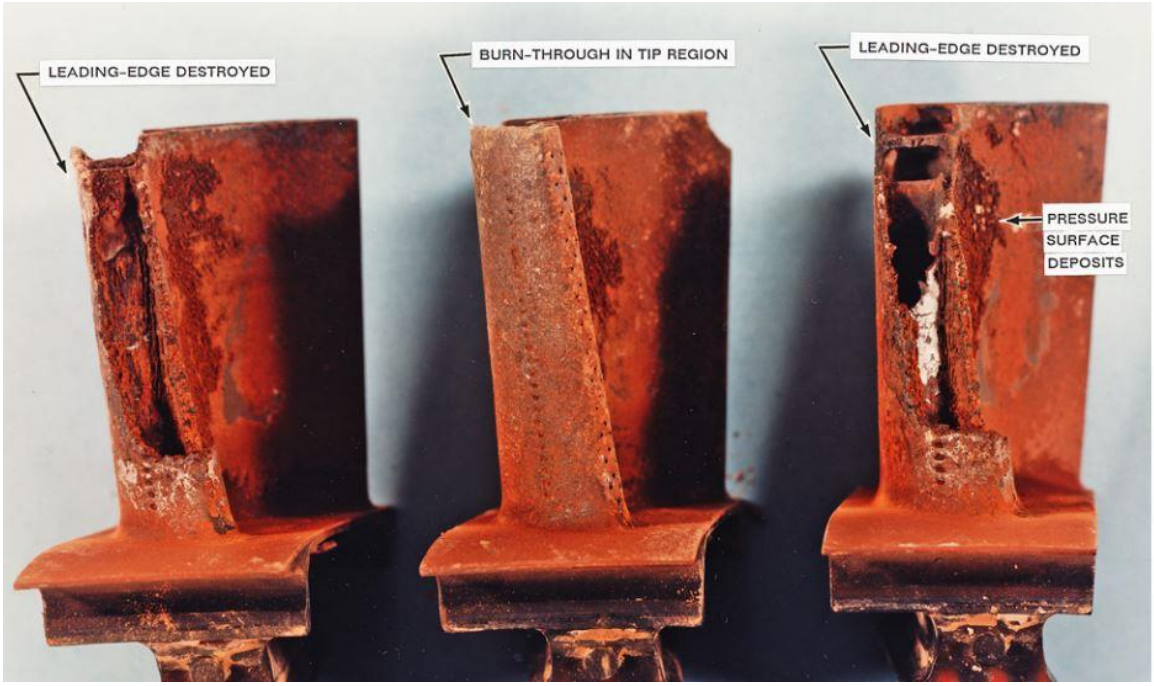

Figure 1.4: Image of turbine blades after exposure to continuous dust feed. Reproduced from Dunn (2012).

There are similar concerns for the turbine guide vanes. When material adheres to the vanes by impingement of molten ash particles, as shown in figure 1.5, the heat transfer ability of the blade is changed.

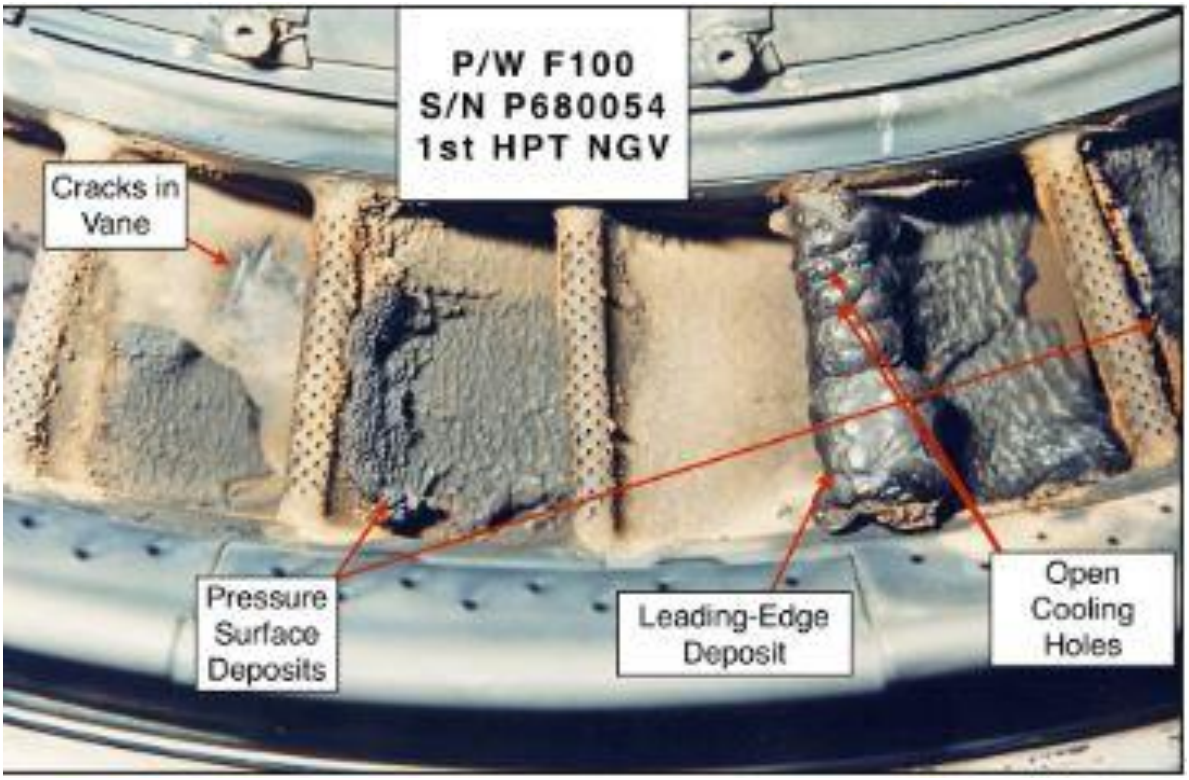

Figure 1.5: Volcanic ash material that has been melted and deposited on the turbine vanes of a GTE. Reproduced from Dunn (2012).

Cracking and degradation of thermal barriers applied to the vanes becomes a significant issue due to the buildup of material (Chen & Zhao, 2015). Another concern for turbine guide vanes is that significant material buildup will decrease the lift on the blades and degrade turbine efficiency. A decrease in efficiency will force the GTE compressor to work harder, resulting in decreased service or even engine stall.

The volcanic ash deposition problem discussed above is associated with the broader topic of droplet impingement, which is important for a wide variety of applications, such as thermal spray coating (Alavi et al., 2012; Bertagnolli et al., 1994),

inkjet printing (Lim et al., 2009; van Dam & Le Clerc, 2004), agriculture (Wirth et al., 1991), droplet erosion on turbine blades (Zhou et al., 2008), icing of airfoils (Antonini et al., 2011; Mishchenko et al., 2010) and others. The physics of droplet impingement have been extensively investigated over several decades, as discussed in detail in the Literature Review chapter of this thesis. However, nearly all research on droplet impingement has considered cases where the droplet Reynolds number is large compared to unity. By contrast, the problem of molten volcanic ash particle impingement in gas turbine engines is a small Reynolds numbers process, due to the high viscosity and small diameter of the droplets. Many of the assumptions used in theoretical models of droplet impingement at high Reynolds numbers may not be valid for low Reynolds numbers. Therefore, there is a need for expanding the existing body of research on droplet impingement to cover low Reynolds number impingement problems. In particular, as has been discussed above, melted volcanic ash particles pose a significant danger to aviation safety and equipment through adhesion and deposition in gas turbine engines. An improvement in our ability to predict this damage by an improved understanding of the droplet impingement problem under appropriate parameter values is a critical concern.

1.2. Objectives and Scope

This thesis examined the impact and spreading of fluid droplets on a flat surface under parametric values typical of volcanic ash passage through an aircraft gas turbine engine. In particular, this research differed from the existing body of research on droplet

impingement in that it is primarily concerned with problems of low Reynolds number droplet impingement and associated modeling.

To model the spreading process of volcanic ash inside of a gas turbine engine, two preliminary analyses were completed. The analyses completed were done to determine significance of heat transfer during the droplet spreading process and the uniformity of the fluid temperature for a melted volcanic ash particle. After the preliminary analyses were completed, a computational fluid dynamics model was developed for an axisymmetric droplet impingement onto a flat surface at low droplet Reynolds number. The model used a coupled level-set volume-of-fluid (CLSVOF) solver to simulate the liquid and gas phases. The simulated solutions were used to assess the validity at low Reynolds numbers of various assumptions typically used for theoretical modeling of droplet impingement at higher Reynolds numbers, including droplet shape, dissipation rate field, and velocity profiles during droplet impact.

The layout of this thesis is as follows. Chapter 2 gives a literature review covering volcanic ash material properties, a discussion of previous work on droplet impingement, and experimental and numerical studies done on volcanic ash ingestion into gas turbine engines. Chapter 3 covers the thermal assessments used to justify the simulation setup. Chapter 4 details the computational method used for direct numerical simulations of droplet impingement. Chapter 5 assesses the results of the droplet impingement simulations, examining the energetics of the droplet by looking at the local kinetic energy, potential energy, and dissipation rates during the collision. The computations are validated using previous experimental data. Conclusions are presented in Chapter 6,

including discussion of how low Reynolds number droplet impingement differs from the more widely studied high Reynold's number cases and the significance of these differences for modeling of volcanic ash passage through gas turbine engines.

CHAPTER 2

LITERATURE REVIEW

This literature review discusses background information necessary to understand volcanic ash interactions with solid surfaces under conditions relevant to GTEs. Section 2.1 discusses the material properties of volcanic ash, including viscosity and thermal properties as functions of temperature and ash chemical composition. Section 2.2 provides background on the problem of droplet impingement onto a flat surface, including an overview of the physics of a droplet collision, regime mapping, a more detailed discussion of experimental and numerical results for droplet collision. Section 2.3 covers droplet solidification, including an in-depth review of droplet adhesion and solidification inside of GTEs. Relevant material on droplet solidification and adhesion in thermal spray coating applications are also discussed.

2.1. Volcanic Ash Material Properties

2.1.1. Volcanic Ash Viscosity

Viscosity is one of the most important transport properties of a fluid. The viscosity of molten volcanic ash can span 15 orders of magnitude or more, with variations largely due to differences in temperature and composition. Molten volcanic ash is derived from liquid magma, which is composed of a mixture of silicon dioxide (SiO_2) and a wide range of secondary suspended substances (Hobiger et al., 2011). When

discussing the material properties of volcanic ash, whether its thermal, viscous, or any other property, the composition is important.

Vogel et al. (2017) is one of only a few studies to present a systematic and extensive evaluation of a large set of widely varying volcanic ash samples. The study characterized the composition, optical features, and density of various volcanic ash samples. Figure 2.1 depicts a phase plot of the percent weight of SiO_2 and alkali oxides with varying volcanic ash samples.

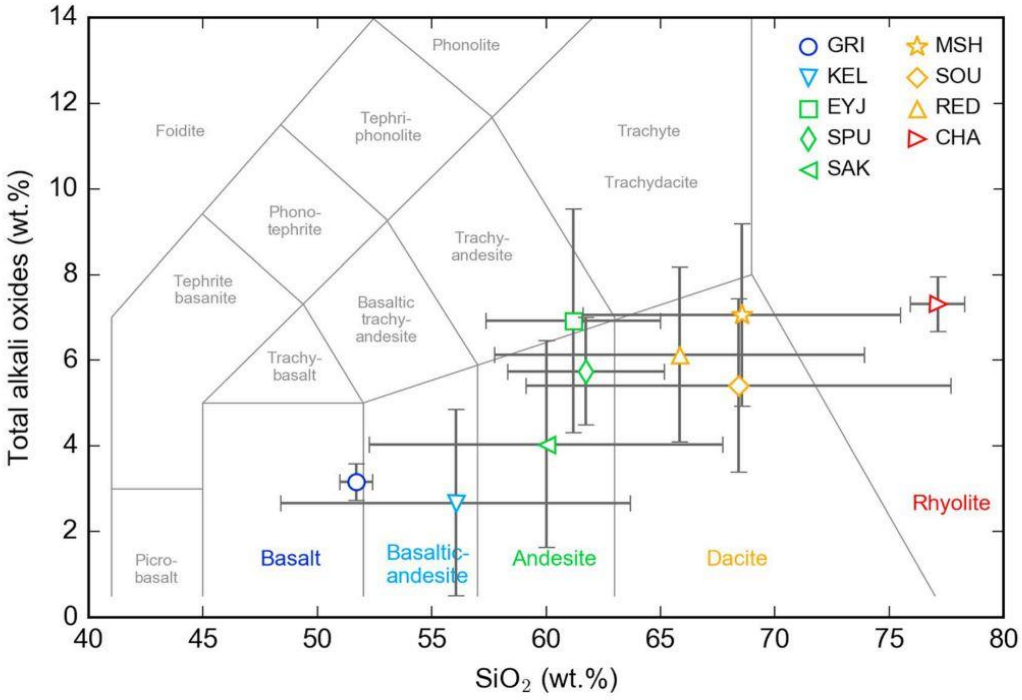

Figure 2.1: Classifications of volcanic ash samples based on their mean SiO_2 and alkali oxide content. The colors indicate the main igneous rock type of the samples; dark blue is basalt, light blue is basalite-andesite, green is andesite, yellow is dacite, and red is rhyolite. The symbols indicate the volcanic eruption that the sample was collected from; GRI is Grimsvotn, Iceland, KEL is Mount Kelud, Indonesia, EYJ is Eyjafjallajokull, Iceland, SPU is Mount Spurr, United States, SAK is Mount Sakurajima, Japan, MSH is Mount St. Helens, United States, SOU is Soufriere, United Kingdom, RED is Mount Redoubt, United States, CHA is Chailten, Chile. Reproduced from Vogel et al. (2017).

In figure 2.1 the percent weights of SiO_2 and alkali oxides will not sum to 100 percent, as much of the constitutive material is not measured or considered significantly important compared to the SiO_2 and alkali oxides. Silicon dioxide gives volcanic ash it's glassy content, while the alkali oxides contribute to the non-linear material behavior (Chen & Zhao, 2015; Giordano et al., 2008). Alkali oxides are what is formed from the reaction between a metallic oxide and water (Krawietz et al., 1998). The alkali oxides also play an important role in determining interfacial characteristics of melted volcanic ash, such as contact angle and surface tension (Hobiger et al., 2011). The data in figure 2.1 exhibits large variations among samples from a single eruption (indicated by error bars) and among samples from different eruption sites around the globe. Throughout this section the suspended constituent material will be referred to as 'crystals', where the composition of the material is unimportant. If the composition, or classification, is important it will be specifically named, e.g. alkali oxides.

Measuring the viscosity of a molten volcanic ash is a non-trivial task. The non-Newtonian material behavior, which arises largely from the crystal content, will cause complications in the mathematics used to derive the measurement method (Krieger, 1953). Taking a direct magmatic sample from an active volcano is not currently possible, so creating a reliable laboratory sample is required. Using wide gap rotational viscometry has been shown to work fairly well for measuring the viscosity of non-Newtonian fluids, becoming the standard method of measuring non-Newtonian viscosities at temperatures and strain rates analogous to magma transport (Krieger, 1953; Macosko, 1994; Sonder et

al., 2006). For the purposes of measuring volcanic ash viscosity with rotational viscometry, the separation gap must be larger than the length scale of the suspended crystals (Hobiger et al., 2011). The cylindrical viscometry method, with an arbitrary gap length, has an exact solution for the viscosity based on the rotation rate of the cylinders and applied torque (Krieger, 1953). The method has been adapted to commercially available tools and supplies accurate results for high temperatures and non-Newtonian fluids (Hobiger et al., 2011; Sonder et al., 2006; Song et al., 2017). Because obtaining samples of actual magmatic substances is near impossible, sample preperation is quite important. Equally as important as composition is how the term 'melt' is defined. Broadly speadking, in the literature the term 'melt' refers to a sample whose material properties are being tested, such as viscosity or thermal conductivity (Eriksson et al., 2003; Giordano et al., 2008; Hobiger et al., 2011; Nishi et al., 2018; Sonder et al., 2006; Song et al., 2017). Unfortunately, 'melt' also refers to how the test sample was prepared and processed, such as sintering and heating rate. While being tested the melt sample can either be in an equilibirum or non-equilibirum state. For silicate melts the equilibirum state is defined as time invariant thermodynamic conditions and material properties (Hobiger et al., 2011; Onorato et al., 1978). Material property equilibrium is when the crystal content has achieved checmial equilibrium, meaning the constituent material (crystal content) is no longer reacting with one another (Lofgren, 1971; Thornber & Huebner, 1985). For studies that don’t mention the state of the crytal content it is assumed that the melt contains both equilibiurm and non-equilibrum crystals. It is likely that there is always some non-equilibirum crystals present in the melt sample, even if the concentration is low

(Lofgren, 1971). The cylindrical viscometry method has been used over a range of 1131 to 1451 °C on samples produced directly from the 2010 eruption of Eyjafjallajökull volcano, Iceland. The results showed a viscosity ranging from ~10^3-10 Pa-s, see figure 2.2 (Song et al., 2017).

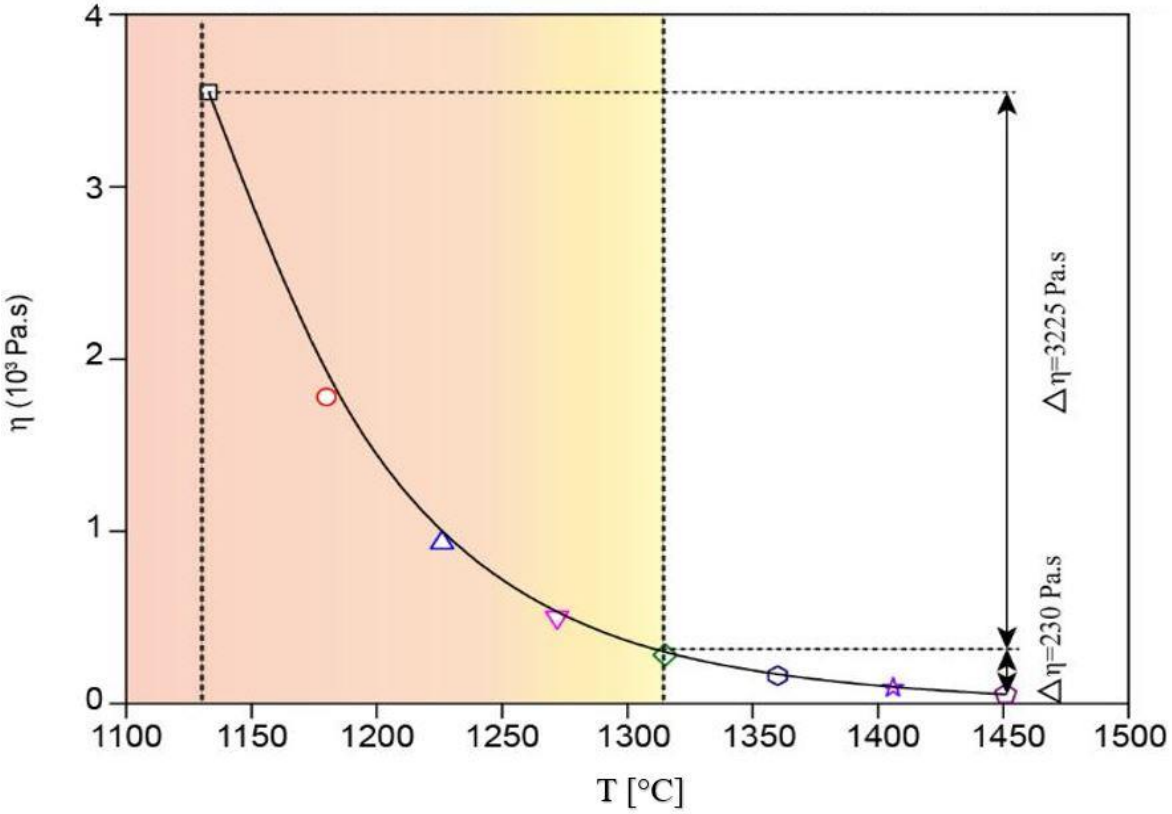

Figure 2.2: Viscosity and temperature plot produced from a cylindrical viscometry test on material gather from the Eyjafjallajökull volcano, Iceland. The red shaded region (left) indicates that the sample has heterogenous microstructures during heating, while the white region (right) indicates homogenous microstructures during heating. Data was collected at temperatures of: 1133 °C (black square), 1180 °C (red circle), 1226 °C (blue delta), 1272 °C (purple triangle), 1315 °C (green diamond), 1360 °C (blue hexagon), 1406 °C (purple star), 1451 °C (dark purple pentagon). Reproduced from Song et al. (2017).

The viscosity of amorphous substances can be well modeled by the Vogel-Fulcher-Tammann (VFT) equation (Lara et al., 2004). Previous models used a strictly Arrhenian temperature dependence to model the viscosity (Bottinga, 1972; Shaw, 1972). An Arrhenian temperature dependence is purely exponential and has been shown to break down at temperatures as low as 130 degrees Celsius. This led to the implementation of models which used three fitting parameters rather than two, known as a non-Arrhenian model (Baker, 1996; Giordano et al., 2004a; Hess & Dingwell, 1996; Vetere et al., 2006). The crystal content, specifically taken as alkali oxides, is crucial to the nonlinear behavior of viscosity (Giordano et al., 2008; Giordano, et al., 2004a; Giordano et al., 2004b). The nonlinear effects of the crystals led to the breakdown of most Arrhenian and non-Arrhenian models. Giordano et al. (2008) developed a semi-empirical model for the viscosity of magmatic liquids using an extensive database to ensure robust data for parameter fitting. The model was developed with data from 1,774 labs which covers most forms of terrestrial volcanic rock. The data considered ranged in temperature from 535 to 1,705 °C, and a viscosity that ranged from 10^{-1} to $10^{13.8}$ Pa-s.

The Giordano et al.'s (2008) model used the form of the VFT equation given by

$$\log_{10} \eta = A + \frac{B}{T(K) - C}. \quad (2.1)$$

Coefficients *A, B,* and *C* are fitting parameters determined from viscosity data given as a function of temperature. It is noted that as the temperature goes to infinity this equation predicts that the viscosity approaches a constant value, regardless of the parameters B and C. This implies that there is a universal high temperature viscosity for all silicate materials, approximately 10^{-5} Pa-s (Angell, 1991, 1996; Eyring et al., 1982; Russell et al.,

2003; Scopigno et al., 2003). Giordano et al.'s (2008) model addressed the coefficient *A* as the value required to achieve the measured high temperature viscosity for a given data set. The coefficients *B* and *C* determined by the Giordano et al.'s (2008) model come from 18 adjustable parameters. The adjustable parameters were determined from linear combinations of coefficients determined by material properties. The result is a system of nonlinear equations that can be solved for the coefficients, which accurately reflected a given data set's material properties. The resulting model is robust for both volatile-rich and anhydrous material compositions, capturing Arrhenian and non-Arrhenian behaviors. Figure 2.3 shows the fitted curve for volatile-rich and anhydrous material compositions with good agreement for both.

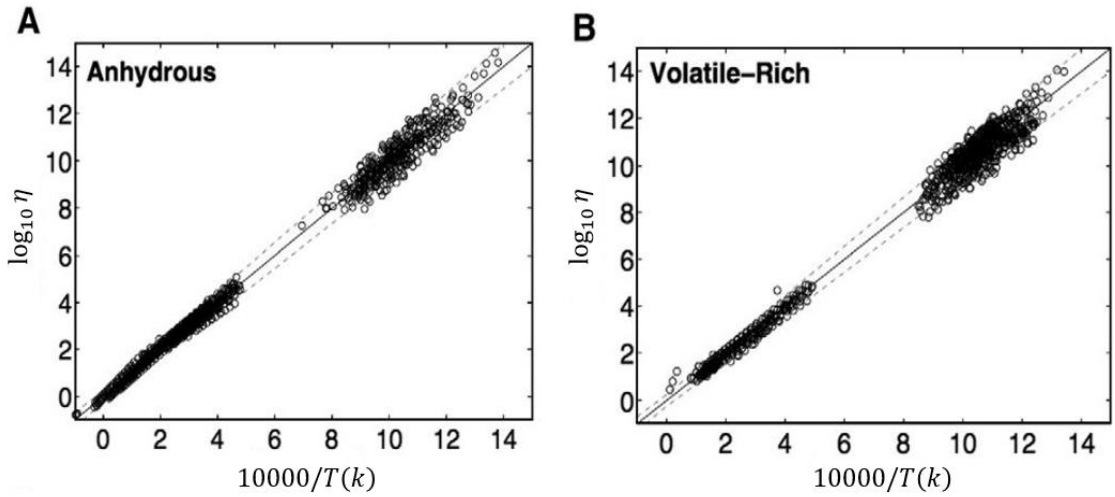

Figure 2.3: Experimental data, shown as the circles, plotted against the Giordano (2008) model, shown as a black line. The black dashed lines are the 5 percent confidence intervals. The y-axis is the base ten logarithm of viscosity. The x-axis is 10,000 divided by the temperature the sample was taken at, *T(k)*. Plot (a) is a data set of anhydrous melt samples, with N=932. Plot (b) is a data set of volatile-rich melt samples, with N=842. Reproduced from Gordiano et al. (2008).

Figure 2.3 can be easily compared to both older and more recent models shown in figure 2.4.

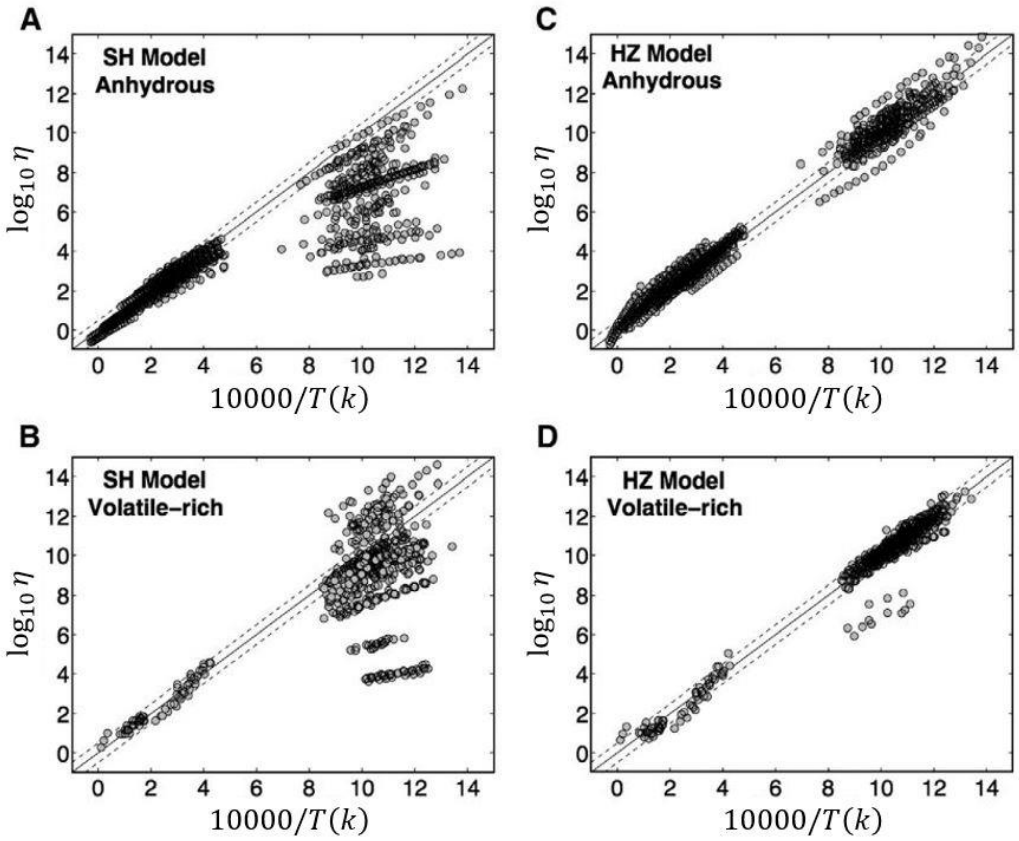

Figure 2.4: Predicted viscosity shown as the solid black line with five percent confidence interval, shown as the dashed black line. Plots (A) and (B) were reproduced with the Arrhenian Shaw (1972) model and the same data used in figure (bb)* by Giordano (2008). Plots (C) and (D) were reproduced with the non-Arrhenian Hui and Zhang (2007) model and the same data used in figure (bb)* by Giordano (2008). The y-axis is the base ten logarithm of viscosity. The x-axis is 10,000 divided by the temperature the sample was taken at, *T(k)*.

*All four plots, (A)-(D), do not include fluorine based experimental samples, the models were not calibrated to this material. Reproduced from Gordiano et al. (2008).

In figure (c) four plots are shown. Two of the plots, (A) and (B), are based on an Arrhenian models (Shaw, 1972). The other two plots, (C) and (D), are based on a non-Arrhenian models (Hui & Zhang, 2007). Both models were calculated using the same

volatile-rich and anhydrous material composition data as figure 2.3. In figure 2.4 Giordano et al.'s (2008) model is clearly shown to be more robust for the presented data.

2.1.2. Volcanic Ash Thermal Properties

The previous section demonstrates that the viscosity of a silicate melt, such as volcanic ash, decreases logarithmically with increased material temperature. If a significant temperature gradient is present in the volcanic ash material, then a significant viscosity gradient will also be present. For this reason, how the material conducts heat becomes very important when considering the impact of ash particles onto GTE surfaces. The thermal properties of volcanic ash melts have not been well studied, so we will also consider properties of silicate-based melts in general in this section as an analogy for volcanic ash, as ash is primarily composed of SiO_2.

Methods for measuring the thermal conductivity of silicate melts were developed in the decades spanning from 1970 to 1990 (Carrigan & McBirney, 1997; Murase & McBirney, 1973; Snyder et al., 1994; Snyder et al., 1997). One of the first methods developed for measuring thermal conductivity of silicate melts used either a hot plate or hot wire to measure heat flux, which was then used to solve the radial heat flow equation for temperature (Murase & McBirney, 1973). This method is very simple to use (Speyer, 1994), but the requirement that the thermocouple must be directly linked to the medium being tested creates contact issues, mainly that attaching the apparatus to a liquid sample is limited (Bagdassarov & Dingwell, 1994). A more sophisticated method, proposed by

Parker et al. (1961) and further refined in a series of papers in the 1990's, is called the laser flash analysis (LFA) method. This method was first applied to silicate melts by Ogawa (1993). The advantage of LFA over a hot plate or hot wire is the minimally intrusive nature of the measurement procedure, where radiation and conduction are less of a concern (Ogawa et al., 1993; Parker et al., 1961). LFA is conducted by placing a cylindrical sample with planer parallel faces on an isothermal surface. An infrared laser pulse is directed at the exposed planar face, where the laser is set up in such a way that the exposed surface heats homogenously. The other planar face will heat up due to conduction, while the surface temperature is recorded as a function of time. The procedure allows for the heating caused by radiation and diffusion to be easily distinguished (see figure 2.5 for a schematic and description of the setup).

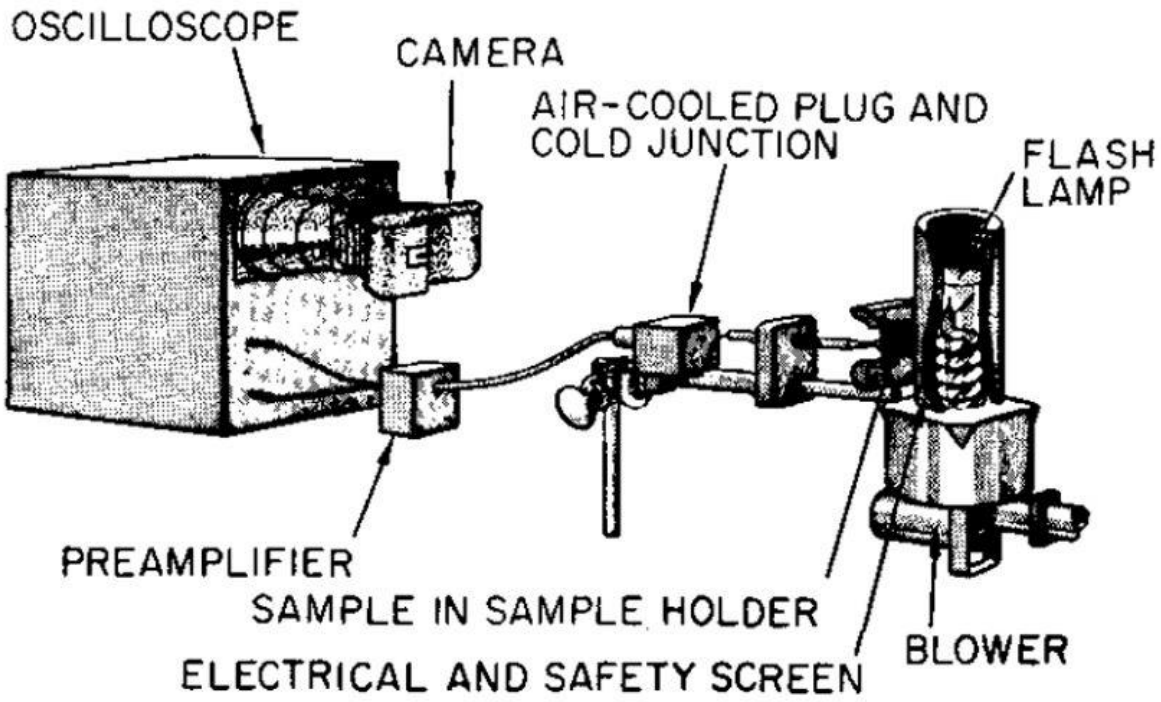

Figure 2.5: Original laser flash analysis (LFA) scheme. The sample holder was connected to a thermo couple on the back side away from the flash lamp. The flash lamp was a commercially available unit capable comprised of a four-turn quartz spiral and Pyrex envelope. Each flash required 400 Joules of energy. The oscilloscope, with the use of a differential transistor preamplifier, output the electrical signal from the thermocouple. The display of the oscilloscope was recorded on a polaroid camera. Reproduced from Parker et al. (1961).

The methods of determining the thermal properties of molten volcanic ash have been developed largely by testing on silicate-based materials. While these materials are certainly useful to validate measurement techniques, results for general silicate-based materials might not be relevant to volcanic ash samples, as volcanic ash is extremely varied in composition of silicate and the crystal materials. The silicate content varies from approximately 30 - 60 percent for volcanic ash samples from different volcanoes,

see figure 2.1. A number of studies done over the last 20 years were examined to typical ranges of the volcanic ash thermal properties, including thermal conductivity, thermal diffusivity, and specific heat. The thermal properties have a strong dependence on the silicate content and crystal content, so the data is presented in terms of order of magnitude. The results of this survey indicate that thermal diffusivity ranges from $O(10^{-7})$ - $O(10^{-6})$ m^2/s. The thermal diffusivity is a relatively challenging quantity to measure and is typically done using the laser flash analysis method (Büttner et al., 1998; Merriman et al., 2013; Vosteen & Rudiger, 2003). The thermal conductivity of volcanic ash ranges from O(1) - O(10) W/m-K (Büttner et al., 1998; Horat & Simmons, 1969; Merriman et al., 2013; Mielke et al., 2016; van Manen & Wallin, 2012). The specific heat ranges from O(0.1) - O(1) J/g-K (Büttner et al., 1998; Mielke et al., 2016; Vosteen & Rudiger, 2003).

2.2. Droplet Impact onto a Flat Surface

This section provides an overview of experimental and numerical results for droplet impact, regime mapping, and approximate models used to describe the droplet motion following impact. Droplet impact on a flat surface is a problem that arises in a wide variety of fluid mechanics applications, including ink-jet printing (Bechtel et al., 1981; Lim et al., 2009; Son & Kim, 2009; van Dam & Le Clerc, 2004; Zable, 1977), thermal spray coating (Alavi et al., 2012; Attinger et al., 2000; McDonald et al., 2006; Pasandideh-Fard et al., 2002), plasma spraying (Bertagnolli et al., 1994; McDonald et al., 2006), raindrop erosion (Abuku et al., 2009; Zhao et al., 2015), pesticide deposition

(Bergeron et al., 2000; Wirth et al., 1991), spray impingement cooling (J. Kim, 2007), lithography (Banine et al., 2011), additive manufacturing (Suli et al., 2017), fire suppression (Manzello & Yang, 2002), icing from freezing rain (Antonini et al., 2011; Fu et al., 2016; Ju et al., 2019; Mishchenko et al., 2010), precipitation effects on erosion and performance degradation of turbine blades (Corrigan & DeMiglio, 1985; Li et al., 2008), and blood splatter forensics (Hulse-Smith et al., 2005; Laan et al., 2014). Previous research on droplet impingement has been extensive, including a wide range of studies examining physical processes such as droplet spreading and oscillation (Clanet et al., 2004; Gao & Li, 2014; Kim & Chun, 2001; Lee et al., 2016; Roisman et al., 2002), rim formation (Eggers et al., 2010; Roisman et al., 2009; Visser et al., 2015), splash formation (Guo et al., 2016; Mani et al., 2010; Riboux & Gordillo, 2014), air entrapment during droplet impact (Kolinski et al., 2012; Liu et al., 2013; Wang & Bourouiba, 2017; Xiong & Cheng, 2018), effect of surface contact angle and surface roughness on droplet spreading (Kim et al., 2013; Šikalo et al., 2005; Tang et al., 2017), anisotropic effects caused by surface motion (Almohammadi & Amirfazli, 2017), and effects of fluid viscoelasticity (Izbassarov & Muradoglu, 2016; Venkatesan & Ganesan, 2019). Four review papers that provide particularly useful overviews of the underlying physics of droplet impact were given by Rein (1993), Yarin (2006), Attané et al. (2007) and Josserand and Thoroddsen (2016).

2.2.1. Overview of Droplet Impact Behavior

Droplet collisions have been visualized experimentally using high-speed cameras by a number of investigators (Attané et al., 2007). However, obtaining detailed measurements of fluid velocity and pressure fields during droplet collisions is both complicated and costly. Various types of numerical methods have been used to simulate droplet collisions, including the Lattice Boltzmann Method (Xiong & Cheng, 2018), the axisymmetric Euler equation (Haller et al., 2002), and the volume-of-fluid (VOF) and VOF-like solvers (Pasandideh-Fard et al., 2002; Šikalo et al., 2005; Yokoi et al., 2009). A challenge in numerical modeling of droplet impact concerns solving for the motion of the contact line, which is the line on the solid where the two fluid phases and solid all meet (see figure 2.6).

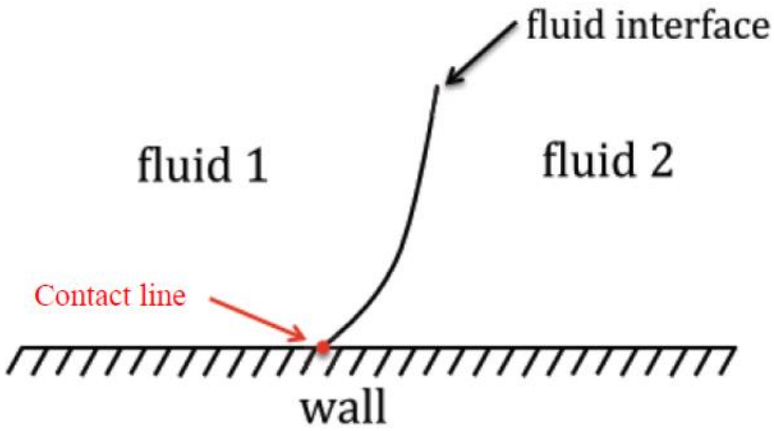

Figure 2.6: A schematic of the moving contact for two fluid phases. The red dot indicates the cross section of an arbitrary curve going into and out of the page, for a three-dimensional case. If two dimensions are considered then the red dot is only a point, referred to as the triple point. Reproduced from Holmgren (2017).

It has long been known that the fluid near the contact point undergoes a rolling motion (Dussan, 1979) and that at the molecular scale there is slip along the wall near the contact line, whose value is proportional to the shear stress (Shikhmurzaev, 1997). This molecular slip, also referred to as Navier slip, is necessary to overcome the stress singularity in the continuum theory associated with motion of the contact line (Dussan & Dussan V., 1976). Computational methods regulate this singularity in a number of different ways, either by explicitly introducing slip near the contact line or via discretization of the Navier-Stokes equations. A full discussion of contact line regularization by the VOF method is given by (Afkhami et al., 2009; Legendre & Maglio, 2015). A second complication associated with the contact line involves time-variation of the contact angle associated with contact line motion, the so-called dynamic contact angle (Blake et al., 1999; Šikalo et al., 2005). The dynamic contact angle depends on the surface roughness, the contact line speed, and the chemical heterogeneity of the impact surfaces (Choi et al., 2009; David & Neumann, 2011; Extrand & Kumagai, 1996). For a more detailed of dynamic contact angle properties, refer to Eral et al. (2013).

Numerical simulations excel at visualizing fields that cannot be easily determined experimentally (Alavi et al., 2012; Bussmann et al., 2000; Eggers et al., 2010; Hirt & Nichols, 1979; Pasandideh-Fard et al., 2002; Philippi et al., 2016; Šikalo et al., 2005; Sussman & Puckett, 2000; Wildeman et al., 2016; Xiong & Cheng, 2018). The first computationally efficient and widely used method for interface tracking and multiphase flow modeling was the volume-of-fluid formulation (Hirt & Nichols, 1979). The original VOF formulation lacked both surface tension modeling and was quite diffuse in the

interface. The surface tension modeling was addressed by Brackbill et al. (1992) and was adapted to the VOF formulation (Bussmann et al., 2000). Front tracking and level-set (LS) algorithms produce highly resolved interfaces and geometric reconstructions (Sethian, 1999). However, it is well known that level-set algorithms are not mass conserving. Coupling the VOF and LS algorithms produces a solver that is both mass conserving and highly resolved (Sussman & Puckett, 2000).

Any sort of analytical or numerical droplet spreading model either directly or indirectly confronts the moving contact line (MCL). The MCL deals with motion of fluid interfaces as they move along solid surfaces, see figure 2.7. The velocity and spreading of the MCL is dictated by both the material and surface properties (Dussan, 1979), including the static and dynamic contact angle. The static contact angle is a material property while the dynamic contact angle changes throughout the spreading process (De Gennes, 1985; Dussan, 1979; Hoffman, 1975). The Hoffman–Voinov–Tanner law couples the cubic dynamic and cubic static contact angles proportionally to the spreading velocity (Hoffman, 1975). The Hoffman–Voinov–Tanner law is only a proportionality statement so empirical modeling is often used to couple the dynamic and static contact angles with the spreading velocity (Jiang et al., 1979).

For droplet impact normal to a flat stationary surface, three broad flow categories can be used to describe the result of the impact - bouncing, spreading, and splashing (figure 2.7).

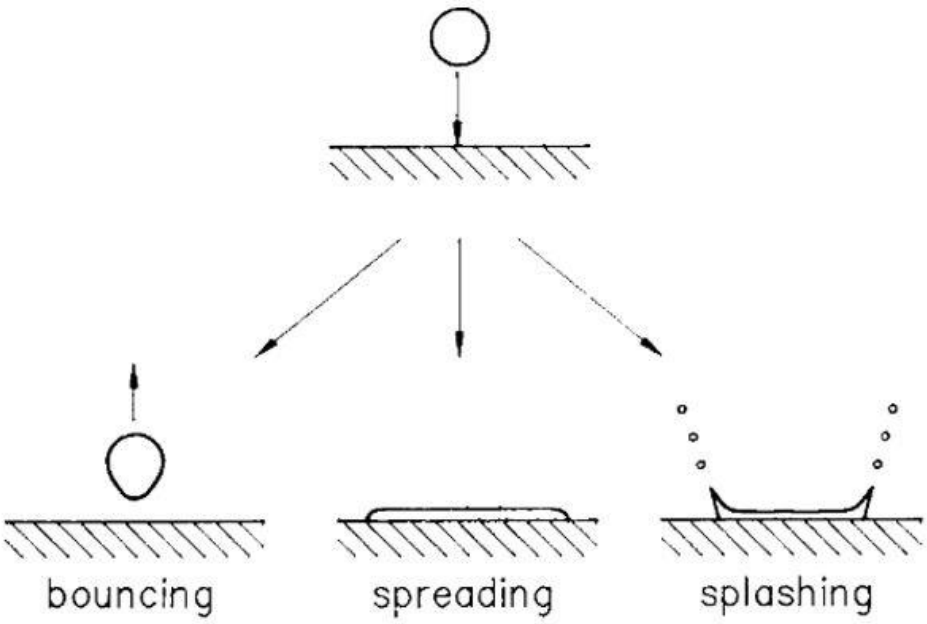

Figure 2.7: The three possible collision mechanics of normal droplet impingement; bouncing, spreading, and splashing. Reproduced from Rein (1993).

For bouncing to occur a droplet collides with a solid surface without any wetting. This typically occurs on super hydrophobic surfaces where the contact angle is close to 180º. Kinetic energy is transferred to the impact surface without wetting which allows for bouncing (Richard & Quéré, 2000). If the surface allows wetting, then spreading will occur. Two possible limiting cases exist for spreading. The first is that the kinetic energy is small and near zero. The second is that the kinetic energy and impact velocity are of moderate magnitude. If the kinetic energy is near zero then the molecular forces, such as surface tension, govern spreading. If the kinetic energy and impact velocity are of moderate magnitude, the balance between dissipation and surface energy governs spreading. Splashing is characterized by the breakup of one droplet into two or more

upon collision with the surface. The limit when spreading transitions to splashing is governed by the impact conditions and fluid material properties. A delicate balance of kinetic energy and surface tension, classified by the Weber number, acts as a critical indicator. However, the viscosity and surface properties (e.g., contact angle) are not included in the Weber number, so another criterion is required. The development and examination of this criterion is the focus of much literature (Baker et al., 1988; Burzynski & Bansmer, 2018, 2019; Schmidt & Knauss, 1976; Stow et al., 1981; Walzel, 1980).

2.2.2. Regime Mapping

The dynamics of droplet impact are determined by the droplet diameter *D*, the impact velocity *V*, and direction of the droplet motion relative to the collision surface, as well as the properties of the materials involved. Important material properties include the surface tension, density, viscosity and contact angle, as well as thermal properties for problems involving heat transfer. The substrate the droplet collides with has a significant effect on the collision dynamics, properties such as surface roughness and wettability.

Four dimensionless parameters are used to classify the droplet collision, as given in (2.2a-d). Important dimensional variables include the liquid density, surface tension, and viscosity, as well as length and velocity scales. The Weber number, *We*, is the ratio between the inertial and surface tension forces. The Reynolds number, *Re*, is the ratio of inertial and viscous forces. The Ohnesorge number, *Oh*, is the ratio of the Weber and Reynold number. The final parameter, the Bond number, *Bo*, describes the ratio of

gravitational and surface tension forces. In these equations, ρ and μ are the liquid density and viscosity, σ is the liquid-gas surface tension, and g is the acceleration of gravity. Typically, the Bond number is found to be much smaller than unity, implying that gravitation effects are negligible. The three remaining dimensionless parameters - *We*, *Re* and *Oh* - are coupled so only two are needed to describe a collision. The dimensionless parameters are defined mathematically by

$$We = \frac{\rho D V^2}{\sigma} \qquad Re = \frac{\rho D V}{\mu} \qquad Oh = \frac{\mu}{\sqrt{\rho D \sigma}} = \frac{\sqrt{We}}{Re} \qquad Bo = \frac{\rho g D^2}{\sigma} \quad . \tag{2.2}$$

Because droplet impingement can be described using two parameters, such as the Weber and Ohnesorge or Weber and Reynolds numbers, regime mapping can conveniently be performed in a two-dimensional space. A regime map proposed by Schiffano and Sonin (1997a) includes four regions labeled I-IV (figure 2.8).

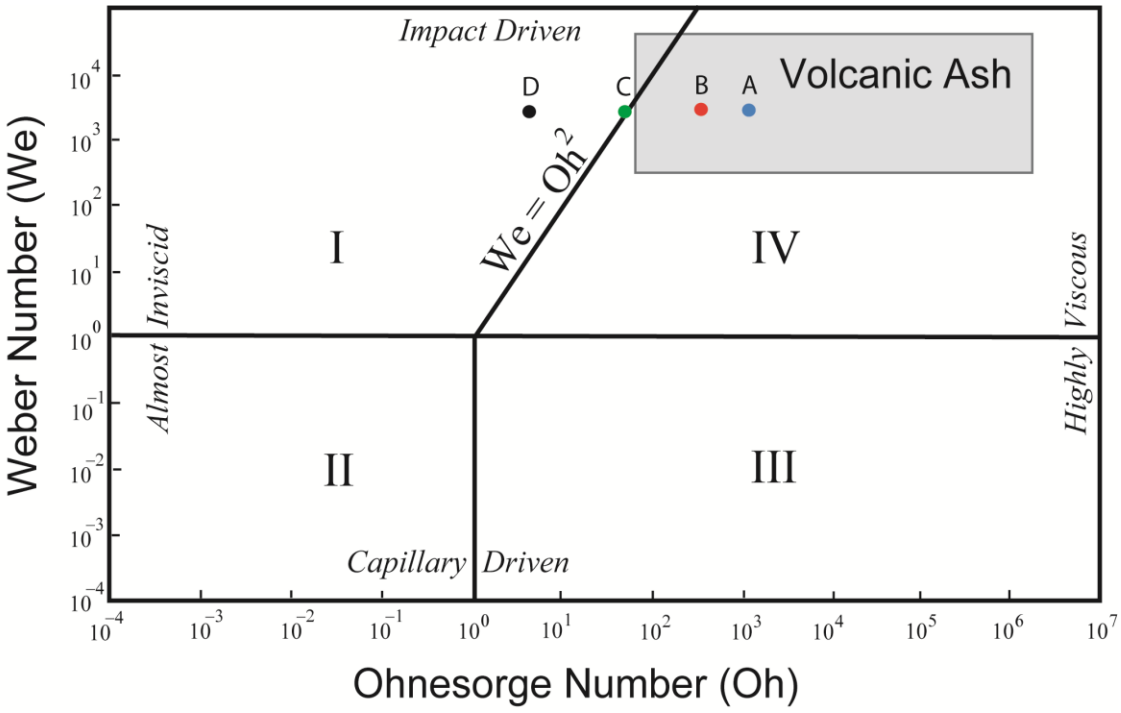

Figure 2.8: Schiaffino-Sonin map showing four regimes of droplet impact in the plane of Weber number versus Ohnesorge number. The range of parameter values typical of molten volcanic ash particle impingement in the hot section of gas turbine engines is indicated by a shaded rectangle. The four points indicate computational conditions examined, with Re = 0.05 (A, blue), 0.19 (B, red), 1 (C, green), 10 (D, black).

Each region is dominated by different mechanics. Region I describes as collision that is impact-driven and almost inviscid. The droplet fluid spreads out rapidly into a thin sheet, and then undergoes a series of oscillations in which the flow alternates from spreading radially outward to rebounding back inward. These oscillations are eventually damped by viscous diffusion. In Region II, the flow is again nearly inviscid, but the spreading is driven more by capillary force rather than by the impact pressure difference. The droplet again experiences oscillations that are damped over time by viscous effects. Region III is characterized by highly viscous droplets whose outward spreading is driven by capillary

force and resisted by viscous shear. The droplet spreads slowing outward on the surface, with no oscillations, and the impact velocity has negligible effect. Region IV is characterized by droplets that are highly viscous, so that the droplet spreading is driven by the impact pressure and resisted by viscous shear. There are no oscillations in this region, and droplet is observed to maintain approximately a spherical cap form. The problem of volcanic ash collision in gas turbine engines is characterized by the shaded region shown in figure 2.8, which lies mostly in Region IV.

2.2.3. Spreading and Analytical Modeling

Because of the complexities of fully resolving and understanding three-dimensional droplet impingement, an approximate model is desirable. An approximate model is also advantageous because most industry applications are only concerned with the geometric properties of the droplet collision, such as the spreading radius and final deposition shape. A typical approximation made in droplet impact studies is restriction to an axisymmetric flow field, which can be described by two spatial dimensions and time. A variety of other approximations are typically made in developing simplified models for droplet impacts, including restrictions on droplet geometry, velocity profile, and dissipation rate. Development of approximate models for droplet impacts is discussed in detail by Attané et al. (2007).

Experimental and analytical modeling of droplet collision has been of scientific interest for over a century (Worthington, 1876). While Worthington (1876) did not have

the means to image the droplet collision or the ability to model the process, he did spark the race to understand the spreading phenomena. The next significant study on the subject had the technology to image the spreading process, and attempted to model several characteristics of the droplet (Engel, 1955). The quantities calculated included the maximum impact pressure and the spreading radius. The calculated spreading radius appears to be in good agreement, but this assessment is based only on inspection of table 1 from the study (Engel, 1955), no comparative figure was provided. Despite developing an expression to calculate the maximum impact pressure, no experimental or calculated data was provided for comparison (Engel, 1955).

Engel (1955) did not apply strict geometric constraints to the colliding droplet as it evolves in time. Instead, an area internal to the droplet where the fluid velocity was considered significant was considered. Kendall and Rohsenow (1979) were the first researchers to use an energy balance that included explicit geometric constraints, calculation of kinetic energy, and potential energy. The report introduced the cylindrical disk and spherical cap geometries, see figure 2.9 (a) and (b).

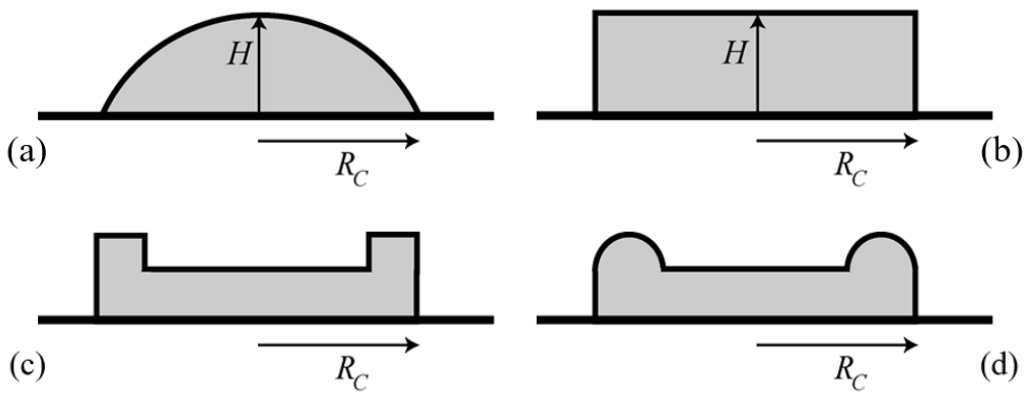

Figure 2.9: Approximate droplet shapes used in various droplet impingement theories: (a) truncated sphere, (b) cylinder, (c) rimmed cylinder, (d) cylinder with spherical rims.

The model did not account for viscous dissipation (Kendall & Rohsenow, 1978), which was introduced by (Bechtel et al., 1981). The Bechtel model balanced kinetic energy, surface tension, and dissipation with geometric constraints, resulted in an ODE for the droplet height. The kinetic energy was obtained by assuming that the droplet flow was an irrotational straining flow. The potential energy was modeled as the interfacial area between the gas and liquid minus the contact surface area multiplied by one minus the contact angle. The viscous dissipation was included by approximating the region where dissipation occurs as a thin boundary layer. The effect of the thin boundary layer was modeled as the shear stress over some radial displacement. The shear stress was assumed to be the product of the radial velocity, viscosity and a constant. The constant had dimensions of inverse length. The radial displacement was written as a function of the center of mass and radius. The ODE was written in a dimensionless form, embedding parameters describing the surface tension and viscous dissipation into the models. Solving the ODE was done numerically using a Runge-Kutta integrator while

systematically varying the governing parameters. The result was a comprehensive study that analyzed the stability of the energy balance as it was numerically integrated for various parametric values. The numerical results were compared against available experimental data and were overall not in good agreement. Nevertheless, this study pioneered the concept of mathematically modeling the viscous dissipation in a droplet. Kendall and Rohsenow (1979) and Bechtel et al. (1981) established the standard energy balance recipe used in analytical modeling.

The dissipation rate of a droplet collision isn't only governed by the viscosity and radial velocity with a constant, as proposed by Bechtel et al. (1981). The dissipation function can be represented as tensor product of velocity gradients, given by (Chandra & Avedisian, 1991)

$$\phi = \mu\left(\frac{\partial u_i}{\partial x_j} + \frac{\partial u_j}{\partial x_i}\right)\frac{\partial u_i}{\partial x_j}. \tag{2.3}$$

The dissipation function was approximated by the initial state of the collision, eliminating the need for a correction coefficient. The energy balance formulation used by Chandra et al. (1991) was significantly different than Bechtel et al. (1981), in that the initial kinetic and potential energy were balanced against the final potential energy and dissipation rate. The initial kinetic and potential energy states were calculated from the initial geometry and impact conditions, as well as the material properties. The final potential energy was a function of the final spreading diameter. The balance resulted in an analytical expression for the maximum spreading factor as a function of the initial parameters and contact angle. The initial parameters were given as the Weber and Reynolds. The liquid-solid

contact angle was given as a function of the collision substrate temperature, which was referred to as the 'wall temperature'. The analytical expression was used to obtain the maximal spread radius data as a function of the wall temperature. Comparing the analytical data to available experimental data revealed a significant discrepancy. This was attributed to either not accounting for viscous dissipation correctly or droplet evaporation occurring during spreading. The latter is likely as evaporation was not included in the analytical model and the analytical results were consistently higher.

The energy balance used by Chandra and Avedisian (1991) was further developed by Pasandideh-Fard et al. (1995). The dissipation function developed by Chandra and Avedisian (1991) was taken and modified to include boundary layer effects (Pasandideh-Fard et al., 1996). The boundary layer effects were captured by using the classical self-similar solution (White, 1991), for which the boundary layer thickness scales with the inverse square root of the Reynolds number. The boundary layer thickness in conjunction with the cylindrical disk geometry yields a modified dissipation formulation, yielding a modified solution for the maximal spread radius (Pasandideh-Fard et al., 1996). An experiment was used to obtain transient spread radius and contact angle data. The volume-of-fluid approach originally developed by Hirt and Nichols (1979) was modified to include dynamic contact angle. The computations were used to compare to the experimental images and spreading data. Qualitatively and quantitatively, the experimental spreading data agreed well with the computations. The analytical maximal spreading radius was compared against various experimental results, which also agreed well for a range of parameters.

The regime map discussed in section 2.2.2 was developed by Schiaffino and Sonin (1997a) to explore the wide variety droplet deposition parameters. Both molten and non-molten materials were tested. The non-molten materials were tested under isothermal conditions and the molten materials were performed under non-isothermal conditions. The results indicated that the low Weber number limit is driven by capillary force. In the highly viscous limit, the spreading is resisted by the contact line velocity and dynamic contact angle. In an inertially dominated limit the mechanics become much more complex, including rebound, receding, and oscillations, all with their own respective time scales. In the case of non-isothermal molten deposition, the spreading mechanism is coupled to solidification mechanism. In the coupled spreading-solidification problem two singularities are present, the MCL and the heat flux problem (Schiaffino & Sonin, 1997b). Schiaffino and Sonin, (1997b) showed that continuum theory breaks down when considering a molten liquid cooling as it spreads along a similar solid surface. The contact angle at which the material solidifies cannot be determined because at the contact point the heat flux is singular (Schiaffino & Sonin, 1997b).

Continued modification of the dissipation mechanism proposed by Bechtel et al. (1981) was done by Kim and Chun (2001). The improved dissipation mechanism proposed by Pasandideh-Fard et al. (1995) only predicted the final spread radius, rather than the time-variation of the droplet radius. Instead, Kim and Chun modified the dissipation model employed by Bechtel et al. (1981) to use a semi-empirical expression, where the correction coefficient was scaled by the Ohnesorge number (Kim & Chun, 2001). The change to the correction coefficient was the only change made to Bechtel et

al.'s (1981) model. The same kinetic energy and potential energy models as Bechtel et al. (1981) were used. The resulting ODE was functionally the same and solved with a Runge-Kutta type integrator. The correction coefficient was determined empirically by solving the ODE and tuning the coefficient, so the maximum spread factor was equal to the experimental spread factor. All of the experiments that were conducted were classified as a Region I collisions, the collisions are shown in figure 2.8. In figure 2.8 the Reynolds numbers of the collisions shown in (a) and (b) are 730 and 1410, respectively. The results shown were consistent with the expected mechanics for an inertia-dominated collision, see figure 2.10 (a) and (b).

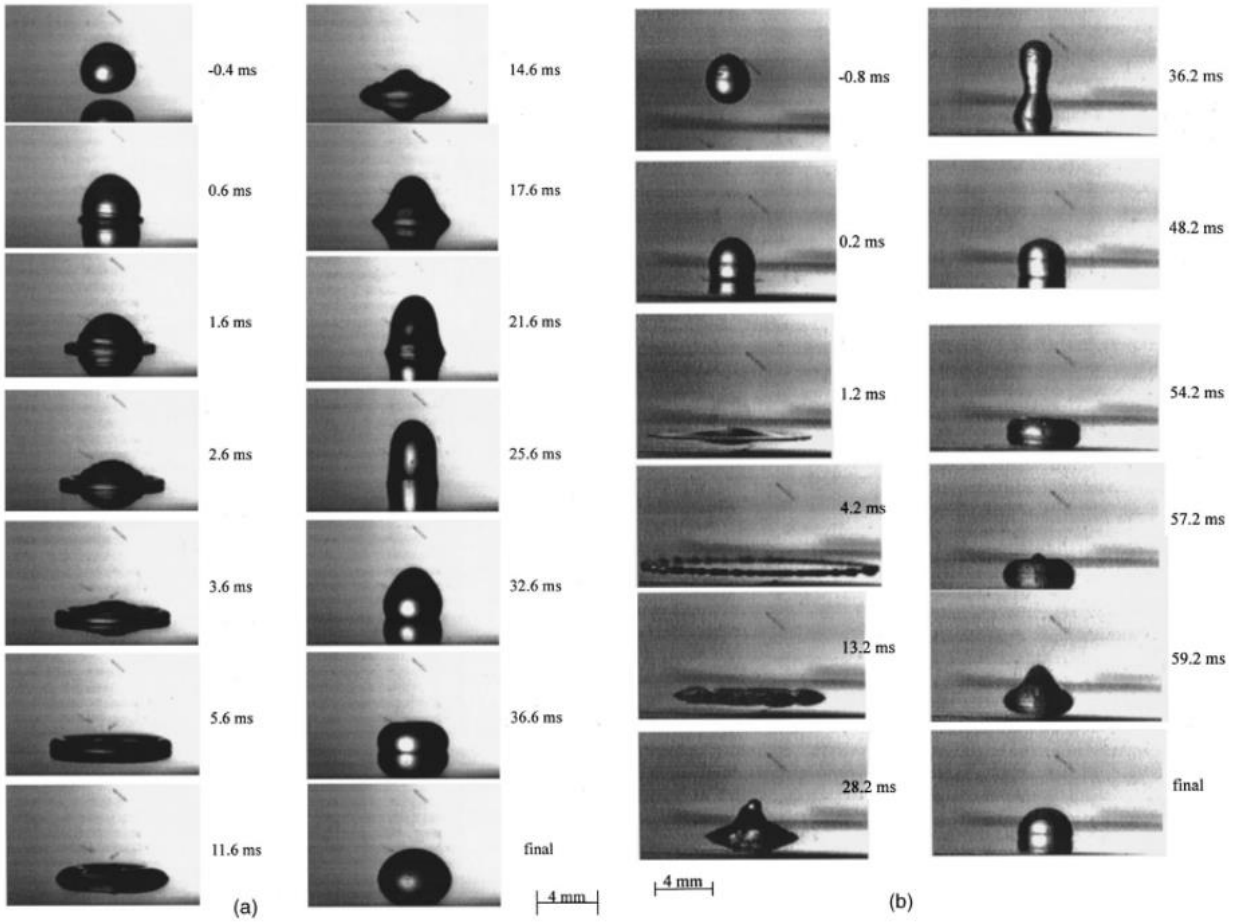

Figure 2.10: Droplet collision of water onto a polycarbonate surface. (a) Droplet diameter of 3.6 mm, impact velocity of 0.77 m/s. Corresponding We and Oh numbers are 30 and 0.0017, respectively. (b) Droplet diameter of 3.5 mm, impact velocity of 3.47 m/s. Corresponding We and Oh numbers are 582 and 0.0017, respectively. Reproduced from Kim & Chun (2001).

In both of these figures, the droplet spreads out rapidly into a lamella with a rim and then recedes inward and outward until reaching its final resting state. In figure 2.10 (b) fingers are formed and the rim spreads further and more thinly than (a). The purpose of this study was to develop a semi-empirical one-dimensional model describing the spreading process. Results shown in figure 16 compare the model to the experimental results shown in figure 2.10a. Figure 2.11 shows the Reynolds number 730 experimental and numerical data.

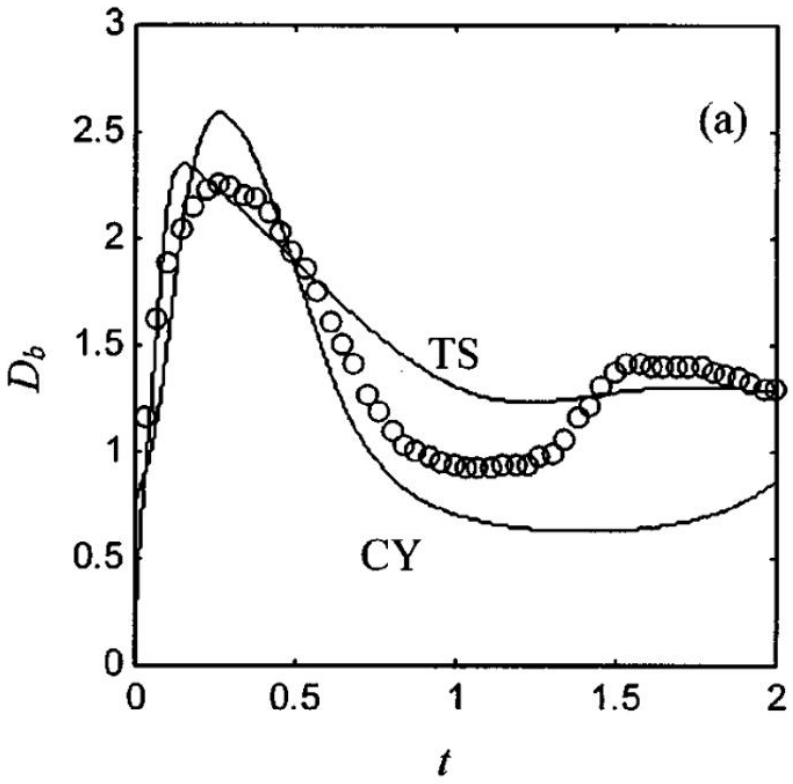

Figure 2.11: Experimental results for We and Oh numbers 30 and 0.0017, respectively, shown as circles. The solid lines indicate the semi-empirical model assuming either the truncated-sphere (TS) or cylindrical (CY) geometry. Both cases assume an irrotational straining flow as the velocity profile. Reproduced form Kim & Chun (2001).

The truncated sphere model agrees reasonably well with the spreading process but does not capture the amplitude of the oscillations effectively, see figure 2.11. The cylindrical disk model captures initial spreading process well but overall does not perform as well as the spherical cap model.

The spreading of moderate and high Reynolds number droplet collisions often results in lamella bound by a rim being formed (Chandra & Avedisian, 1991; Kim & Chun, 2001; Pasandideh-Fard et al., 1996; Rioboo et al., 2002). Prior to the 2000's all

attempts made to model droplet spreading assumed a simple geometry, either a spherical cap or cylindrical disk. As it is seen in the referenced studies the droplet spreading geometry determined experimentally isn't a simple geometry. Roisman et al. (2002) considered a disk combined with a half sphere. The novel geometry was accompanied with a new velocity profile which was taken as the viscous creeping flow between two approaching disks. The dissipation was taken to be similar to Chandra and Avedisian (1991) but was not simplified and instead was written in an axisymmetric form as

$$\phi = 2\mu\left[\left(\frac{\partial u}{\partial r}\right)^2 + \left(\frac{u}{r}\right)^2 + \left(\frac{\partial w}{\partial z}\right)^2 + \frac{1}{2}\left(\frac{\partial u}{\partial z} + \frac{\partial w}{\partial r}\right)^2\right]. \tag{2.4}$$

The same potential energy model as Bechtel et al. (1981) was used. In the case were the dissipation was not considered, the results were compared against experimental data for $Re \gg We$. The results for these cases agreed well, but when dissipation was considered and compared against equivalent experimental data the agreement broke down rapidly. The problem of developing a more realistic geometry describing the spreading process is periodically revisited. Attané et al. (2007) attempted to better model the formation of the lamella by developing a rimmed cylinder (figure 2.9c). The end result isn't exactly a lamella, but there is a rim around the outer diameter of the spreading droplet. Similar to Kim and Chun (2001) a semi-empirical model was developed. The same kinetic and potential energy models as Bechtel et al. (1981) were used. The results were compared against Kim and Chun (2001) and Bechtel et al. (1981). The Attané et al. (2007) model more accurately captured the data while maintaining the spreading oscillations. The rimmed cylinder model was further improved by changing the rimmed cylinder to a rimmed sphere (Gao & Li, 2014), shown in figure 2.9d. Gao and Li (2014) developed

two different analytical expressions; one for maximum spread factor and one for transient spreading. The maximum spread factor model was developed similarly to Pasandideh-Fard et al. (1995), where the potential energy differed to include a non-uniform pressure field. The dissipation given by Pasandideh-Fard et al. (1995) was modified to include both spreading and receding radii and associated contact angles. The transient spread factor model was developed similarly to Bechtel et al. (1981), with modifications to the three energy terms to better describe advancing and receding radii. Results for the maximal spread factor agreed well with the experiment data. The results for the transient modeled agreed well with the presented experimental data, but only data from the author was provided. The provided data did not capture a wide range of parameters or physics, such as spreading oscillations.

The collision surface plays a role in the spreading dynamics by affecting the dynamic contact angle. Spreading on a superhydrophobic surface can result in rebound and bouncing (Clanet et al., 2004; Rioboo et al., 2002). Plotting the spread factor versus some dimensionless parameter, like the Reynolds or Weber number, reveals the nature of spreading under limiting conditions. Rioboo et al. (2002) completed a series of droplet impingement experiments across a wide range of parameters. The Reynold's number ranged from 9 to as high as 8800, with Weber numbers ranging from 30 to 600. The purpose was to propose a new equation that could predict the spread factor. What was found is that as the time after collision increases, the number of factors that determine spreading increases. This means that for longer times it will become harder, if not impossible, to develop an expression for the spread factor that is globally accurate

(Rioboo et al., 2002). Clanet et al. (2004) conducted a droplet impingement study with fluids having low and high viscosities onto a super hydrophobic and partially wetting surfaces. The intent was to study droplet spreading that is resisted by capillary or viscous forces. In figure 2.8 the regions that resist motion through capillary action are I and II while Regions III and IV resist motion through high viscous forces. Clanet et al. (2004) defined the impact parameter $P=We/Re^{-4/5}$ as a universal data rescaling. The impact parameter is capable of capturing both capillary and viscous effects when plotted with the maximal spreading renormalized by $Re^{1/5}$ (figure 2.12).

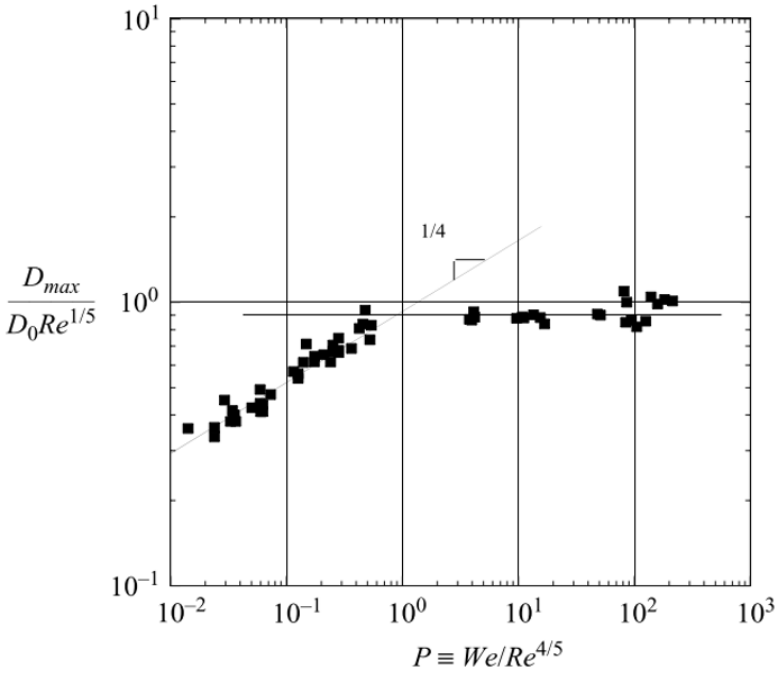

Figure 2.12: Maximum dimensionless spreading of an impinging drop, normalized by a factor of $Re^{1/5}$, as a function of the impact number P. Reproduced from Clanet et al. (2004).

For *P* less than unity, the droplet spreading is resisted by capillary action. For *P* greater than unity, the droplet is resisted by viscosity. A transitional point is location at *P* equal to unity. Both the capillary and viscous regions contain their own scaling laws (Clanet et al., 2004). For the capillary regime the maximal spreading scales as $D_{max} \sim D_0 We^{1/4}$ and the viscous regime scales as $D_{max} \sim D_0 Re^{1/5}$.

It was claimed by Laan et al. (2014) that the scaling results for the capillary regime from Clanet et al. (2004) were not generally valid for different materials, but that the scaling expression $D_{max} \sim D_o We^{1/4}$ was only valid for water (Laan et al., 2014). The contact angles measured for the liquid-surface combinations ranged from 20 to 90

degrees (Laan et al., 2014), so these were not classified as superhydrophobic. This indicated that the material properties play an important role in capillary-driven spreading. Figure 2.13 shows four different materials colliding with stainless-steel with curves representing two different scaling arguments.

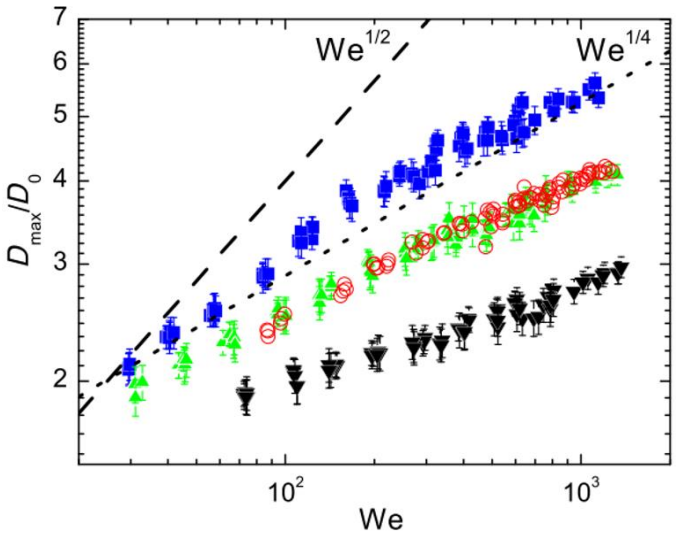

Figure 2.13: The spread factor (D_{max}/D_0) plotted against the Weber number. The blue squares are water, up triangles are water-glycerol at 6 mPa-s, down triangles are water-glycerol at 51 mPa-s, and circles are blood. All collisions occurred onto stainless steel, with a contact angle varying from 80-90 degrees. The short-dashed line is $D_{max} \sim D_o We^{1/4}$ and the long-dashed line is $D_{max} \sim D_o We^{1/2}$ proposed by Clanet et al. (2004) and Eggers et al. (2010). Reproduced by Laan et al. (2014).

Laan et al. (2014) used figure 2.13 to claim that two parameters based on the initial conditions cannot be used to describe the whole spreading process. This suggests that there is likely a smooth transition from the capillary regime to the viscous regime, which can't be modeled by a single parameter. To address this a function that interpolates

between two scaling arguments given as the Weber and Reynolds number is used, an expression was proposed by Eggers et al. (2010) of the form

$$D_{max}/D_0 \propto Re^{1/5} f_{EC}(WeRe^{-2/5}). \quad (2.5)$$

This equation was developed using asymptotic theories and scaling arguments, validated by computations. The scaling arguments were defined as $We^{1/2}$ and $Re^{1/5}$ with a rescaling variable of $WeRe^{-2/5}$. The resulting equation was solved using a Padé approximant which requires the use of a fitting parameter. The rescaling for the given experimental data, as well as data taken from other studies, worked very well once the tuning parameter was fitted using a least squares method. The scaling arguments defined by Clanet et al. (2004) as $We^{1/4}$ and $Re^{1/5}$ with a rescaling variable of $WeRe^{-4/5}$. The results did not collapse to a single curve, failing to produce a universal model.

Producing experimental results over a wide range of Weber and Reynolds numbers is difficult. Developing highly viscous fluids may require melting amorphous solids or using non-Newtonian fluids (Gordillo et al., 2018; Song et al., 2017). Producing and controlling droplets with very small length scales and imaging the spreading is challenging. This challenge was partially overcome with clear limitations in the reliability of the spreading images (Visser et al., 2012) (figure 2.14).

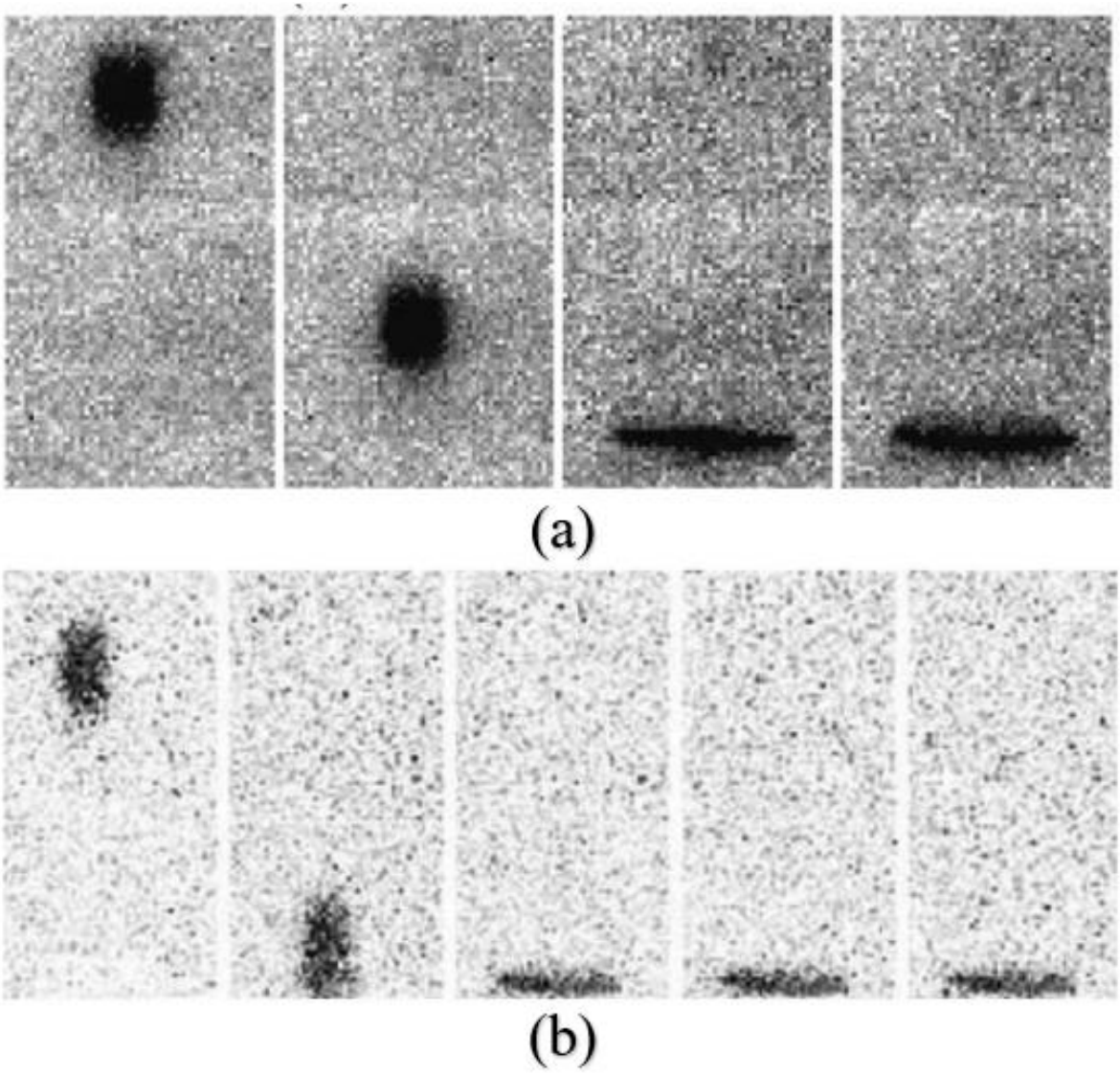

Figure 2.14: Two high speed micro droplet collision image sets. Both image sets were sampled at one micro-second intervals. (a) Impact velocity of 73 m/s, droplet diameter of 23 µm. Corresponding We and Oh numbers are $1.8*10^3$ and 0.0223, respectively. (b) Impact velocity of 100 m/s, droplet diameter of 20 µm. Corresponding We and Oh numbers are $1.8*10^3$ and 0.0238, respectively. Reproduced from Visser et al. (2012).

Visser et al. (2012) sought to develop an experimental method to accurately produce micron sized droplets but did not address the issue of viscosity. The result was an

apparatus that produced droplets with a diameter of 12 µm and with an impact velocity as high as 100 m/s. The validity of the method was tested by taking the spread factor as a function of the Weber number and plotting analytical models provided by Chandra and Avedisian (1991) and Pasandideh-Fard et al. (1995). Experimental data from other another study with similar parameters was taken for comparison. A new experimental method was successfully developed. Figure 2.15 took data from various authors and plotted a *Re*-*We* map with the impact parameter equal to one as a solid line.

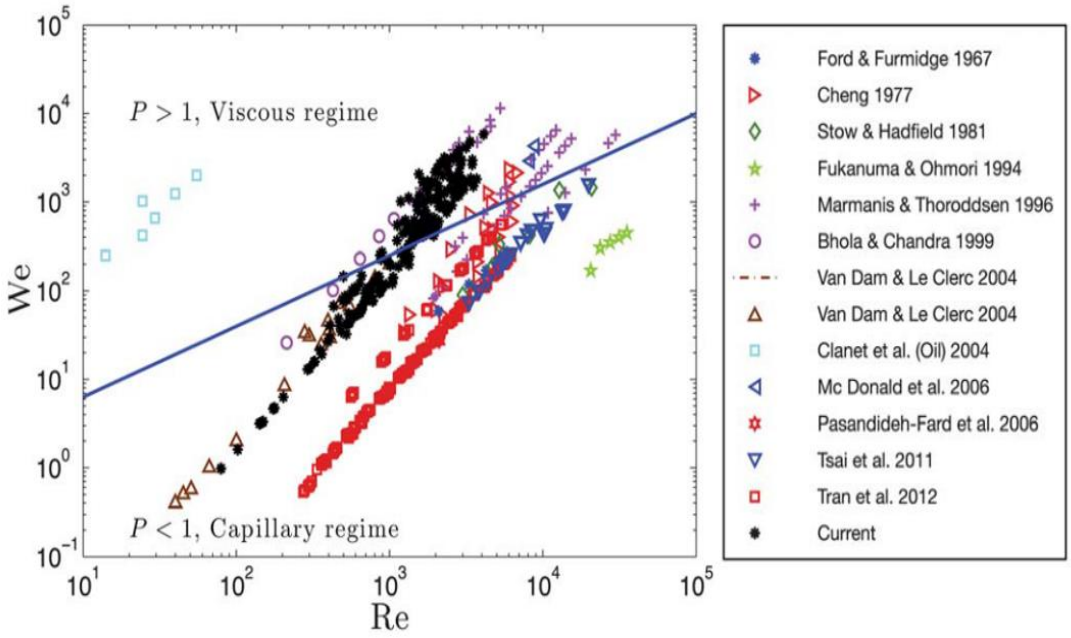

Figure 2.15: Weber and Reynolds numbers for various droplet impact experiments, with sources given in the box to the right. The solid blue line indicated *P* equals one, where capillary regime is $P < 1$ and the viscous regime is $P > 1$. Reproduced from Visser et al. (2012).

The figure effectively shows how few studies have considered low Reynolds number droplet collisions in the viscous regime.

Non-Newtonian fluids can be used to produce extremely viscous fluids (Gordillo et al., 2018). The result is a fluid with a kinematic viscosity as high as 0.3 m^2/s and a Reynolds number of 0.11. By using a piezoelectric force sensor highly accurate data was rapidly taken (Gordillo et al., 2018; Lagubeau et al., 2012). Capturing pressure is advantageous because it can be computed numerically (Philippi et al., 2016). Using experimental and numerical data, analytical expressions for pressure at the collision surface have been developed (Gordillo et al., 2018; Lagubeau et al., 2012; Philippi et al., 2016). Three analytical expressions are plotted against data taken by Gordillo et al. (2018) in figure 2.16.

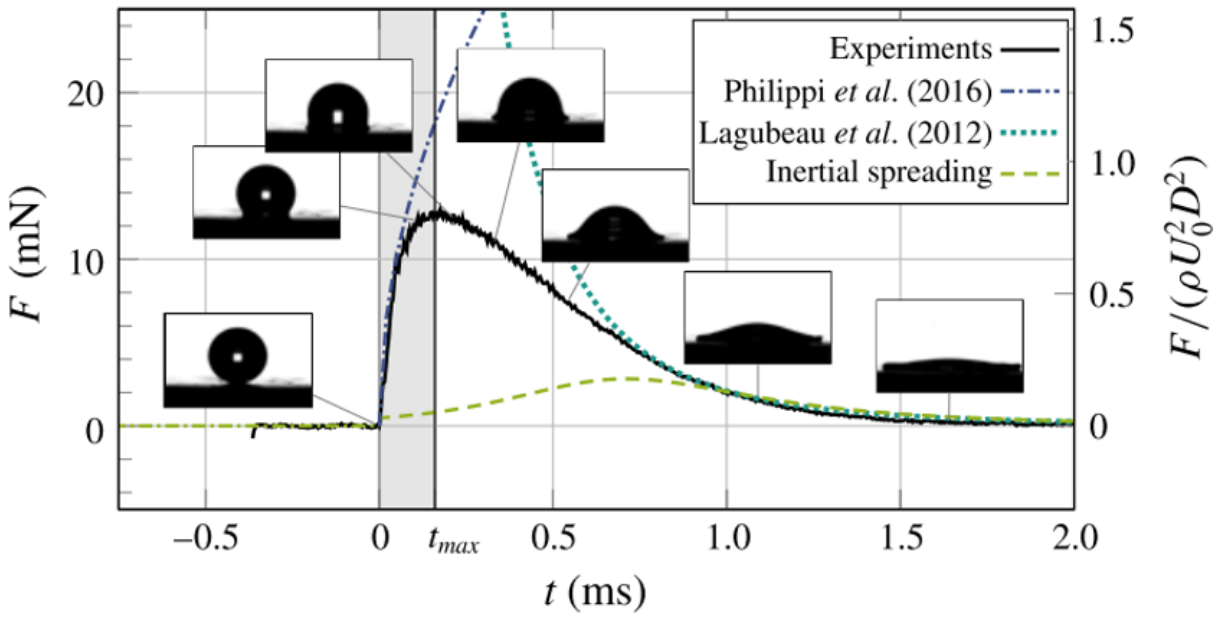

Figure 2.16: Force data as function of time from the Gordillo et al. (2018) experiments. Data shown is for a Reynolds number of 212. The blue dashed-dot line is Phillippi et al. (2016) force expression. The short-dashed line is Lagubeau et al. (2012) force computation. The long-dash green line is the inertial spreading expression proposed by Gordillo et al. (2018). Reproduced from Gordillo et al. (2018).

Figure 2.17 shows transient force data for varying Reynolds number. As the Reynolds number became smaller the force curve developed a rebound. Gordillo et al. (2018) attributed this to the use of non-Newtonian silicon oils as the droplet substance, where the droplet did not completely detach from the droplet generator.

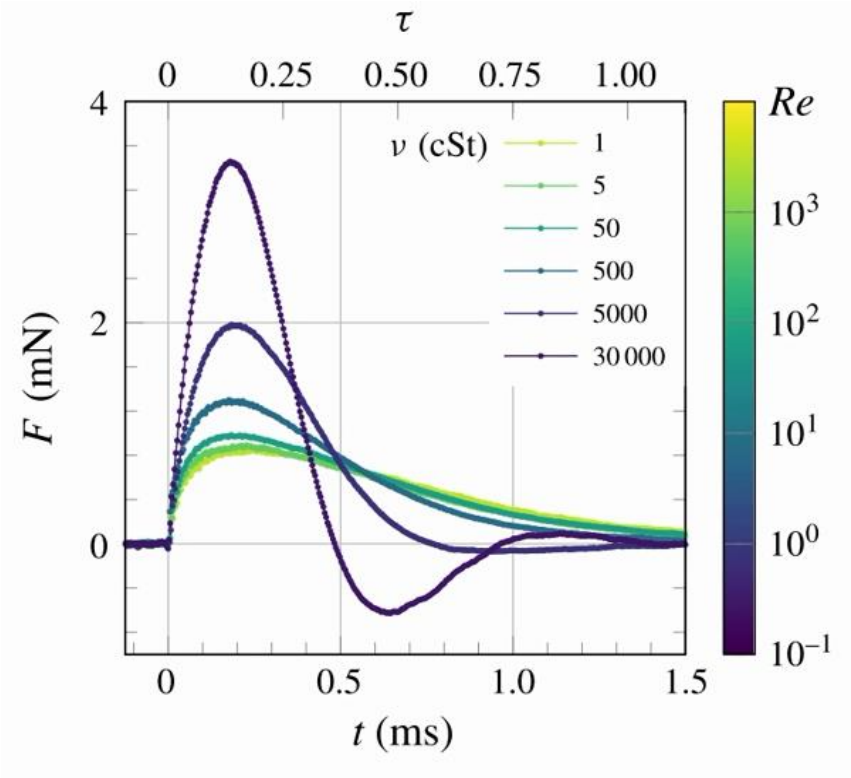

Figure 2.17: Dimensional force plotted against time. Viscosity is given in centistokes (cSt). For each droplet collision the diameter and impact velocity were kept the same, producing a wide range of Reynolds numbers. The Reynolds numbers are 0.10, 0.72, 6.9, 66, 670 and 3200, respectively. The upper x-axis is the time non-dimensionalized by the impact velocity and initial diameter. Reproduced from Gordillo et al. (2018).

The expression developed by Phillippi et al. (2016) is only valid for short times with inviscid flows, and rapidly blows up. The expression developed by Lagubeau et al. (2012) asymptotically approaches a steady value, making it suitable for long times but

cannot yield results for short times. A model that is continuous over the entire range of collision time was developed but failed to reproduce the maximum impact force (Gordillo et al., 2018). A scaling law was developed to address the maximal impact force the models could not predict (figure 2.18).

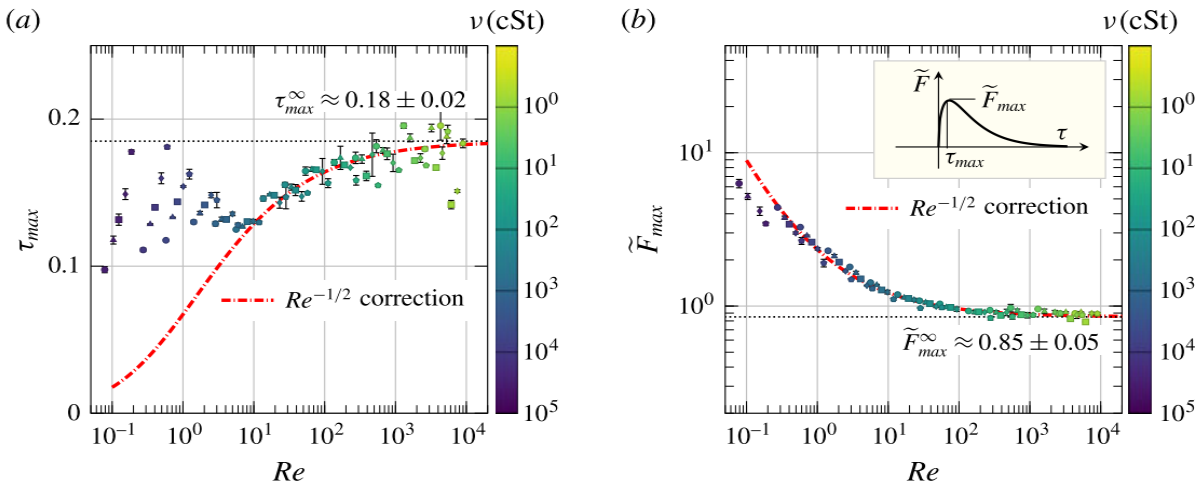

Figure 2.18: The maximum dimensionless impact force and time as functions of the Reynolds number. (a) Shows the dimensionless peak time, $\tau_{max} = (t_{max}D)/U$, and (b) shows the dimensionless maximum impact force, $\tilde{F}max = F_{max}/(\rho U^2 D^2)$. The color bars to the right of (a) and (b) indicate the decades of Reynolds data was taken for. Asymptotic values are shown for (a) and (b). The black dashed line is an asymptotic value based on averaging all data for Re > 10^3. The dash-dotted lines are model predictions given by Gordillo et al. equations (3.18) and (3.20), respectively. Reproduced by Gordillo et al. (2018).

Philippi et al. (2016) considered the short time dynamics of a single droplet impacting onto a flat solid surface. Simulations were conducted using the Gerris flow solver, an open source CFD code specialized for multiphase flow modeling and adaptive mesh refinement. The CFD results were used to develop short time asymptotic theories for the impact pressure field, impact velocity field, and spreading radius. The results

required using a variant of the Wagner theory of liquid impact to simplify the self-similar derivation. Both the pressure and velocity fields contain singularities at zero time and the origin point. Despite the singularities the asymptotic solutions are in good agreement with the numerical results over three decades of time.

The VOF formulation with surface tension modeling developed by Bussmann et al. (2000) was further advanced to include heat transfer and solidification (Pasandideh-Fard et al., 2002). Two simulations of molten tin droplets colliding with a steel surface were conducted. The first case was for normal impact onto a flat surface, conducted at a Reynolds number of 9,800. The second case was for droplet impact onto an angled flat surface, conducted at a Reynolds number of 18,800. Validation of the solidification model was done by comparing the numerical results to the Neumann solidification problem in one dimension. The overall three-dimensional solver was validated by comparing the spread factor to experimental data, and qualitatively comparing spreading images. The results were in excellent agreement with the data.

The standard fluid-wall boundary condition assumes a constant contact angle and a no-slip condition on the velocity (Bussmann et al., 2000; Hirt & Nichols, 1979). Including a relationship between the contact line speed and dynamic contact angle has been done to increase accuracy (Šikalo et al., 2005). The Hoffman relationship with an empirical model developed by Kistler (1993) was used to determine the dynamic contact angle. The main conclusion was that the dynamic contact angle is not just a function of the contact line speed. Sikalo et al. (2005) stated that the flow field near the MCL also

effects the dynamic contact angle. This conclusion is also supported by Blake et al. (1999).

The dynamic contact angle likely doesn't just depend on the contact line velocity (Blake et al., 1999; Šikalo et al., 2005). Empirical modeling reflects a case by case basis of the surface wettability and material properties. Yokoi et al. (2009) took the CLSVOF developed by Sussman et al. (2000) and introduced a dynamic contact angle formulation. The Hoffman relationship was modified is a piecewise manner, where each of the components depended on a tuning parameter. The tuning parameters were used to reflect the material and surface properties. The model was in good agreement with the authors experimental findings but required significant adjustment of the tuning parameters.

Zhou et al. (2008) used a numerical method they had developed in a previous study and applied it to a more complicated system (Li et al., 2008). The previous model was designed to simulate a non-linear wave internal a fluid droplet as it spreads out along a solid surface. The local stress in the solid was coupled to the pressure field in the fluid, which was solved from the non-linear wave equation. The model is also capable of giving the stress distribution of the impact surface. The numerical method was taken and set up to run with parameters similar to a water drop colliding with a 1Cr13 airfoil (Zhou et al., 2008). The stress distribution in the solid was used to extrapolate to the erosion of the blade.

2.3. Solidification in Gas Turbine Engine

2.3.1. Volcanic Ash Solidification

This section refers to 'solidification', as opposed to 'fusion' or 'sticking', and volcanic ash is referred to simply as 'ash'. Solidification is one of the key issues when considering particle ingestion in GTEs. When ash is ingested into a GTE it encounters the compressor blades, the combustion section, and the turbine section in that order (figure 2.19).

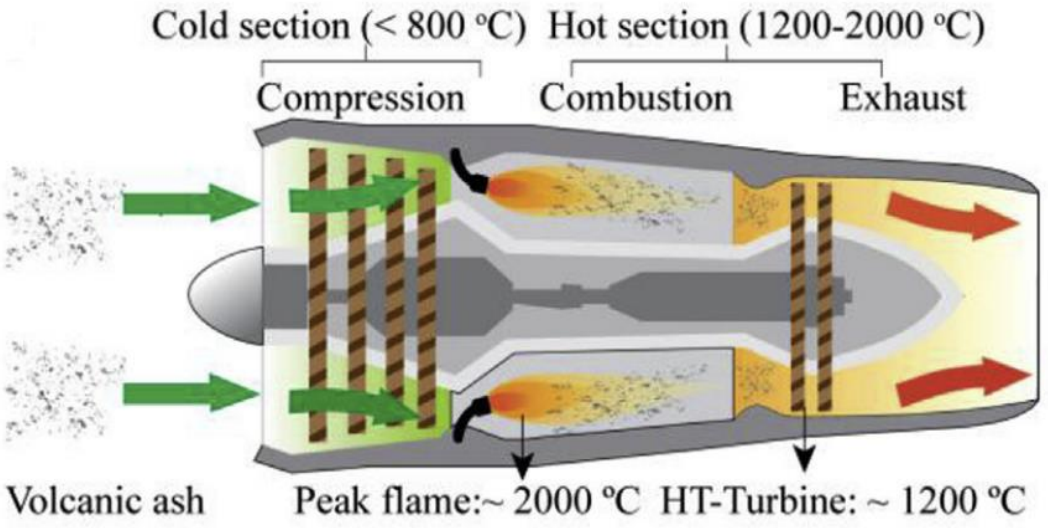

Figure 2.19: Schematic of volcanic ash ingestion into a GTE. Green arrows indicate a relatively low gas temperature, typical of ash softening. The red arrows indicate the high temperatures capable of melting the ash. The first section is the compressor blades. Then comes the combustion section indicated with peak temperature. Followed by the high temperature (HT) turbine blades at a lower temperature. Finally, the gas and particle matter are exhausted. Reproduced from Song et al. (2019).

Ash will encounter the compressor blades at a low temperature and is likely to rebound (Chen & Zhao, 2015; Dunn, 2012; Taltavull et al., 2016). After the ash passes through the compressor and combustion section it may be heated as high as 2000 °C (Song et al.,

2016). The high temperature is capable of fully melting the ash (Song et al., 2017). After melting the volcanic ash may collide with and adhere to a surface in the GTE.

The primary method for studying volcanic ash adhesion in GTEs is by attempting to experimentally reproduce the GTE conditions in a laboratory test. Experimental studies of this type can be grouped into two broad classifications. The first uses an *in-vitro* setup, where particles are shot at high velocity at a surface, representing a wall within a component of a GTE (Song et al., 2014, 2016, 2019; Taltavull et al., 2016; Walsh et al., 2006). These representative experiments are typically done to obtain detailed measurements of the effect of a specific quality of volcanic ash, such as contact angle, splat characteristics, viscosity, and other properties (Dean et al., 2016; Song et al., 2017). The second classification of experiment is one where either an actual GTE, or a model of a GTE, is used (Bonilla, 2012; Dunn, 2012). These experiments are typically done to address engine related damage (figures 3 and 4), but do not yield detailed data on individual droplet impacts. Few studies use numerical modeling to analyze volcanic ash adhesion and solidification (Kondo et al., 2018; Murugan et al., 2017). However, this can be easily supplemented by considered powder coating processes for which there is a large body of both experimental and numerical work. The numerical works of plasma coating will be discussed in section 2.3.2.

Using *in-vitro* style experimental simulations are invaluable for determining properties of volcanic ash under conditions similar to operating GTEs. Knowing the properties of the ash are a requirement for any kind of modeling. A variety of different properties are involved in the ash melting, deposition and solidification process (Song et

al., 2016). As the ash undergoes melting it will reach a critical temperature required to first adhere to a surface at a given impact velocity. Molten volcanic ash is a complex material and exhibits non-Newtonian behaviors. Characteristic temperatures have been identified to describe how ash material responds to high temperatures (figure 2.20).

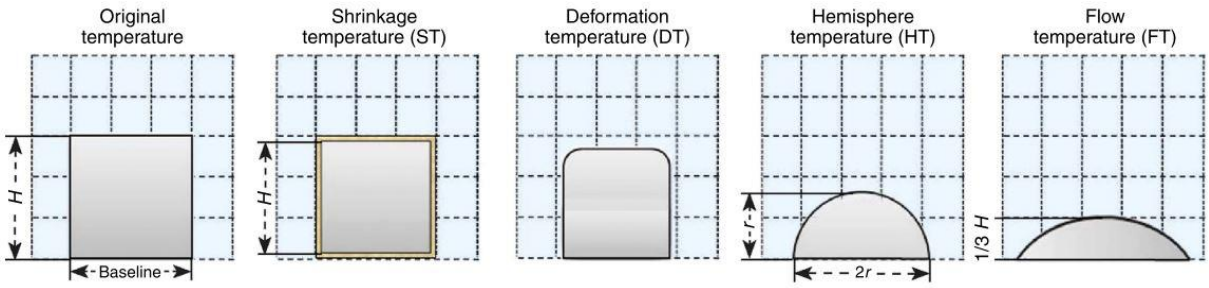

Figure 2.20: The original temperature is the sample geometry after fine volcanic ash is compressed in a cylindrical mold. Shrinkage temperature (ST) is when sintering begins to occur and porous media begins to collapse. Deformation temperature (DT) is defined as sticking to surfaces due to melting. Hemisphere temperature (HT) is defined as flowing and wetting of a surface. Flow temperature (FT) is defined as significant spreading due to gravity. Reproduced from Song et al. (2017).

The characteristic temperatures include the shrinkage temperature (ST), which is when sintering begins to occur and porous media begins to collapse; the deformation temperature (DT), defined as sticking to surfaces due to melting; the hemisphere temperature (HT) at which flowing and wetting of the material occurs; and the flow temperature (FT), identified by significant material spreading due to gravity. Song et al. (2014) was the first group to apply these characteristics to volcanic ash in an attempt to identify solidification. The samples were heated from 50 to 1400 °C at a rate of 10 °C/min while conducting simultaneous thermal analysis and differential scanning calorimeter to gain insight into the sintering and thermal properties. The sintering data

was used to identify the different characteristic temperatures. At each characteristic temperature the sample was held at isothermal conditions for a span of time to assess adhesion. The span of time a sample was held at for a characteristic temperature was determined by the sample's response to that temperature. If adhesion was achieved, flow was assessed by inclining the substrate to 70 degrees and waiting for the test material to reach a constant deformed sloped. The sample at the ST showed no adhesion to the aluminum substrate, even after 50 minutes. Without adhesion the flow properties could not be tested. At the DT the sample adhered to the substrate after 10 minutes. After 20 minutes constant flow was achieved. At the HT and FT the sample materials adhered and flowed immediately. Twenty minutes were required for constant flow. For temperatures above the ST fusion of volcanic ash becomes much more likely (Song et al., 2014).

Song et al.'s (2014) study indicated that volcanic ash melting under GTE conditions can be described by a three stage process: (1) shrinkage, (2) fusion, (3) wetting (Song et al., 2016). Shrinkage occurs at the ST, fusion occurs at the DT, and wetting occurs at the HT and FT (figure 2.21).

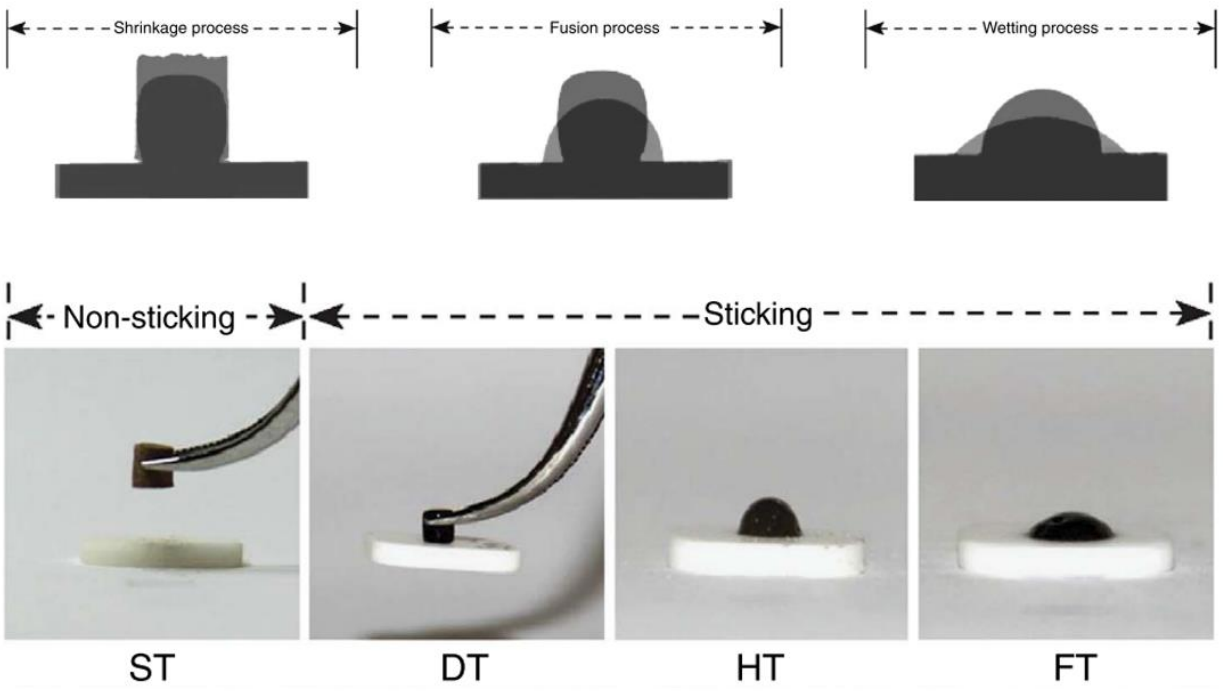

Figure 2.21: The top three images show the phases of volcanic ash melting in GTE conditions. The bottom four images show the fusion potential, also referred to as sticking. At the ST the sample does not fuse and refers to the shrinkage process. The fusion process occurs at the DT. Wetting occurs readily at the HT and FT. Reproduced from Song et al. (2016).

Song et al. (2014) addressed the characteristic temperatures in volcanic ash, and Song et al. (2016) expanded upon those ideas. In particular, it addressed sticking and heating rate. In Song et al. (2014), a single heating rate of 10 °C/min was considered. In the current study being discussed heating rates of 10, 20, 30, and 40 °C/min were considered (figure 2.22a).

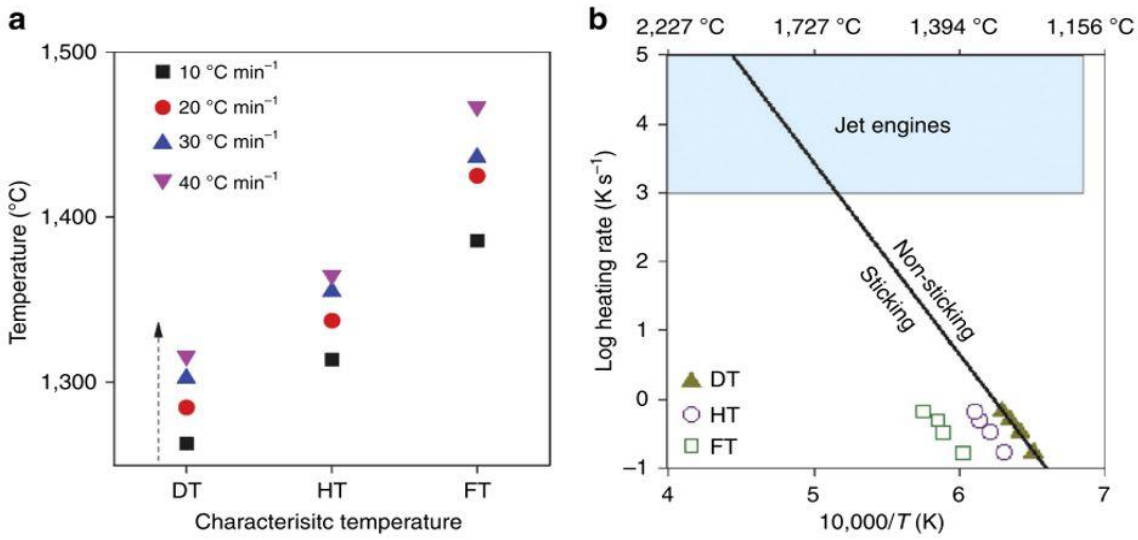

Figure 2.22: (a) Temperature in °C (y-axis) versus characteristic temperatures classification (x-axis), with varying heating rates. The heating rates are; 10 °C/min (black squares), 20 °C/min (red circles), 30 °C/min (blue triangles), and 40 °C/min (purple deltas). (b) Logarithm of the heating rate in °K/s (y-axis) versus inverse temperature as 10^4/°K. The characteristic temperatures are given as; DT (green triangles), HT (purple circles), and FT (blue squares). The solid black line is an Arrhenian fit of the temperature as a function of heating rate (r=0.99; n=4), to the left of the line ash sticks and to the right it does not. The blue box indicates the heating rate and temperature range of a GTE. Reproduced from Song et al. (2016).

The important take away from figure 2.22 is that as the heating rate increased the DT increased. This means that the sticking potential decreased with increased heating rate. The multiple heating rate DT data points were plotted against a scaled inverse temperature (figure 2.22b). The plot was fitted with a highly accurate Arrahian model (r=99) and extrapolated to heat rates more common in GTEs. However, because three decades separate the experimental heating rates and the heating rates experienced in GTEs, relevance of these observations to GTE conditions requires confirmation.

Determining the spreading and wetting properties of volcanic ash is useful for modeling purposes (Song et al., 2014, 2016, 2017). However, it is generally impossible to extrapolate these properties to an accurate description of the effects in a GTE. For this reason, macroscale experiments involving ash and GTEs much be conducted. These experiments, while important and insightful, are generally limited in their ability to identify and produce detailed data on individual droplet impact events. Much of this data is also protected by companies and not published in a form accessible by researchers. However, a limited number of studies presenting images of damaged turbine vanes (figure 1.5), turbine blades (figure 1.4), compressor blades (figure 1.2), and other components are available (Dunn, 2012).

Simulations are a useful tool that can reveal much more detailed information than experiments. Simulations specifically referencing volcanic ash adhesion in GTEs are few and far between. A multi-physics finite-element simulation has been employed to determine whether sand can melt while flowing through the combustion section of a GTE (Murugan et al., 2017). The study conducted two sets of simulations. The first was to determine is a fully molten particle could be achieved, and the second was to solve the particle laden flow field across a turbine cascade. The melt simulations were run using a two-dimensional axisymmetric first-order accurate thermal solver with particle sizes varying from 100nm-500μm. The material properties were assigned to be similar to a commonly available testing sand, AFRL 02 test sand (34 wt.% quartz, 30wt.% gypsum, 17 wt.% aplite, 14 wt.% dolomite, and 5 wt.% salt). The melting simulations were done to determine the time scales for various diameters to reach a molten or semi-molten state.

The particle-laden flow was solved with a couple finite-volume and Eulerian-Lagrangian particle injection method including chemical reactions (Bravo et al., 2016). The carrier gas was modeled using a Reynolds Averaged Navier Stokes (RANS) equation and the particle thermophysical properties were assigned to reflect SiO_2. Computational results indicated significant particle build up on the turbine blade leading edges (figure 2.23).

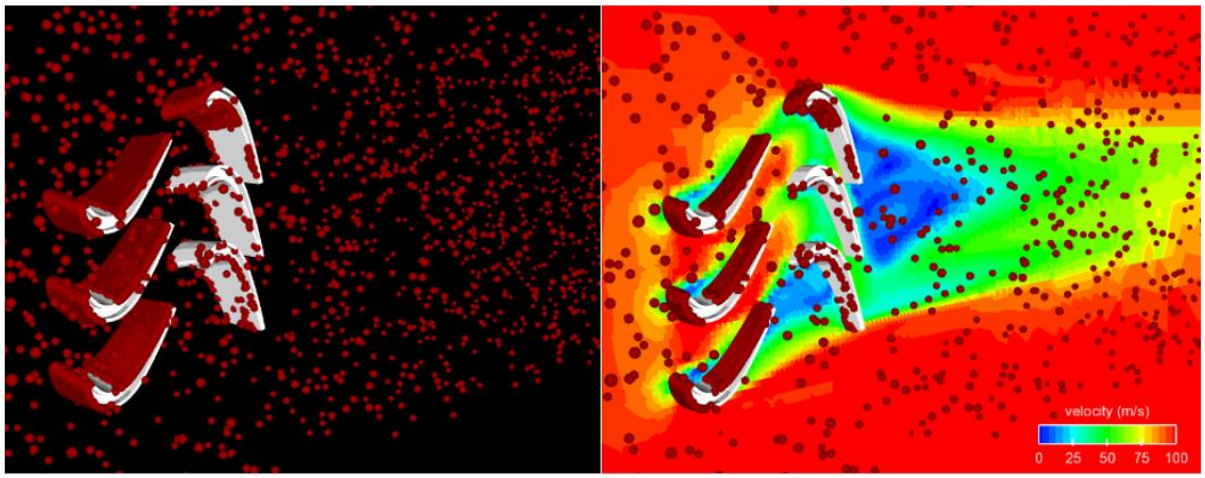

Figure 2.23: The left plot is a schematic of the turbine blade cascade, shown in white, interacting with the SiO_2 particles. The right plot shows the same time frame as the left, but with a velocity contour map over it. Reproduced from Murugan et al. (2017).

See figure 1.5 for an experiment that confirms build-up on the leading edge of the turbine guide vanes.

2.3.2. Plasma Coating Simulations

Because there is not an extensive body of literature numerically simulating volcanic ash collisions, plasma coating techniques will be discussed. Plasma coating

refers to molten or semi-molten ceramic materials impacting at high velocities against a solid surface. The length scales of a plasma coating particles range anywhere from tens to hundreds of microns (Gu & Kamnis, 2009; Saleh et al., 2014; Shinoda et al., 2005; Shinoda & Murakami, 2010). The similarities in impact velocity and length scales are why the simulation techniques are being discussed. However, the materials used in plasma coating varying greatly from the composition and properties of volcanic ash (Shinoda et al., 2005), and in particular tend to be significantly less viscous.

Kondo et al. (2018) used an explicit moving particle simulation (e-MPS) to study the collision and solidification of molten tin with a plate, which has been experimentally studied (Kondo et al., 2018; Shakeri & Chandra, 2002). The e-MPS method works essentially by representing the particle in question, the molten tin, as an ensemble of many small particles (Oochi et al., 2010). Roughly 195,000 computational particles all initially in the liquid state were used. In each particle the continuity, Navier–Stokes, and energy equations are solved. Because solidification is being studied the latent heat of a computational particle is very important. As the particle collides with the isothermal surface it begins to transfer heat, and the adjacent particles begin to transfer heat. If a computational particle reaches a prescribed melting temperature, the temperature becomes fixed. At this point the heat equation is used to calculate the heat transfer between adjacent particles, and the latent heat of the particle in question. Once the latent heat reaches zero the particle is considered solid. The numerical results were in good agreement with the available experimental data and depicted the expected fingering.

Tabbara and Gu (2011) developed a novel method for modeling the impingement of a semi molten oxide ceramic particle. The solid core of the impingement model is treated as a perfect solid that can move but cannot deform, however it can still transfer heat. The substrate surrounding the particle, the molten phase, is modeled using the VOF method which is well established. The novelty of the solver comes from the heat transfer model which couples the solid particle and molten phase, creating smooth temperature gradients across the boundaries. The spread factor of the droplet agrees reasonably well with available experimental data, with comparing splat images furthering agreement.

In the previous paragraph a novel model with obvious limitations was discussed. Zhu et al. (2015) took this idea and expanded upon it slightly by allowing for a deformable core, creating a novel coupled Eulerian and Lagrangian solver. The solver does not use the VOF method to capture the molten phase. The solver is capable of handling both molten or semi-molten ceramic particle collisions. The model considers four unique systems of equations. The first is the thermodynamic model which uses the Mie–Grüneisen equation of state. The second is a pressure equation which imbeds the relative velocity of the particle and material speed of sound in the equation. The third equation is a temperature dependent viscosity model that uses a shifted Arrhenian form. The fourth equation is a plasticity modeled applied to the material which operates for a range of temperature covering both the solid and melt regime.

Pairzi et al. (2007) simulated molten droplet collisions onto patterned surfaces. A modified VOF method including heat transfer and phase changes was used. The work was done using the material properties of molten nickel and zirconia because it is a

commonly used material in manufacturing. If the material is heated beyond 1000 °C the liquid viscosity falls below one Pa-s (Shinoda et al., 2005). The material temperature was set to match experimental data at 2390 °C, producing a viscosity of 0.03 Pa-s. The droplet size range was between 15 and 60 microns, with an impact velocity between 70-250 m/s. The reference density of the material used was 5700 kg/m^3. The results presented were for Reynolds numbers of 550 and 600. Qualitative validation was completed by comparing numerical splat images against the experimental. The key takeaway was that a VOF formulation could be used to faithfully simulate droplet splat on patterned surfaces at moderate Reynolds numbers.

CHAPTER 3

THERMAL SCALING ANALYSIS

A two-part thermal analysis was conducted to determine if the spreading process during volcanic ash droplet impingement can reasonably be approximated as being isothermal with a uniform temperature across the droplet. The first part of this study was done with scaling analyses that approximated the spreading, thermal diffusion, and convective time scales. These topics and results are covered in sections 3.1.1. and 3.1.2.. The nominal values from table 3.1. were used for all parts of the thermal analysis.

Table 3.1: Typical values of input parameters for volcanic ash impingement in gas turbine engines.

Property	Symbol	Units	Range of Values	Nominal Value
Diameter[1]	d_0	μm	3 - 30	10
Turbine Inlet Temperature[2]	T_p	°C	980 - 1370	1200
Impact Velocity[3]	V_0	m/s	130 - 450	200
Viscosity[4]	μ	Pa-s	10 - 10^5	25
Density[5]	ρ	kg/m^3	2350 - 2450	2400
Surface Tension[6]	σ	N/m	0.35 - 0.37	0.36
Thermal conductivity[7]	k	W/m-K	1 - 2	1.5
Specific heat[7]	c_p	J/g-K	0.7 - 1.7	1.2
Equilibrium contact angle[8]	θ_e	degrees	18 - 71	55

NOTES

[1]Based on a distal particle size distribution analysis, Dacre et al (2013) found that 90% of ash particles (by mass) ejected from Eyjafjallajökull volcano where in size range of 3-30

μm.
[2]Dunn (2012) examined three 1980-1990's era GTEs with turbine inlet temperatures sufficiently hot to melt volcanic ash particles. Range is TIT for these engines is given in the table.
[3]Velocity range within turbine section of GTE is from Fundamentals of Gas Turbine Engines (https://www.cast-safety.org/pdf/3_engine_fundamentals.pdf).
[4]Viscosity varies from 10 - 10^5 over the range of TIT typical of GTEs, as recorded above, based on measurements of Giordano et al (2008). Strongly dependent on temperature, but the dependency is well known and a good correlation exists. Viscosity nominal value based on measurement by Song et al (2017) at 1200°C.
[5]Based on data from Vogel et al. (2017), Wilson et al. (2012), and Shipley and Sarna-Wojcicki (1983) for amorphous volcanic glass particles.
[6]Based on data from Song et al. (2017) and Li et al. (1997). Surface tension has negligible dependence on temperature.
[7]Based on data from Büttner et al. (1998) for olivine-melilitite volcanic rock samples.
[8]Song et al (2017) found that the contact angle has a strong dependence on temperature. Nominal value used based on measurements of Song et al (2017) at 1200°C.

The second part was done using numerical approximations to assess degree of uniformity of the particle/droplet temperature profile.

Section 3.1. Scaling Analyses

Because the conduction time scale is used in both sections 3.1.1. and 3.1.2. it will be introduced here. The conduction time scale is the order of magnitude of time for thermal diffusion to occur over a given length scale. The thermal diffusivity is defined as $\alpha = k / \rho c_p$, and the length scale for particle heat conduction is the particle diameter *d*, so that the resulting conduction time scale is given by

$$\tau_\alpha = \frac{d^2}{\alpha}. \tag{3.1}$$

3.1.1. Conduction Time Scale and Convective Transport Time Scale

The convective transport time scale is the ratio of the length and velocity scales of the fluid motion. The characteristic length scale of the GTE is on the order of $L \sim 1\,\mathrm{m}$ and the velocity scale is denoted by V in table 3.1. The resulting convective time scale is

$$\tau_V = \frac{L}{V}. \tag{3.2}$$

Taking the ratio of the convective transport and conduction time scales reveal the approximate nature of how fast the particle moves through the GTE with respect to the heating time. The ratio is denoted by **Ω** and is referred to as the conduction-convection ratio, given by

$$\Omega \equiv \frac{\tau_V}{\tau_\alpha} = \frac{\alpha}{dV}\frac{L}{d}. \tag{3.3}$$

Using the nominal volcanic ash properties given in table 3.1, the conduction-convection ratio has a typical value of about 26 for ash particles in GTEs. Because this value is O(1), a more detailed analysis of temperature uniformity in advected ash particles is reported in section 3.2.

3.1.2. Conduction Time Scale and Spreading Time Scale

The spreading time scale for a liquid droplet is given by (Schiaffino & Sonin, 1997a) as

$$\tau_s = \frac{\mu}{\rho V^2}. \tag{3.4}$$

The viscosity is logarithmically dependent on temperature and chemical composition, as discussed in section 2.1.1 of the literature review. Giordano et al's. (2008) model was used to produce the results for viscosity in table 3.1, with the nominal value used in the scaling analysis. Taking the ratio of the spreading and conduction time scales revealed the approximate nature of how fast the particle solidifies as it spreads on a flat surface. This is ratio is referred to as the conduction spreading ratio, defined by

$$S \equiv \frac{\tau_S}{\tau_\alpha} = \frac{\mu}{\rho V d}\frac{\alpha}{V d}. \tag{3.5}$$

The conduction spreading ratio has a typical value of 0.0014 for ash particles in GTEs, based on the nominal properties listed in table 3.1. The fact that $S << 1$ for this application implies that the spreading process occurs much more quickly than the diffusion process. This observation implies that solidification is negligible during the spreading process. Consequently, the spreading and solidification processes can be separated, so that the droplet first experiences a nearly isothermal spreading process followed by solidification of a nearly stationary droplet.

Section 3.2. Numerical Analyses

The observation that the conduction-convection ratio for ash particles in GTEs is approximately order unity motivated us to perform a more in-depth analysis of the

particle temperature profile during passage through the GTE. This assessment was important since, if the particle temperature profile is not uniform, significant viscosity gradients within the droplet could exist during impact with the GTE surfaces. Section 3.2.1 covers the numerical method used for this assessment while 3.2.2 covers the results.

3.2.1. Crank-Nicholson Scheme and Boundary Conditions

The particle was treated as a sphere and thermal diffusion across the sphere was computed as a function of radius *r* and time *t* as the droplet traversed through the GTE. The transient temperature profile $T(r,t)$ through the sphere is governed by the energy equation

$$\frac{\partial T}{\partial t} = \alpha\left(\frac{\partial^2 T}{\partial r^2} + \frac{2}{r}\frac{\partial T}{\partial r}\right). \tag{3.6}$$

The boundary conditions at the center of the sphere and the radial edge are given by

$$\left.\frac{\partial T}{\partial r}\right|_{r=0} = 0, \tag{3.7a}$$

$$-k_p \left.\frac{\partial T}{\partial r}\right|_{r=r_o} = h\left(T|_{r=r_o} - T_\infty(x)\right). \tag{3.7b}$$

Equation (3.7a) enforces a smooth temperature gradient across the center of the particle, and (3.7b) is a mixed-type boundary condition which balances thermal conduction within the particle at the outer surface to the thermal convection away from the particle surface.

Here, k_p is the particle thermal conductivity and h is the convective heat transfer coefficient from the particle surface. A correlation for h can be expressed in terms of the Nusselt number $Nu = hd / k_f$, where k_f is the working fluid thermal conductivity. For particles moving through a gas, the Marshall-Randz relation can be used to estimate the Nusselt number as a function of the relative particle Reynolds number and Prandtl number, given by

$$Nu = 2 + 0.6 Re_p^{1/2} Pr^{1/3}. \tag{3.8}$$

Assuming that the particle moves through the GTE with approximately the same velocity as the working fluid, the particle Reynolds number Re_p in (3.8) is approximately zero and $Nu \cong 2$. This results in an expression for the temeprature gradient at the outer edge of the particle of the form

$$\left.\frac{\partial T}{\partial r}\right|_{r=r_o} = -\frac{k_f}{k_p r_o}\left(T|_{r=r_o} - T_\infty(x)\right) \tag{3.9}$$

where $T_\infty(x)$ denotes the ambient temperature of the gas within the GTE at the particle location.

A Crank-Nicholson scheme was used to simulate the transient particle temperature. The Crank-Nicholson scheme is difficult to use directly with (3.6), so a variable scaling and transformation was used of the form shown below:

$$\theta = T - T_\infty(0), \tag{3.10a}$$

$$\theta_o = \max(T_\infty) - \min(T_\infty), \tag{3.10b}$$

$$u(r,t) = \theta(r,t)r, \tag{3.11}$$

$$\frac{\partial u}{\partial t} = \alpha \frac{\partial^2 u}{\partial r^2}. \tag{3.12}$$

Here, θ denotes the difference between the temeprature at the particle location and the GTE inlet temperature. The variable transformation (3.11) converts the nonlinear equation (3.6) into a linear equation (3.12). The reduction leads to the rectangular heat equation. For convenience, these equations were nondimensionalized by

$$u' = \frac{u}{r_o\theta_o}, \qquad \theta' = \frac{\theta}{\theta_o}, \qquad r' = \frac{r}{r_o}, \qquad t' = \frac{\alpha}{r_o^2}t, \tag{3.13}$$

So (3.12) reduces to (3.14) given by

$$\frac{\partial u\prime}{\partial t\prime} = \frac{\partial^2 u\prime}{\partial r\prime^2}. \tag{3.14}$$

From here moving forward all equations will be given in non-dimensional form with the primes dropped unless otherwise specified. Applying the scaling, variable transformation, and nondimensionalization as well as defining $\eta = k_f/k_p$ and $\theta_\infty(x) = T_\infty(x) - T_\infty(0)$ gives the final results for the boundary conditions, equations (3.15a and 3.15b).

$$u|_{r=0} = 0 \tag{3.15a}$$

$$\left.\frac{\partial u}{\partial r}\right|_{r=1} + u|_{r=1}(\eta(t) - 1) = \frac{\eta(t)\theta_\infty(t)}{\theta_o} \tag{3.15b}$$

A particle initial temperature profile was chosen as constant across the radius and equal to the GTE inlet temperature which is defined as $T_\infty(0)$. The initialization is then given as $u|_{t=0} = 0$.

The latent heat of melting is set to zero since the particle is an amorphous solid (Shinozaki et al., 2013). The carrier gas in the GTE was treated as air with temperature dependent thermal conductivity. With the boundary conditions, initialization, and governing equation, the Crank-Nicholson scheme was employed to numerically approximate the heat equation and a second-order predictor-corrector method was used to track the particle location in the GTE. Particle diameters of 3, 10 and 30 μm were used. Two different GTE data sets with different peak temperatures were used, one having relatively low temperature peak (900 °C) and the other with higher temperature peak (1800 °C). The high peak data used for the computation is shown in figure 3.1.

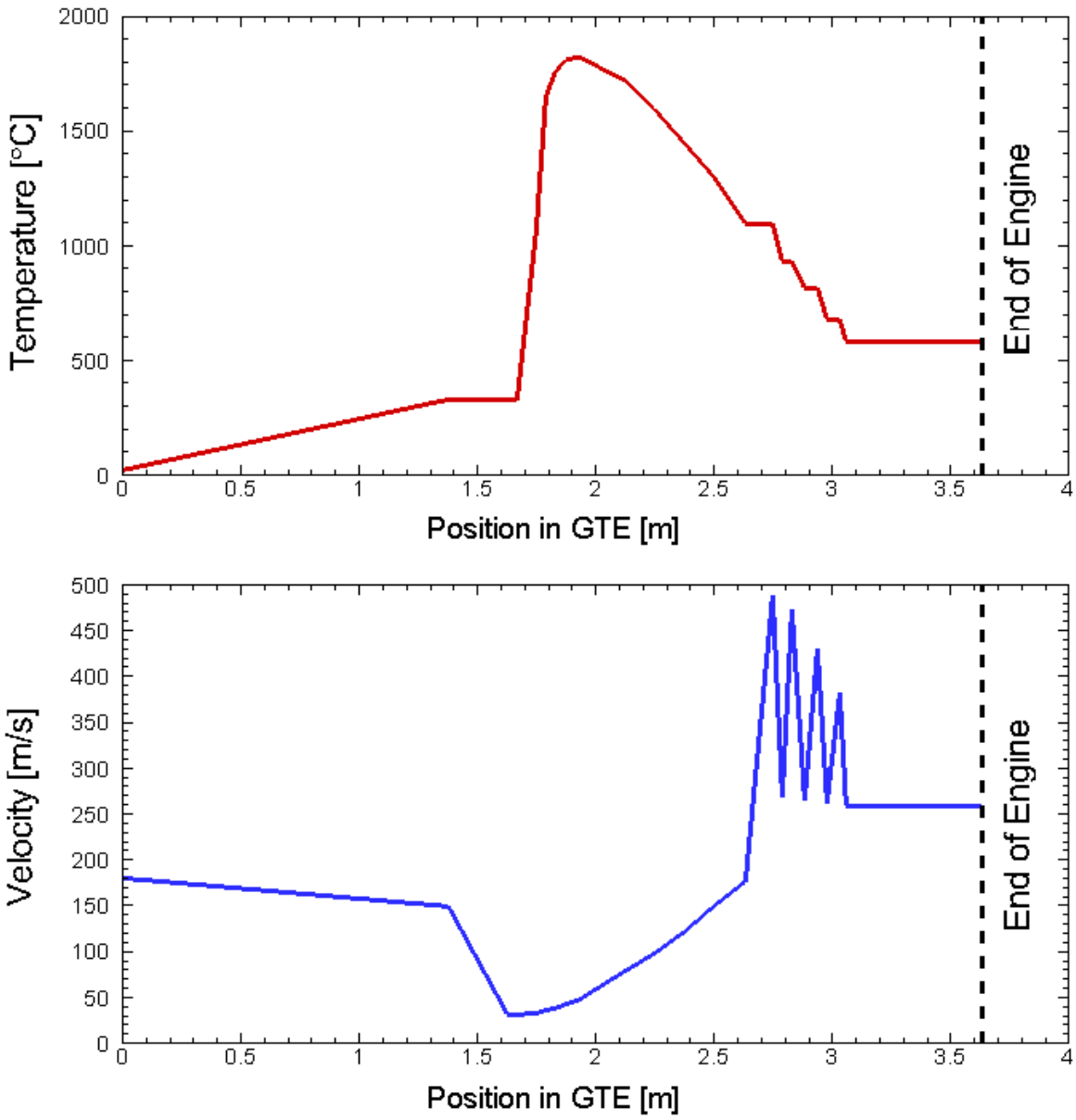

Figure 3.1: In both the top and bottom plots the x-axis the position in the GTE given in meters. In the top plot the y-axis is the reference frame temperature of the GTE. In the bottom plot the y-axis is the reference frame velocity used in predictor-corrector algorithm. The vertically dashed black line indicates the end of the engine in both plots, at approximately 3.6 meters.

The results for the high peak and low peak engine data were similar, so only the results from the high peak data are discussed. The material properties used for the volcanic ash

are given in table 3.1. With the numerically calculated temperature profiles the viscosity was determined from (2.1). The three coefficients in (2.1) were taken to be *A*=-4.55, *B*=7720 J/mol, and *C*=344 K (Giordano et al., 2008). The method of Giordano et al. (2008) used to determine the coefficients, as discussed in section 2.1.2..

3.2.2. Numerical Results

The variation of the particle surface temperature and the particle surface viscosity is plotted in figure 3.2 for 3, 10, and 30 μm diameter particles as functions of particle position in the gas turbine engine.

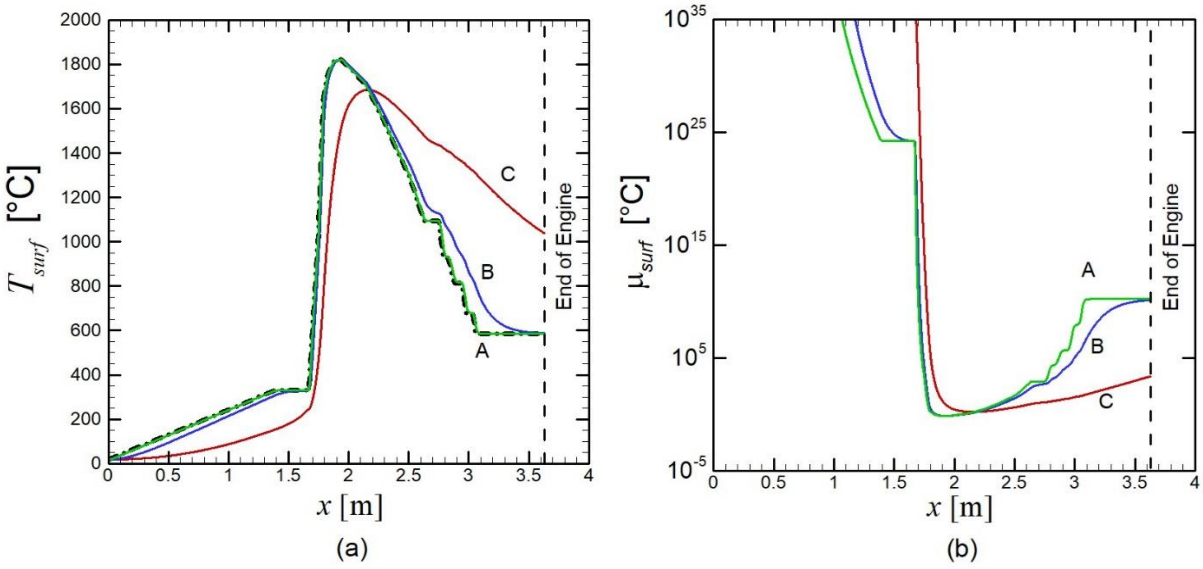

Figure 3.2: Variation of (a) the particle surface temperature $T_{surf}(t)$ and (b) the particle surface viscosity $\mu_{surf}(t)$ as functions of position *x* in the gas turbine engine for particles with diameter of 3 μm (green line, A), 10 μm (blue line, B), and 30 μm (red line, C). The gas turbine engine fluid temperature T_f is plotted as a black dashed-dotted line in (a).

The particle surface temperature changes by about 1800 °C and the viscosity changes by approximately 35 orders of magnitude as the particle travels through the engine. Computations for 3 μm diameter particles indicate that the surface temperature value almost exactly follows the GTE fluid temperature and the temperature profile across the particle is very close to uniform. The change in the particle surface temperature is seen to lag the change in the ambient GTE fluid temperature by a slight amount for the 10 μm particle and by a significant amount for the 30 μm particle. The peak temperature within the engine is also observed to be lower for the 30 μm particle than for the 10 μm particle, although due to its larger thermal mass, the 30 μm particle remains hotter with a significantly lower viscosity for a much longer period of time than the smaller particles. This difference is significant since it is this rear region of the engine, downstream of the thermal peak, where particle deposition on the turbine blades and nozzle guide vanes is observed to occur.

The temperature variation in the radial direction across the particle can be characterized by the difference between the surface and the center, $\Delta T(t) = T(r_0, t) - T(0, t)$. The temperature difference is plotted as a function of time for the three particle sizes in figure 3.3.

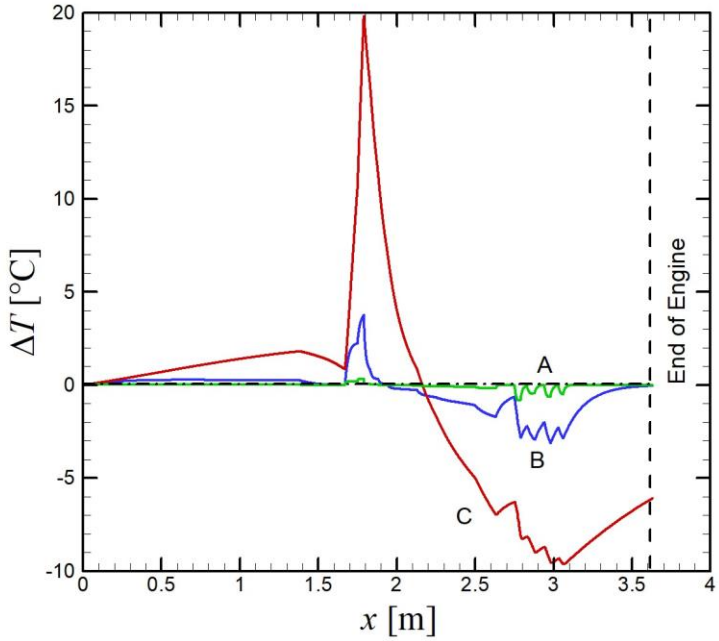

Figure 3.3: Plot of temperature difference between particle surface and center as a function of position *x* in the gas turbine engine for particles with diameter of 3 μm (green line, A), 10 μm (blue line, B), and 30 μm (red line, C).

The temperature difference is largest in the region where the temperature increases rapidly at the entrance of the hot section of the GTE (at about x = 1.75 m), since in this region the slope of the temperature variation is almost vertical. The temperature difference exhibits a negative peak near the end of the engine hot section, at about x = 3 m.

Results for the maximum absolute value and the root-mean-square value of the temperature difference $\Delta T(t)$ are listed in table 3.2 for each of the three particle sizes. Here, ΔT_m is defined by

$$\Delta T_{rms} = \left[\frac{1}{N}\sum_{i=1}^{N}(\Delta T(t) - \Delta T_m)^2\right] \tag{3.16}$$

where ΔT_m is the mean value of $\Delta T(t)$ as the particle moves through the engine.

Table 3.2: Maximum and root-mean square (rms) values of the difference in temperature between the particle surface and center, $\Delta T(t) \equiv T(r_0, t) - T(0, t)$, and of the viscosity difference ratio $\Delta\beta(t) \equiv \{\mu[T(r_0, t)] - \mu[T(0, t)]\}/\mu[T(r_0, t)]$ for three particle diameters.

Profile Measure	**3 μm diameter**	**10 μm diameter**	**30 μm diameter**
Max $\lvert\Delta T\rvert$ $^\circ C$	0.839	3.77	19.8
RMS ΔT $^\circ C$	0.115	1.01	6.71
Max $\lvert\Delta\beta\rvert$	0.0341	0.239	3.97
RMS $\Delta\beta$	0.00567	0.0572	0.928

Also listed in table 3.2 is the maximum absolute value and root-mean square value of the viscosity difference ratio

$$\Delta\beta = \frac{\mu[T(r_0, t)] - \mu[T(0, t)]}{\mu[T(r_0, t)]} \tag{3.17}$$

which represents the difference between the particle surface and center viscosity divided by the surface viscosity.

Bearing in mind that the maximum temperature within the GTE is approximately $T_{max} = 1800℃$, we see that the maximum temperature difference across the particle is only about 0.05%, 0.2% and 1.1% of T_{max} for the 3, 10 and 30 μm diameter particles, respectively. The maximum value of the temperature difference occurs on the nearly vertical section of the temperature profile near *x* = 1.7 m, and the value in other parts of

the GTE is significantly lower. Correspondingly, the root-mean-square temperature difference across the particle is much smaller, measuring only about 0.006%, 0.06%, and 0.4% of T_{max} for the three particle diameters, respectively. Since the viscosity varies exponentially with temperature, as indicated by (2.1), the maximum and root-mean-square values of the viscosity difference ratio $\Delta\beta(t)$ listed in table 3.2 are significantly larger than the temperature ratios listed above. For instance, the maximum and root-mean-square values of the viscosity difference ratio for the 10 μm diameter particle are about 24% and 5.7%, respectively. However, these values should be interpreted in light of the 35 orders of magnitude variation in particle viscosity as it passes through the GTE.

CHAPTER 4

COMPUTATIONAL METHOD

Section 4.1. Computational formulation

Computations were conducted of droplet impingement onto a flat surface using the finite-volume based formulation in ANSYS Fluent v19.2 and employing the combined level-set volume-of-fluid (CLSVOF) method to represent the droplet fluid and the external fluid phases (Griebel & Klitz, 2017; Sun & Tao, 2010; Sussman & Puckett, 2000). The flow field was computed in polar cylindrical coordinates (r, θ, z), with axisymmetric velocity profile given by

$$\mathbf{u} = u(r,z,t)\mathbf{e_r} + w(r,z,t)\mathbf{e_z}. \tag{4.1}$$

The governing equations for the fluid flow are based on the assumption of an incompressible Newtonian viscous fluid with viscosity μ and density ρ that are functions of the level-set function ϕ, given by

$$\nabla \cdot \mathbf{u} = 0 \tag{4.2}$$

$$\rho(\phi)\left[\frac{\partial \mathbf{u}}{\partial t} + (\mathbf{u}\cdot\nabla)\mathbf{u}\right] = -\nabla p + \nabla\cdot\left[\mu(\phi)(\nabla\mathbf{u} + \nabla\mathbf{u}^T)\right] - \mathbf{F}_{sf} \tag{4.3}$$

The level-set function ϕ is equal to $+\phi_0$ in the liquid phase, $-\phi_0$ in the gas phase, and 0 on the gas-liquid interface, where ϕ_0 is a prescribed constant. The level-set function ϕ is evolved in time using the standard equation

$$\frac{\partial \phi}{\partial t} + \nabla \cdot (\mathbf{u}\phi) = 0 . \tag{4.4}$$

The level-set function is regularly re-initialized using the geometrical interface-front construction method to preserve the property $|\nabla \phi| = 1$ (Sethian, 1999).

The distributed surface tension force $\mathbf{F}_{sf}$ is evaluated using an extension of the Brackbill et al. (1992) equation as

$$\mathbf{F}_{sf} = 2H(\phi)\delta(\phi)\sigma\kappa\mathbf{n} \tag{4.5}$$

where the interface unit normal **n** and mean curvature κ are defined by

$$\mathbf{n} = \frac{\nabla \phi}{|\nabla \phi|_{\phi=0}}, \quad \kappa = \nabla \cdot \mathbf{n} . \tag{4.6}$$

A phase-smoothed Heaviside function $H(\phi)$ and Dirac delta $\delta(\phi)$ can be defined for an interface with thickness *a* as (Croce et al., 2010)

$$H(\phi) = \begin{cases} 0 & \text{for } \phi < a \text{ (gas phase)} \\ 1 & \text{for } \phi > a \text{ (liquid phase)} \\ \frac{1}{2}[1+\frac{\phi}{a}+\frac{1}{\pi}\sin(\frac{\pi\phi}{a})] & \text{for } -a < \phi < a \text{ (interface)} \end{cases} \tag{4.7}$$

$$\delta(\phi) = \begin{cases} 0 & \text{for } |\phi| > a \\ \dfrac{1+\cos(\pi\phi/a)}{2a} & \text{for } -a < \phi < a \end{cases} \tag{4.8}$$

The fluid density and viscosity were specified in terms of the values (ρ_ℓ, μ_ℓ) in the liquid and the values (ρ_g, μ_g) in the gas as

$$\rho(\phi) = [1 - H(\phi)]\rho_g + H(\phi)\rho_\ell \tag{4.9a}$$

$$\mu(\phi) = [1 - H(\phi)]\mu_g + H(\phi)\mu_\ell \tag{4.9b}$$

A block-structured mesh containing four blocks was generated using the ANSYS meshing utility, as shown in figure 4.1a.

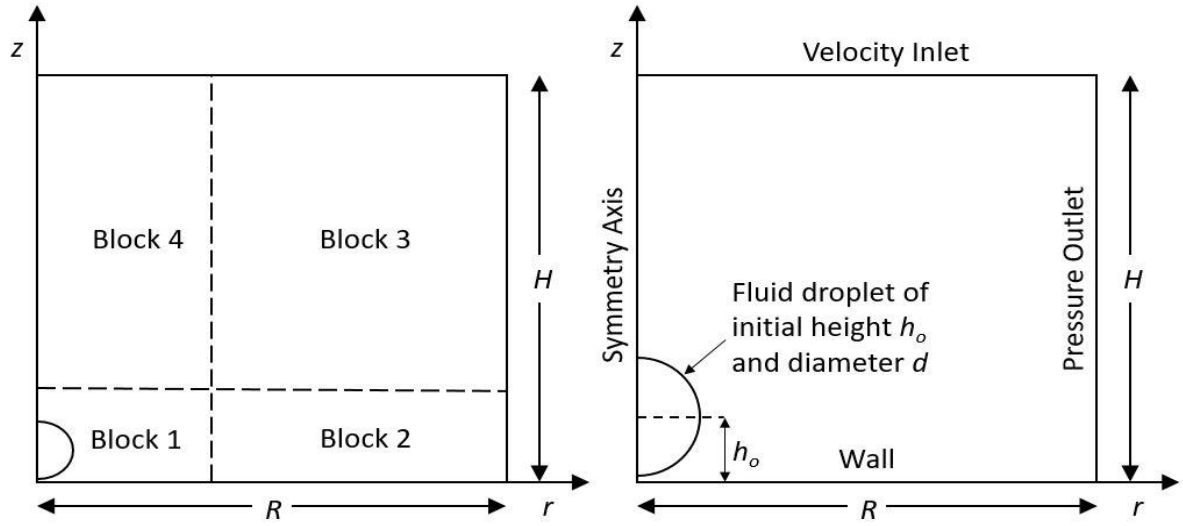

Figure 4.1: Plots illustrating the computational domain, of height H and radius R. Here r and z are the radial and axial coordinates, respectively. In (a), the four blocks of the multi-block structured grid are indicated. The plot in (b) shows the droplet initial configuration and the boundary conditions on the domain sides.

The mesh is uniform in blocks 1 and 3, with the mesh size is set equal to a value L_e in block 1 and 0.62 in block 3. In blocks 2 and 4, the mesh gradually varied from the small grid size in block 1 to the large grid in block 3. A fully implicit coupled pressure and velocity solver was used to solve equations (4.2) and (4.3) on the block-structured grid. The momentum equation (4.3) and the level-set equation (4.4) were solved using a second-order upwind scheme. The pressure interpolation was performed using the PRESTO! (PREssure STaggering Option) scheme, and gradients were computed using a cell-based least-squares method.

The domain initial and boundary conditions are shown in figure 4.1b. The droplet is entrained in a downward axisymmetric stagnation-point flow. A uniform downward velocity was set at the velocity inlet, and the no-slip condition was prescribed at the wall

boundary. In order to enhance computational stability, the density and viscosity of the gas phase were set to 1000 times smaller than the liquid phase. The offset distance between the droplet surface and the wall at the initial time was set equal to one-tenth of the droplet diameter. The transient droplet solution was initialized using a steady-state solution for the gas phase. All variables in the computations were non-dimensionalized using the initial droplet diameter *d*, the impact velocity V_0, and the liquid density ρ_ℓ as

$$\mathbf{u}' = \mathbf{u}/V_0, \qquad \mathbf{x}' = \mathbf{x}/d, \qquad p' = p/\rho_\ell V_0^2, \qquad t' = tV_0/d. \tag{4.10}$$

Primes on dimensionless variables are dropped in the remainder of the paper for convenience.

CHAPTER 5

COMPUTATIONAL RESULTS

Direct computations of droplet impingement were performed using the dimensionless parameters listed in table 5.1.

Table 5.1: Computed parameters for melted volcanic ash in gas turbine engines.

Property	**Symbol**	**Equation**	**Units**	**Range of Values**	**Nominal Value**
Weber number	We	$\rho d V_0^2/\sigma$	none	320 - 42,500	2667
Reynolds number	Re	$\rho d V_0/\mu$	none	$0.9*10^{-5}$-3.3	0.19
Ohnesorge number	Oh	$\mu/\sqrt{\rho d\sigma}$	none	$61\text{-}2.0*10^{6}$	273
Bond number	Bo	$\rho g d^2/\sigma$	none	$5.6*10^{-7}$-$6.2*10^{-5}$	$6.5*10^{-6}$
Spreading velocity	U	$\rho V_0^2 d/\mu$	m/s	0.0012 - 1490	38
Collision time	τ_C	$\mu/\rho V_0^2$	μs	0.020 - 2500	0.26

To maximize computational efficiency, a variable time stepping method was used with maximum Courant number of 0.75. The grid size near the contact line was selected as L_e=0.006.

5.1. Results for a Typical Low Reynolds Number Case

Typical results for volcanic ash transported in a gas turbine engine (Case 2, with *Re* = 0.19) are plotted in figure 5.1 showing a time series of the velocity magnitude both inside and external to the droplet during collision.

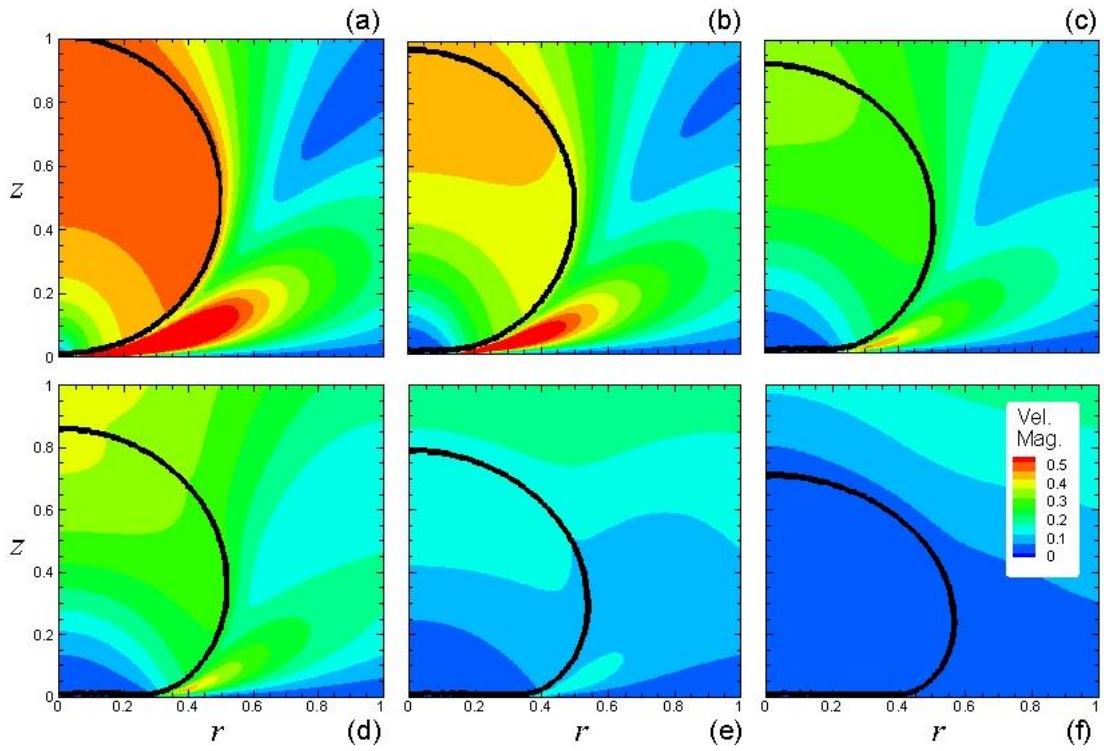

Figure 5.1: Time series of computational results for Case 2 (Re = 0.19) showing contours of the velocity magnitude at times (a) t = 0.016, (b) 0.156, (c) 0.238, (d) 0.360, (e) 0.560 and (f) 0.938. The $\phi = 0$ surface indicating the droplet interface is identified by a solid black line.

The droplet surface ($\phi = 0$) is indicated using a solid black line. The droplet first makes contact with the surface in figure 5.1a, at which time the velocity within the droplet is nearly unchanged from the initial state, save for a decrease in velocity magnitude within a small region surrounding the collision point. The external fluid exhibits a high-velocity jet away from the droplet along the impact surface, as the squeeze-film is emptied of fluid by the impinging droplet. Figure 5.1b-e show the droplet flattening as the contact line moves outward along the impact surface. The velocity magnitude rapidly decreases both within the droplet and external to the droplet. A jet of external fluid is emitted from the

vicinity of the contact line in figure 5.1b-c due to the corner flow in this region, but the magnitude decreases rapidly.

The pressure field internal to the droplet is shown in figure 5.2a at t =0.29.

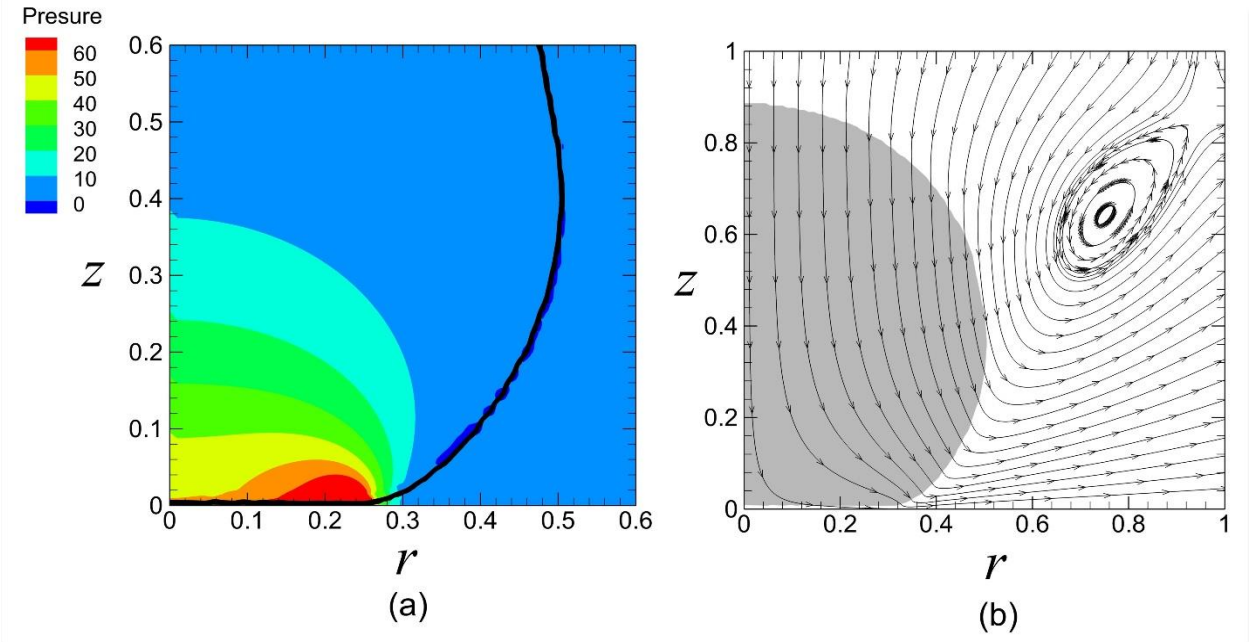

Figure 5.2: Contour plots of (a) the droplet pressure field and (b) the smoothed Heaviside function $H(\phi)$, with velocity streamlines, for Case 2 at time t = 0.29. The solid line in (a) denotes the droplet interface $\phi = 0$, and the shaded region in (b) indicates the interior of the droplet.

A region of high pressure is observed along the impact surface, just inward of the contact line. This pressure field is very similar to that obtained in the droplet impact simulations of Philippi et al. (2016) and Eggers et al. (2010). Figure 5.2b shows contours of the step function $H(\phi)$ indicating the fluid phase at a time of 0.29, where the grey region of the plot indicates the region inside the droplet. Streamlines of the velocity field are also shown. The presence of a recirculating vortical flow in the external fluid streamlines just outside of the impacting droplet is similar to the flow structures present in the numerical

computations of droplet impingement by Guo et al. (2016). The phase plot in figure 5.2b exhibits a thin strip along the bottom surface of the droplet in which the phase transitions back to the external fluid. This strip, which was a common feature observed in computations that we performed for low Reynolds number droplet impingement, is consistent with observations of air film formation beneath impinging droplets made by numerous researchers (Hicks & Purvis, 2010; Kolinski et al., 2012; Liu et al., 2013; Thoroddsen et al., 2003, 2005). Experimentally studies indicate that this air film beneath impacting droplets is sometimes very thin, only a few tens of nanometers thick (Kolinski et al., 2012).

Theories for droplet impingement on surfaces (Attané et al., 2007; Bechtel et al., 1981; Kim & Chun, 2001) typically utilize a balance between the rate of change of potential and kinetic energy in the droplet and the rate of energy dissipation. Consequently, it is of interest to examine the contours of some of these energy terms within the droplet. A time series showing the contours of the kinsetic energy $\frac{1}{2}H(\phi)(u^2 + w^2)$ for Case 2 is presented in figure 5.3 for the same six times as used in Figure 5.1.

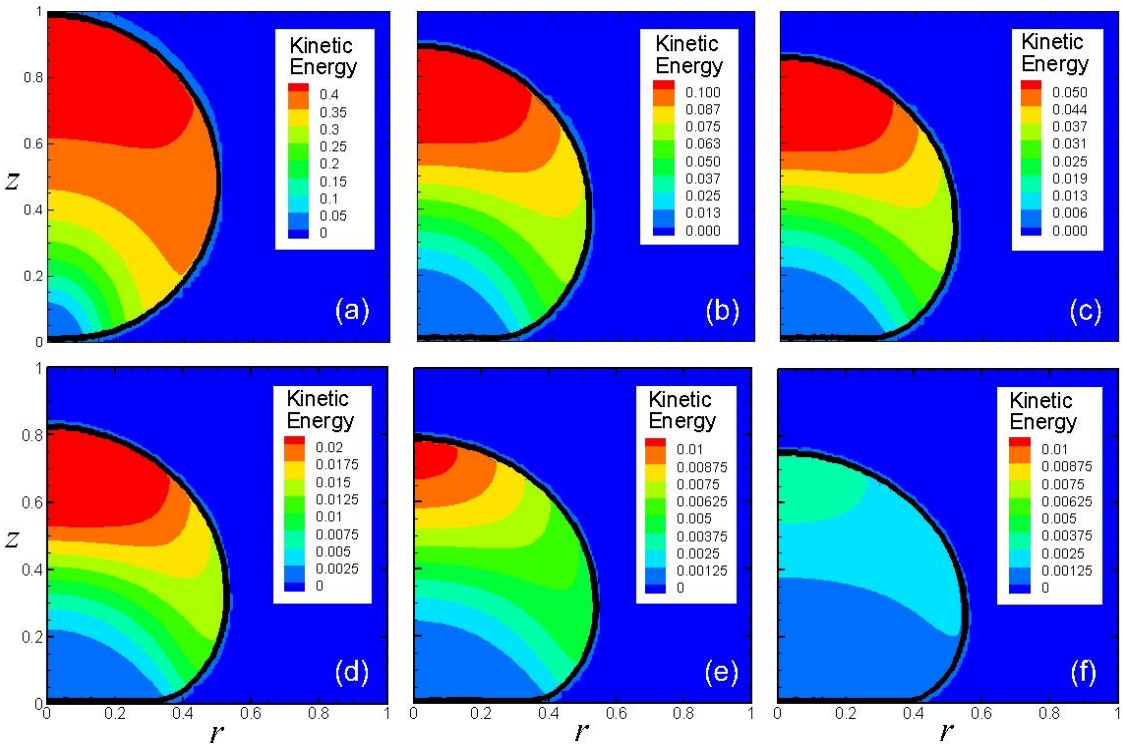

Figure 5.3: Time sequence showing the kinetic energy contours within the droplet for Case 2 at the six times plotted in figure 5.1. The $\phi = 0$ surface indicating the droplet interface is identified by a solid black line. Contour levels in each frame are not equivalent.

The kinetic energy contour levels are reset at each time frame since the value of kinetic energy decreases significantly during the time series. The value of the kinetic energy gradually increases with height and with radius within the droplet at any time during the spreading process.

A time series of the contours of the rate of hydraulic energy dissipation π_h (nondimensionalized by $\rho_\ell d^2 V_0^3$) within the droplet is plotted in figure 5.4, which is defined by

$$\pi_h(r,z,t) = \frac{2H(\phi)}{Re}\left[\left(\frac{\partial u}{\partial r}\right)^2 + \left(\frac{u}{r}\right)^2 + \left(\frac{\partial w}{\partial z}\right)^2 + \frac{1}{2}\left(\frac{\partial u}{\partial z} + \frac{\partial w}{\partial r}\right)^2\right]. \quad (5.1)$$

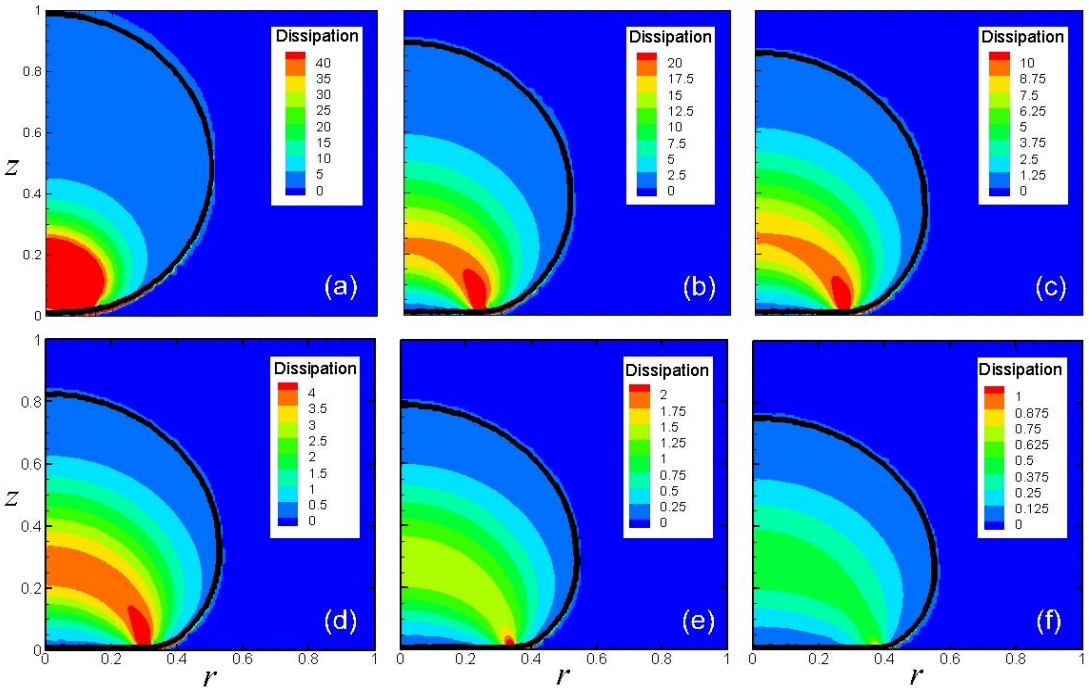

Figure 5.4: Time sequence showing the contours of the rate of energy dissipation within the droplet for Case 2 at the six times plotted in figure 5.1. The $\phi = 0$ surface indicating the droplet interface is identified by a solid black line. Contour levels in each frame are not equivalent.

At the droplet contact time in figure 5.4a, the energy dissipation rate is dominated by a region surrounding the contact point, and it is small in the upper part of the droplet. As the droplet spreads on the impacting surface, the magnitude of the energy dissipation rate decreases but the region with significant values of energy dissipation rate spreads out over a wide region within the droplet. We note that most theories for droplet impingement at high Reynolds number assume that all energy dissipation occurs within a thin boundary layer lying between the droplet and the impact surface (Bechtel et al.,

1981; Kim & Chun, 2001). By contrast, our direct computation results for energy dissipation rate at low Reynolds number exhibit significant energy dissipation rate values within the body of the droplet and relatively small dissipation rate along the impact surface (except very close to the contact line).

5.2. Reynolds Number Effect

The effect of Reynolds number on the droplet impingement computations was examined by repeating the above computations with four different Reynolds number values over the interval $0.05 \leq Re \leq 10$, with the same value of *We* (see Table 3.1). The computed contact radius r_c and the droplet center of mass height z_m are plotted in figure 5.5 as functions of time for *Re* values of 0.05, 0.19, 1 and 10.

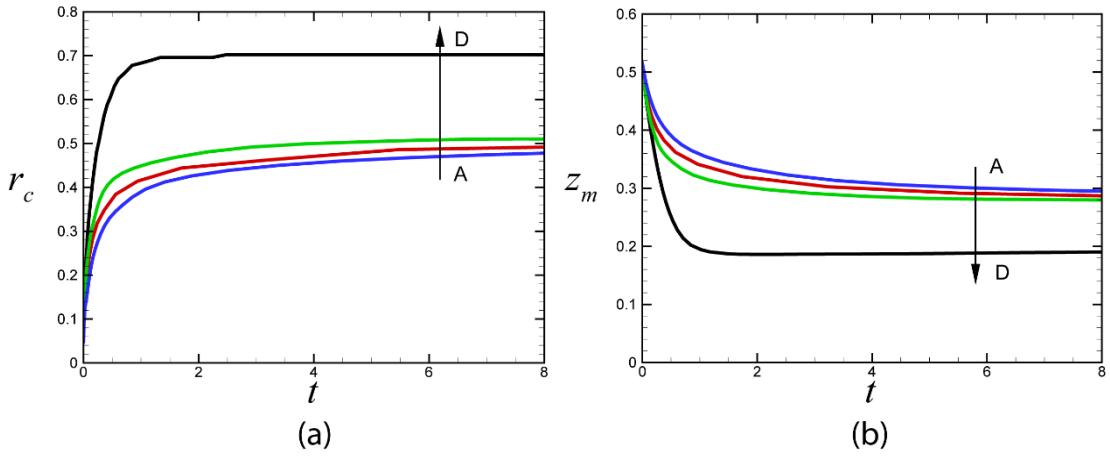

Figure 5.5: Effect of Reynolds number on droplet (a) contact radius r_c and (b) center of mass height z_m as functions of time. The Reynolds number is indicated by the capital letters A to D, and the solid black arrow indicates a decreasing Reynolds number. The Reynolds numbers shown are 0.05 (A, blue), 0.19 (B, red), 1 (C, green), 10 (D, black).

The maximum spread factor is observed to increase as the Reynolds number increases.

A comparison of our computational results for time variation of the contact radius with experimental data and analytical predictions from other investigators is shown in figure 5.6, which is shown using a log-log plot.

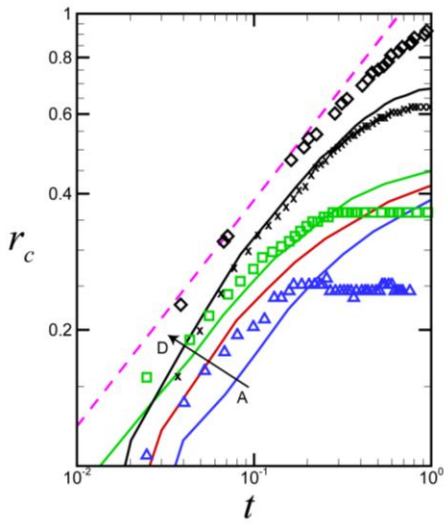

Figure 5.6: Plot of contact radius versus time, using a log-log scale. The solid black arrow indicates an increasing Reynolds number. The computed data is indicated by solid lines, with Reynolds numbers of 0.05 (A, blue), 0.19 (B, red), 1 (C, green), and 10 (D, black). Data from Gordillo et al. (2018) is plotted using deltas, squares, and crosses for Reynolds numbers of 0.11, 0.7, and 7, respectively. Data from Rioboo et al. (2002) for Reynolds number of 9 is plotted using diamonds. The dashed line indicates the Philippi et al. (2016) analytical expression for short-time droplet spreading.

Our computational data is plotted as solid curves, with decreasing contact radius as the Reynolds number increases (as indicated by the arrow from A to D). The computational results are compared to experimental data for low Reynolds number droplet impingement obtained by Gordillo et al. (2018) for Reynold's numbers of 0.11, 0.7, and 7 and by Rioboo et al. (2002) for a Reynolds number of 9. The experimental data is colored in

figure 5.6 using the same color as the computational prediction with the nearest computational Reynolds number. A short-time analytical result from Philippi et al. (2016) based on approximate solution of the inviscid flow equations is also plotted in figure 5.6, which can be written in dimensionless form as

$$r_c = \sqrt{3t/2}\,. \tag{5.2}$$

Both the computational results and the experimental data exhibit the trend that the contact radius decreases with decrease in Reynolds number. The Philippi et al. (2016) invsciid flow solution yields a higher contact radius than any of the finite Reynolds number computational or experimental results. The log-log plot in figure 5.6 indicates that both our computational results and the comparison experimental data agrees with the $\sim t^{1/2}$ trend predicted by the Philippi et al. (2016) solution for short times.

In comparing the quantitative predictions between our computational data and the comparison experimental results, it should be kept in mind that the highly viscous liquids used in these experiments tend to also exhibit significant viscoelastic behavior. The effect of viscoelasticity on inhibiting the droplet spreading was pointed out by Gordillo et al. (2018) as a major reason why the contact radius in their experimental data was substantially lower than indicated by extrapolation of power law predictions made from higher Reynolds number data. Viscoelastic effects in the experimental data is therefore a likely reason for why the Gordillo et al. (2018) experimental results for contact radius suddenly plateau at finite time, which is a behavior not observed in the computations or theory, or in the higher Reynolds number experimental results.

We have also examined the total kinetic and potential energy of the droplet, E_c and E_p, which can be written in dimensionless form as $e_c = E_c/(\rho_l d^3 V_0^2)$ and $e_p = E_p/(\rho_l d^3 V_0^2)$. The potential energy consists of both gravitational potential energy and interfacial potential energy. The potential energy is given by the sum of the air-liquid interfacial energy σA_{GL} and the liquid-solid interfacial energy $\pi R_c^2 \sigma_{SL}$, minus the interfacial energy $\pi R r_c^2 \sigma_{SG}$ that was present before the surface was covered by the liquid. Here, A_{GL} is the area of the liquid-gas interface, R_c is the contact line radius on the planar solid substrate, and σ, σ_{SL} and σ_{SG} denote the liquid-gas, solid-liquid and solid-gas surface tensions, respectively. The resulting interfacial potential energy is given by

$$E_p = \sigma A_{GL} + \pi R_c^2 (\sigma_{SL} - \sigma_{SG}). \tag{5.3}$$

Young's equation defines the equilibrium contact angle θ_e by

$$\sigma \cos\theta_e = \sigma_{SL} - \sigma_{SG} \tag{5.4}$$

so that (5.3) reduces to

$$E_p = \sigma (A_{GL} - \pi R_c^2 \cos\theta_e). \tag{5.5}$$

Nondimensionalizing the interfacial area and the contact radius using the droplet radius *d* as $a_{GL} = A_{GL}/d^2$ and $r_c = R_c/d$, the potential energy can be written in dimensionless form as

$$e_p = \frac{1}{We}(a_{GL} - \pi r_c^2 \cos\theta_e). \tag{5.6}$$

The dimensionless kinetic energy within the droplet is given by

$$e_c = \frac{1}{2}\int_V H(\phi)(u^2 + w^2)dv. \tag{5.7}$$

Plots of the time variation of e_p and e_c are shown in figure 5.7 for the same Reynolds number values examined in figure 5.6.

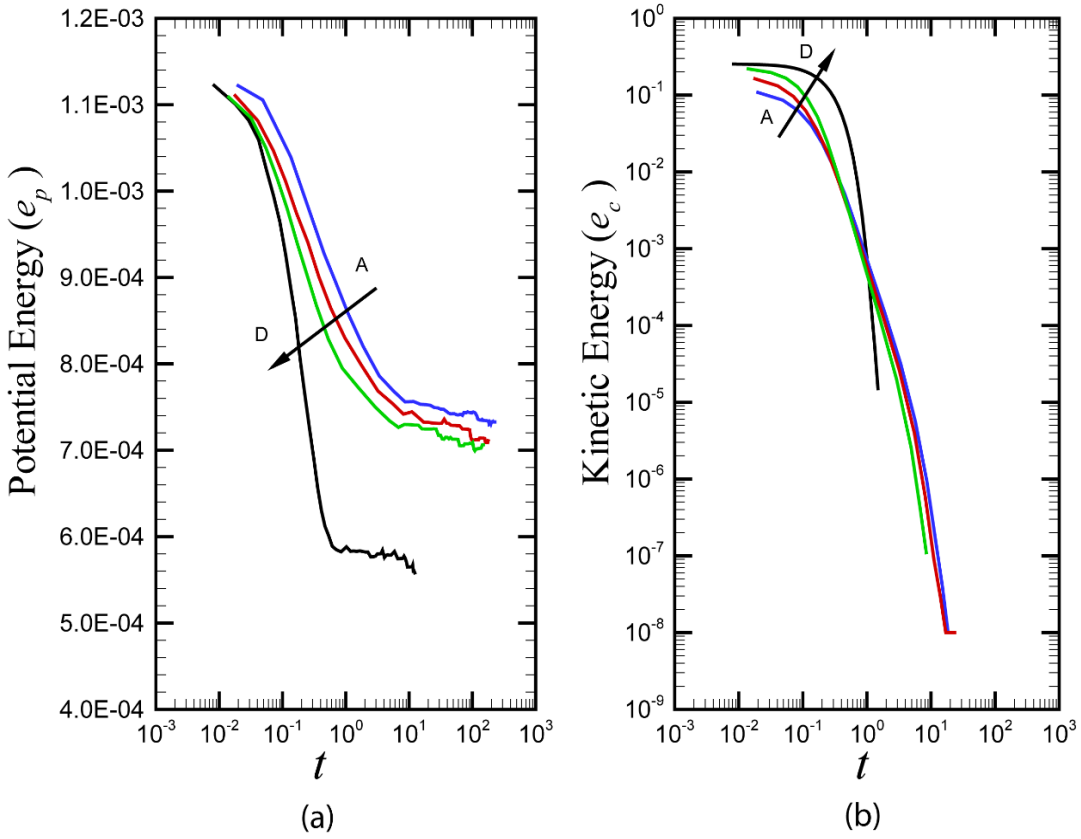

Figure 5.7: Reynolds number effect on (a) semi-logarithmic plot of the potential energy and (b) log-log plot of the kinetic energy within the droplet as functions of time. The Reynolds number is indicated by the capital letters A to D, and the solid black arrow indicates a decreasing Reynolds number. The Reynolds numbers shown are 0.05 (A, blue), 0.19 (B, red), 1 (C, green), 10 (D, black).

A log-log plot is used for the kinetic energy since it reduces rapidly following droplet impact. The potential energy flattens out at a value between 50-60% of the value for the initial spherical droplet, whereas the kinetic energy decreases by nearly eight orders of

magnitude during the computation. The potential energy of the droplet is observed to decrease as the Reynolds increases. This trend is further examined in figure 5.8, where the product of potential energy and Weber number in the long-time steady state configuration of the droplet is plotted versus Reynolds number both for our computational results and for and values calculated from the droplet impingement videos given in the Gordillo et al. (2018) supplementary information.

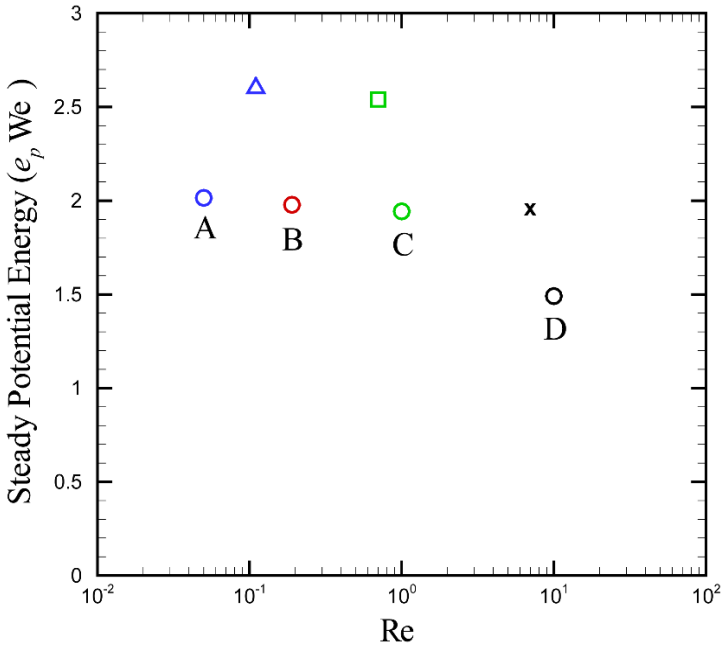

Figure 5.8: Plot of the steady potential energy multiplied by the Weber number (e_p We) versus the Reynolds number. The circular symbols indicate the steady values from our simulations, with Reynolds numbers 0.05 (A, blue), .019 (B, red), 1 (C, green), 10 (D, black). The delta (Δ), square (□), and cross (x) indicate values computed from the experimental video data from Gordillo et al. (2018).

The multiplication by *We* in figure 5.8 was used to normalize the data, as suggested by (5.1), since our computations and the Gordillo et al. (2018) experiments were conducted

at different Weber number values. Both our computations and the Gordillo et al. (2018) experiments indicate a decrease in potential energy as the Reynolds number increases.

Figure 5.9 shows the droplet shape and contours of the local dissipation rate plotted at two different times for three different Reynolds numbers.

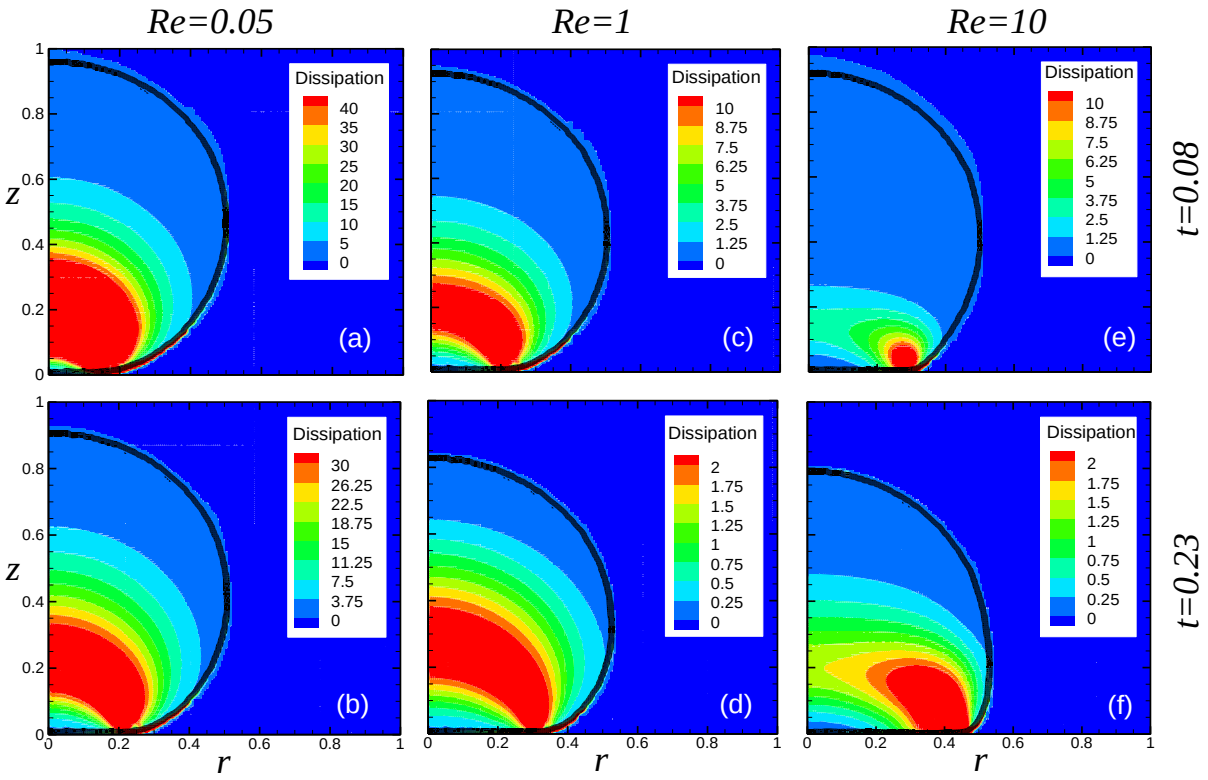

Figure 5.9: Local dissipation rate at two times and three different Reynolds numbers. Frames (a), (c), (e) are at time of 0.08 and frames (b), (d), (f) are at time 0.23. Frames (a) and (b) are Reynolds number 0.05. Frames (c) and (d) are Reynolds number 1. Frames (e) and (f) are Reynolds number 10. The $\phi = 0$ surface indicating the droplet interface is identified by a solid black line. Contour levels in each frame are not equivalent.

The dissipation rate is largest in the low Reynolds number cases, and it occurs over a larger fraction of the droplet volume. This trend is expected because the dissipation defined in (5.1) scales with the inverse Reynolds number. The velocity gradients in (5.1)

define the shape of the contours. For the *Re* =10 case, the dissipation rate is dominated by velocity gradients near the contact line, whereas dissipation rate is more spread out in the low Reynolds number cases.

5.3. Velocity Profile Within the Droplet

An important feature of many theoretical models for impacting droplets is the need to assume a velocity profile within the droplet. The droplet flow field is often assumed to have the form of an inviscid stagnation-point flow (Bechtel et al., 1981; Eggers et al., 2010; Kim & Chun, 2001; Pasandideh-Fard et al., 1996), such that

$$u = sr \qquad\qquad w = -2sz \tag{5.8}$$

where the straining rate $s(t)$ is determined by an additional boundary condition, such as the kinematic condition $w(0,h,t) = \dot{h}$ at the top of the droplet. This form of velocity profile is appropriate at sufficiently long times after impact for cases with high Reynolds numbers. Since the radial velocity in (5.8) does not satisfy the no-slip condition, the droplet is assumed to have a thin boundary layer underneath it in which most of the viscous dissipation occurs. Alternatively, Madejski (1976) developed a theory using a cylinder model for the lamellar film that forms at long time as a droplet spreads on the surface, in which the radial velocity was assumed to have the linear shear form

$$u = czr \qquad\qquad w = -cz^2 \tag{5.9}$$

where $c = c(t)$ is a coefficient with SI dimensions of 1/m-s. This velocity profile is more appropriate for droplet impact cases with low Reynolds number at long time, as the radial velocity satisfies the no-slip condition on the substrate surface.

A similarity theory for droplet impact for short times after impact was developed by Philippi et al. (2016) based on solution of the potential flow equations, which gives droplet velocity and pressure fields as a function of time after impact for cases with high droplet Reynolds numbers. Philippi et al. (2016) also provide a solution for the viscous boundary layer flow lying under the self-similar inviscid flow within the droplet, where the boundary layer velocity field varies as a function of $z\sqrt{\mathrm{Re}/t}$, in agreement with the classical Stokes impulsive motion solution. Similar results are noted by Wildeman et al. (2016) based on computational solution of droplet impacts with Reynolds number in the interval $100 \leq Re \leq 1000$.

In the current subsection, we explore the direct computation results for droplet impingement to determine a reasonable approximate form for the velocity profile within the droplet that is appropriate for low Reynolds number collisions. One common feature of the velocity profiles in (5.8) and (5.9) is that the axial velocity component *w* is approximately independent of radius *r*, at least near the central and middle parts of the droplet. This feature is examined in figure 5.10, in which the axial velocity is plotted as a function of height at three different radial locations (r = 0, 0.15 and 0.3) and at different times during the droplet impact. It is observed that at each of these times, the velocity profile at each radial location is very similar, indicating that the axial velocity can reasonably be assumed to be independent of radius, or $w = w(z,t)$, for low Reynolds number droplet impingement problems. In this case, the radial velocity can be obtained from the axisymmetric continuity equation as

$$u(r,z,t) = -\frac{r}{2}\frac{\partial w}{\partial z}. \tag{5.10}$$

We seek a functional fit for the radial and axial velocity profiles which satisfies the no-slip and no-penetration boundary condition on the substrate surface, which from (5.10) requires that $w = \partial w/\partial z = 0$ on $z = 0$. Satisfaction of these boundary condition can be ensured by approximating the gradient of the axial velocity as proportional to a log-normal distribution $f(z)$, such that

$$\frac{\partial w}{\partial z} = -C_{LN} f(z) = -\frac{C_{LN}}{\sigma_{LN} z\sqrt{2\pi}} \exp\left(-\frac{(ln\, z - \mu_{LN})^2}{2\sigma_{LN}^2}\right) \tag{5.11}$$

and from (5.10)

$$u = \frac{C_{LN} r}{2} f(z) \tag{5.12}$$

Here C_{LN}, μ_{LN} and σ_{LN} are undetermined fitting coefficients. The axial velocity profile $w(z,t)$ can be obtained by integrating (5.11) to obtain

$$w(z,t) = -C_{LN}[\Phi(z) - \Phi(0)] \tag{5.13}$$

where $\Phi(z) = 1 - \frac{1}{2}\text{erfc}\left[\frac{\ln z - \mu_{LN}}{\sqrt{2}\sigma_{LN}}\right]$ is the cumulative normal distribution and erfc(·) is the complementary error function.

A plot demonstrating these functional fits for the case with *Re* = 0.19 is given in figure 5.10.

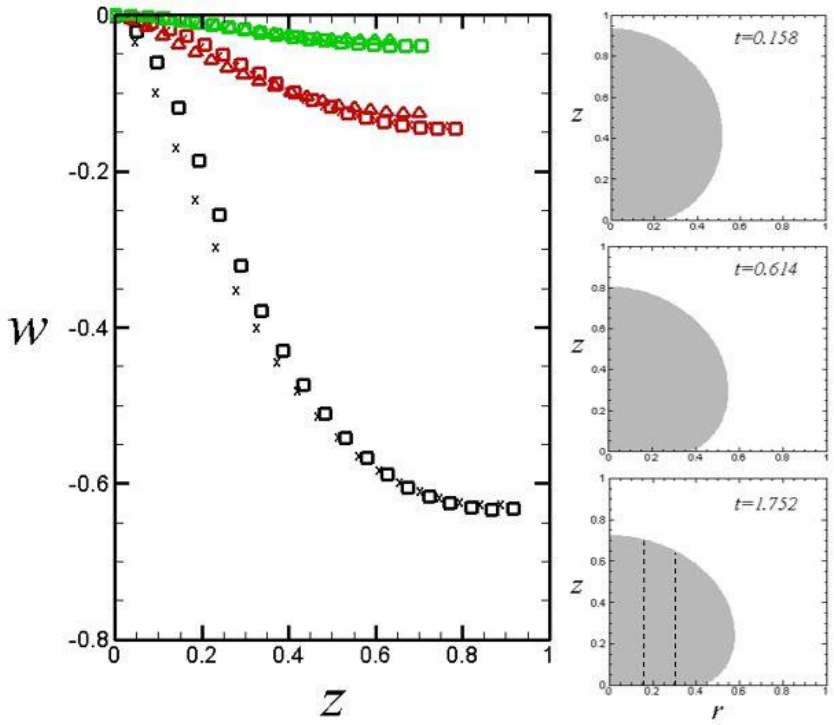

Figure 5.10: Computational results for the axial velocity $w(r,z,t)$ as a function of height z at times t = 0.158 (black), 0.614 (red), and 1.752 (green). Results are compared at three radial locations, r = 0 (squares), r = 0.15 (crosses), and r = 0.30 (deltas), demonstrating that the axial velocity depends only weakly on radius within the body of the droplet. The droplet shape for the three times shown is indicated in the inset plots on the right, with the radial cuts at r = 0.15 and r = 0.30 indicated in the bottom plot.

The radial velocity profile at r = 0.15 was fit using (43), which is shown in figure 5.11a.

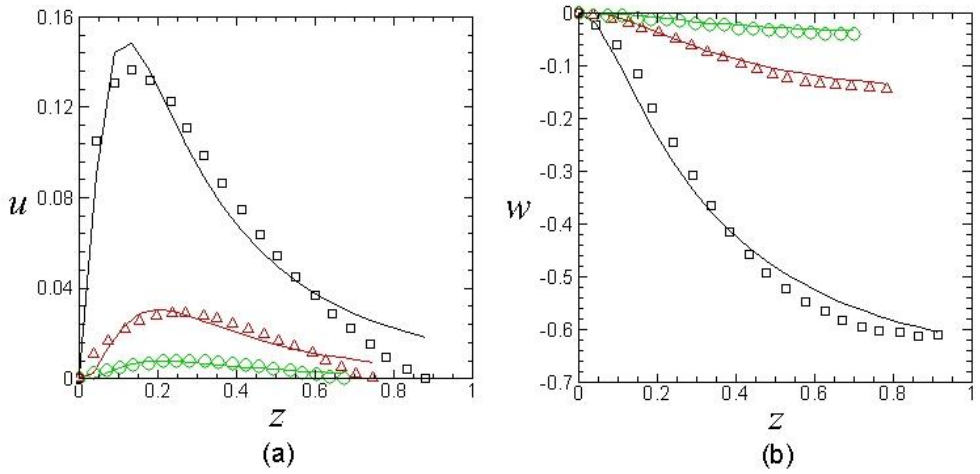

Figure 5.11: Plots showing (a) radial velocity profile in z at $r = 0.15$ and (b) axial velocity profile in z at $r = 0$ for the case with Re = 0.19 at times $t = 0.168$ (black squares), 0.614 (red deltas), and 1.752 (green circles). The curves in (a) are best-fit log-normal curves of the form (5.12) with coefficients given in table 5.2, which end on the droplet boundary. The curves in (b) were computed using (5.13) with the same coefficients as the curves in (a).

The best-fit coefficient values were obtained by searching for values yielding minimum least-square error with increment sizes $\Delta C_{LN} = 0.008,\ \Delta\mu_{LN} = 0.004,\ \Delta\sigma_{LN} = 0.002$. Corresponding plots for the axial velocity profile were obtained using (45) with the same coefficient values as used for the curves in figure 5.11a. The resulting predictions for axial velocity profiles are shown in figure 5.11b to be in excellent agreement with axial velocity data taken along the symmetry axis ($r = 0$). This procedure was repeated for the velocity profiles obtained for computations with all four Reynolds number values listed in table 5.2, and the best-fit values for the coefficients C_{LN}, μ_{LN} and σ_{LN} are plotted in figure 5.12 as functions of Reynolds number.

Table 5.2: Listing of parameter values in different computational cases examined.

Case	Weber	Reynolds	Ohnesorge
1	2666	0.05	1032
2	2666	0.019	271
3	2666	1	51
4	2666	10	5

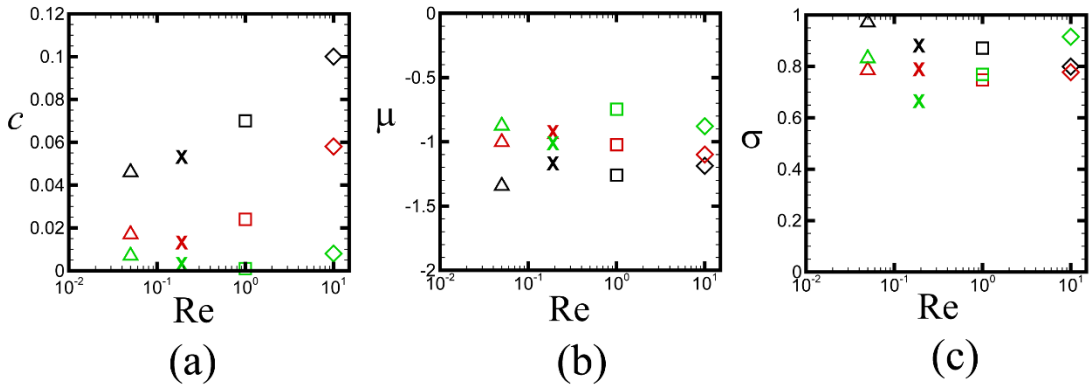

Figure 5.12: Plots of the best-fit values for the log-normal coefficients (a) *C*, (b) μ, and (c) σ for the radial velocity profile, for times $t = 0.168$ (black), 0.614 (red), and 1.752 (green) and for Reynolds numbers 0.05 (deltas), 0.19 (crosses), 1 (squares), and 10 (diamonds).

The data indicate that μ_{LN} and σ_{LN} are approximately constant while C_{LN} decreases significantly in time. We also do not see any clear trend in values of μ_{LN} and σ_{LN} with Reynolds number, but rather the values of scattered around mean values of approximately -1.1 and 0.85, respectively.

5.4. Droplet Shape During Impact

It is also necessary in many analytical theories for droplet impact to assume a family of shapes for the droplet. Common choices are a truncated sphere or a cylinder (Attané et al., 2007), although other options such as the rimmed cylinder or cylinder with spherical rims are sometimes employed. A comparison of the computed droplet shape over a series of times during droplet impingement with the popular cylinder and truncated sphere shapes is given in figure 5.13 for the *Re* = 0.19 case.

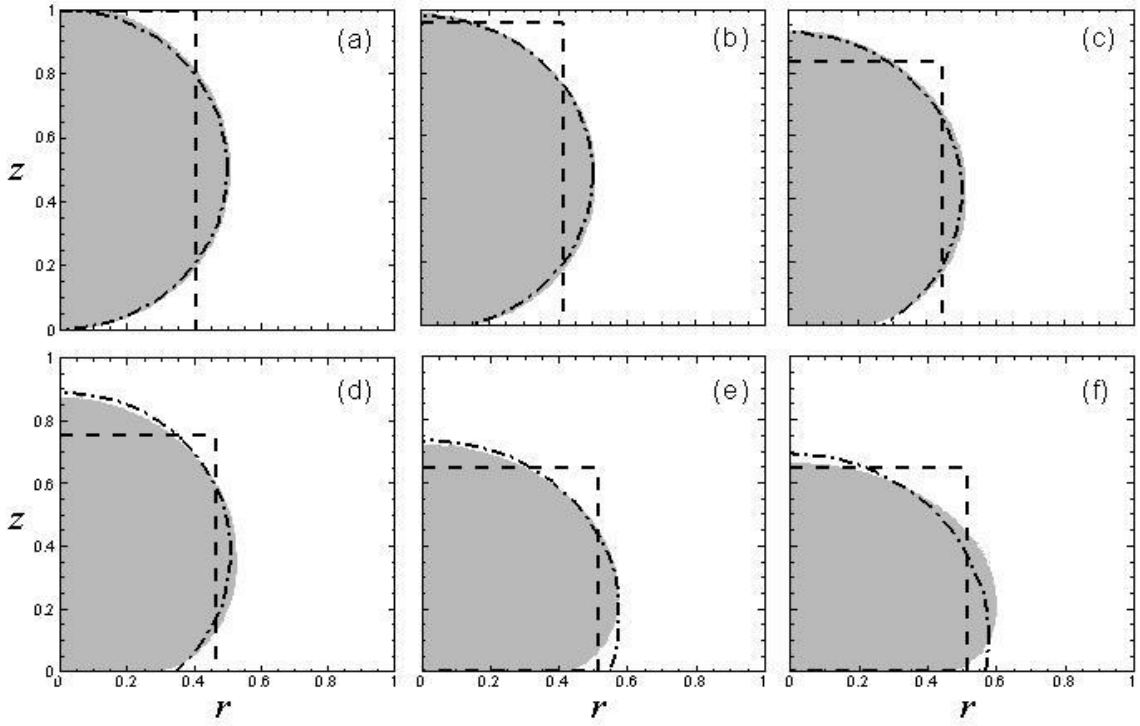

Figure 5.13: Time series of plots showing computed phases (grey = droplet and white = external fluid) at the same times as in figure 5.1, compared to a truncated sphere (dashed-dotted line) and a cylinder (dashed line) with the same volume and center-of-mass.

The cylinders and truncated spheres shown for comparison have the same volume and center of mass as the computed droplet. It is apparent from these results that the truncated sphere is an excellent approximation of the droplet shape during the early stages of droplet impingement, and even for long times remains a reasonable approximation to the computed profile.

In figure 5.14 a time series showing the droplet shapes (in grey shading) and velocity vectors during droplet impingement are compared for cases with two Reynolds numbers: Re = 0.19 (on the left) and Re = 10 (on the right).

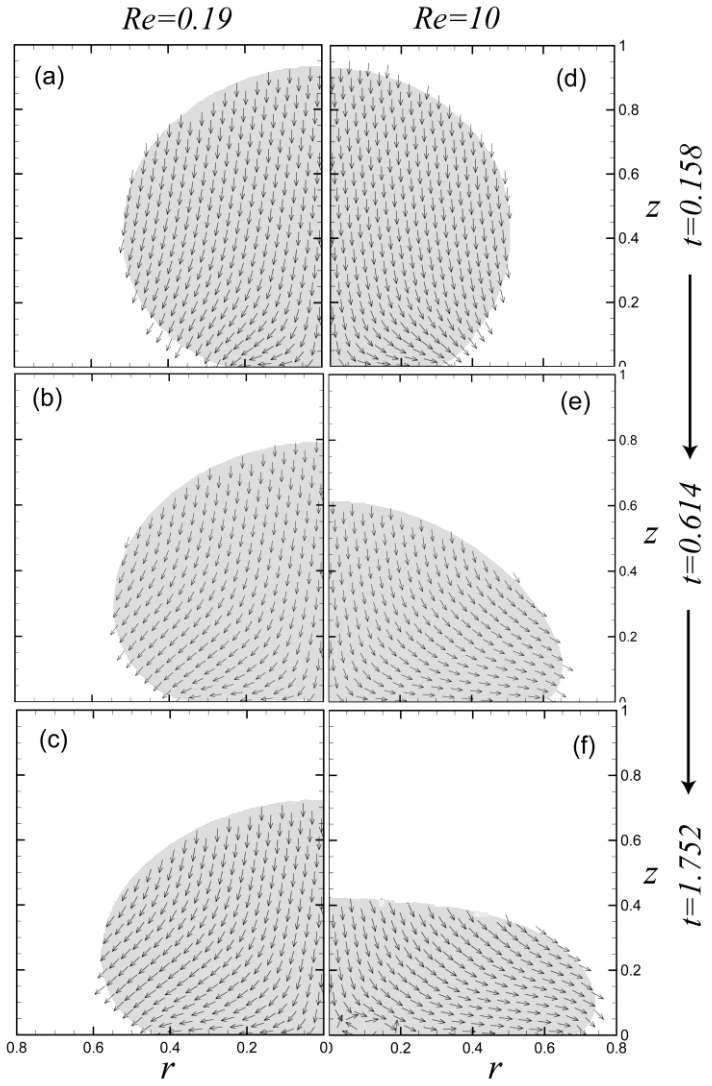

Figure 5.14: Velocity vectors within the droplet for impact computations with Reynold's numbers 0.19 (left - a, b, and c) and 10 (right- d, e, and f). The images are shown at the same times - 0.158 (top), 0.614 (middle), and 1.752 (bottom). Grey shading indicates the interior of the droplet.

All other parameters except the fluid viscosity are the same for the two computations.

The lower Reynolds number problem clearly shows less spreading and less droplet

flattening at times t = 0.614 and 1.752 after the initial impact has occurred. The higher Re

case not only spreads more than the low Re case, but it also spreads more rapidly along the substrate surface.

CHAPTER 6

CONCLUSIONS

6.1. Thermal Analysis Conclusions

A two-part thermal analysis was conducted to determine if the spreading process could be modeled as isothermal with a uniform temperature. The first part, section 3.1, covered scaling analyses used to approximate the various time scales of the impingement and the spreading processes. The stokes number calculated by Taltavull et al. (2016) indicated that the volcanic ash particle will collide with solid surfaces, given that the particle is larger than about 1 μm. The conduction-convection time scale ratio Ω was of order unity, so a more detailed analysis of temperature uniformity within the particle was conducted. The spreading-conduction time scale ratio *S* was much less than unity, which indicated that the spreading process occurs much more quickly than the thermal diffusion process, so that thermal effects can be ignored during droplet spreading simulations.

A Crank-Nicholson scheme was used to model the thermal response of the volcanic ash particle as it flowed through a GTE. The results showed that for particles less than 30 μm in diameter the temperature profile was uniform within 1% of the peak GTE temperature. The assumption of a uniform temperature profile was therefore justified for simulation purposes.

6.2. Droplet Impingement Conclusions

Small volcanic ash particles (with diameter from 3-30 μm) can be suspended in the atmosphere for periods of several weeks following a volcanic eruption. Jet aircraft flying through volcanic ash clouds ingest suspended particles into their gas turbine engines. These small particles can heat up and melt in the combustion portion of the engine, and then deposit on the downstream sections of the engine. Such deposits are of particular concern when they block film cooling holes on the turbine blades, leading the blades to heat up and the material to fail. Scaling studies of molten volcanic ash particle impingement in gas turbine engines indicate that this collision occurs at high Weber numbers (We = O(1000)) but at low droplet Reynolds numbers (Re = O(0.1-1)). A survey of the literature on droplet impingement on flat surfaces reveals that nearly all existing work was done for high droplet Reynolds numbers, and does not adequately capture the parameter range involved in the volcanic ash droplet impingement problem.

The current thesis presents a computational study of droplet impingement at high Weber number (We = 2776) and at relatively low Reynolds number ($0.05 \leq Re \leq 10$). This Reynolds number range was selected because it extends into the range of interest for molten volcanic ash impingement while also extending up into the bottom part of the range covered by previous moderate Re studies. The computations were conducted using an axisymmetric finite-volume approach with the combined level-set volume-of-fluid method used for interface tracking. Validation of the computations was performed by comparing predictions for contact radius variable with time to experimental data from Gordillo et al. (2018) for Reynold's numbers of $0.11 \leq Re \leq 7$ and experimental data

Rioboo et al. (2002) for Reynolds number of 9. The comparison of the computational predictions with the Gordillo et al. data was good for short times, but the presence of viscoelastic effects caused a spreading of the droplet to terminate prematurely (Gordillo et al., 2018). The Rioboo et al. (2002) data compared well with our computational predictions. The results were also compared over short times to the inviscid-flow analytical solution of Philippe et al. (2016), which seems to form a high Re bound for the data. At all Re values examined, the contact radius is observed to increase in proportion to the square root of time for short times after impact, in agreement with the Philippe et al. (2016) prediction. In general, the results show that the droplet spreads less rapidly, and reaches a smaller value of the maximum spread radius, as the Reynolds number decreases.

The computational results were used to examine the time and spatial variation of the kinetic energy and dissipation rate, as well as the time variation of the potential energy of the droplet. The dissipation rate decreases with increase in Reynolds number. At low Re the dissipation rate occurs throughout middle part of the droplet, but as Re approaches moderate values (~10) the dissipation rate becomes increasingly dominated by the region around the contact line. Spatial patterns of dissipation rate differ significantly from assumptions made in high Reynolds number approximate models (Kim & Chun, 2001), which typically assume that all dissipation occurs in a thin boundary layer underneath the essentially inviscid droplet flow. Droplet kinetic energy increases with Reynolds number, corresponding with the observed decrease in dissipation rate. The droplet potential energy was found to decrease with increase in Reynolds number in the

computed data. This trend was also observed in the experimental data of Gordillo et al. (2018).

The computed droplet shape was shown to be well approximated by a truncated sphere throughout the low Reynolds number impingement process. The axial velocity was found to be nearly independent of radius within the central part of the droplet, from which it follows that the radial velocity increases linearly with radius. The radial velocity profile was shown to fit closely to a log-normal form, from which the axial velocity profile was shown to be proportional to the cumulative probability distribution function, which can be written in terms of the complementary error function. The velocity profiles were shown to approach the form proposed by Madejski (1976) at long times, in which the radial velocity varies linearly in height z and the axial velocity varies quadratically in z.

6.3. Future Work and Applications

We have presented a work that assesses the fundamentals of low Reynolds number droplet impingement and how that relates to volcanic ash being ingested into a GTE. Moving forward there are several options to further advance the understanding of low Reynolds number droplet impingement. First, more experimentation that addresses a low Reynolds number should be conducted. Visser et al. (2012) was able to develop a micro sized droplet generater that could produce high speeds but was limited to low viscosity fluids. Gordillo et al. (2018) was able to produce a low Reynolds number but used a viscoelastic fluid which contributed to experimental uncertainty. Conducting an

experiment that overcomes the issues encountered by Gordillo et al. (2018) and Visser et al. (2012) would be a very useful dataset for modeling purposes. A second future work could be the development of an analytical spreading model applicable to low Reynolds numbers in conjunction with new experimental data.

The application of this work was laid out such that it pertains to volcanic ash ingestion in GTE. The premise for this choice was that if the spreading process of low Reynolds number droplets can be better understood then we can better design surface coating and engine components to mitigate ash build up. The study of the effect of volcanic ash on thermal barrier coatings is fairly extensive (Arai et al., 2019; Cai et al., 2016; Mechnich et al., 2011; Naraparaju et al., 2018; Schulz & Braue, 2013). Thermal barrier coatings are used to increase engine component life span and resilience against particulate matter. Our findings will help inform future researchers who attempt to model the process as the volcanic ash melts and spreads along an engine surface.

References

Abuku, M., Janssen, H., Poesen, J., & Roels, S. (2009). Impact, absorption and evaporation of raindrops on building facades. *Building and Environment*, *44*(1), 113–124. https://doi.org/10.1016/j.buildenv.2008.02.001

Afkhami, S., Zaleski, S., & Bussmann, M. (2009). A mesh-dependent model for applying dynamic contact angles to VOF simulations. *Journal of Computational Physics*, *228*(15), 5370–5389. https://doi.org/10.1016/j.jcp.2009.04.027

Alavi, S., Passandideh-Fard, M., & Mostaghimi, J. (2012). Simulation of semi-molten particle impacts including heat transfer and phase change. *Journal of Thermal Spray Technology*, *21*(6), 1278–1293. https://doi.org/10.1007/s11666-012-9804-8

Almohammadi, H., & Amirfazli, A. (2017). Asymmetric Spreading of a Drop upon Impact onto a Surface. *Langmuir*, *33*(23), 5957–5964. https://doi.org/10.1021/acs.langmuir.7b00704

Angell, C. A. (1991). Relaxation in liquids, polymers and plastic crystals — strong/fragile patterns and problems. *Journal of Non-Crystalline Solids*, *131–133*, 13–31. https://doi.org/https://doi.org/10.1016/0022-3093(91)90266-9

Angell, C. A. (1996). The glass transition. *Current Opinion in Solid State and Materials Science*, *1*(4), 578–585. https://doi.org/https://doi.org/10.1016/S1359-0286(96)80076-3

Antonini, C., Innocenti, M., Horn, T., Marengo, M., & Amirfazli, A. (2011). Understanding the effect of superhydrophobic coatings on energy reduction in anti-icing systems. *Cold Regions Science and Technology*, *67*, 58–67. https://doi.org/10.1016/j.coldregions.2011.02.006

Arai, M., Fukushima, Y., & Ito, K. (2019). Numerical Simulation of Volcanic Ash Infiltration into Thermal Barrier Coatings. *Key Engineering Materials*, *827*, 367–372. https://doi.org/10.4028/www.scientific.net/KEM.827.367

Attané, P., Girard, F., & Morin, V. (2007). An energy balance approach of the dynamics of drop impact on a solid surface. *Physics of Fluids*, *19*(1). https://doi.org/10.1063/1.2408495

Attinger, D., Zhao, Z., & Poulikakos, D. (2000). An experimental study of molten microdroplet surface deposition and solidification: Transient behavior and wetting angle dynamics. *Journal of Heat Transfer*, *122*(3), 544–556. https://doi.org/10.1115/1.1287587

Bagdassarov, N., & Dingwell, D. (1994). Thermal properties of vesicular rhyolite. *Journal of Volcanology and Geothermal Research*, *60*(2), 179–191. https://doi.org/10.1016/0377-0273(94)90067-1

Baker, D. R. (1996). Granitic melt viscosities; empirical and configurational entropy

models for their calculation. *American Mineralogist*, *81*(1–2), 126–134. https://doi.org/10.2138/am-1996-1-216

Baker, L. J., Pilch, M., & Tarbell, W. W. (1988). Droplet structure interactions in direct containment heating. *Transactions of the American Nuclear Society*, 361–363. http://inis.iaea.org/search/search.aspx?orig_q=RN:20085876

Banine, V. Y., Koshelev, K. N., & Swinkels, G. H. P. M. (2011). Physical processes in EUV sources for microlithography. *Journal of Physics D: Applied Physics*, *44*(25). https://doi.org/10.1088/0022-3727/44/25/253001

Bechtel, S. E., Bogy, D. B., & Talke, F. E. (1981). Impact of a Liquid Drop Against a Flat Surface. *IBM Journal of Research and Development*, *25*(6), 963–971. https://doi.org/10.1147/rd.256.0963

Bergeron, V., Bonn, D., Martin, J. Y., & Vovelle, L. (2000). Controlling droplet deposition with polymer additives. *Nature*, *405*, 772–775. https://doi.org/10.1038/35015525

Bertagnolli, M., Marchese, M., Jacucci, G., Doltsinis, I. St., & Noelting, S. (1994). Modelling the Impact of Particles on a Rigid Substrate under Plasma Spraying Conditions. *Flash Reaction Processes*, 239–263. https://doi.org/10.1007/978-94-011-0309-1_9

Blake, T. D., Bracke, M., & Shikhmurzaev, Y. D. (1999). Experimental evidence of nonlocal hydrodynamic influence on the dynamic contact angle. *Physics of Fluids*, *11*(8), 1995–2007. https://doi.org/10.1063/1.870063

Bonilla, C. (2012). *The Effect of Particle Size and Film Cooling on Nozzle Guide Vane Deposition* [The Ohio State University]. https://doi.org/10.1115/1.4007057

Bottinga. Y, W. (1972). The viscosity of magmatic silicate: a model for calculation. In *American Journal of Science* (Issue 272, pp. 438–475).

Bravo, L., Wijeyakulasuriya, S., Pomraning, E., Senecal, P. K., & Kweon, C.-B. (2016). Large Eddy Simulation of High Reynolds Number Nonreacting and Reacting JP-8 Sprays in a Constant Pressure Flow Vessel With a Detailed Chemistry Approach. *Journal of Energy Resources Technology*, *138*(3). https://doi.org/10.1115/1.4032901

Burzynski, D. A., & Bansmer, S. E. (2018). Droplet splashing on thin moving films at high Weber numbers. *International Journal of Multiphase Flow*, *101*, 202–211. https://doi.org/10.1016/j.ijmultiphaseflow.2018.01.015

Burzynski, D. A., & Bansmer, S. E. (2019). Role of surrounding gas in the outcome of droplet splashing. *Physical Review Fluids*, *4*(7), 1–10. https://doi.org/10.1103/PhysRevFluids.4.073601

Bussmann, M., Chandra, S., & Mostaghimi, J. (2000). Modeling the splash of a droplet impacting a solid surface. *Physics of Fluids*, *12*(12), 3121–3132.

https://doi.org/10.1063/1.1321258

Büttner, R., Zimanowski, B., Blumm, J., & Hagemann, L. (1998). Thermal conductivity of a volcanic rock material (olivine-melilitite) in the temperature range between 288 and 1470 K. *Journal of Volcanology and Geothermal Research*, *80*(3–4), 293–302. https://doi.org/10.1016/S0377-0273(97)00050-4

Cai, C., Chang, S., Zhou, Y., Yang, L., Zhou, G., & Wang, Y. (2016). Microstructure characteristics of EB-PVD YSZ thermal barrier coatings corroded by molten volcanic ash. *Surface & Coatings Technology*, *286*(C), 49–56. https://doi.org/10.1016/j.surfcoat.2015.12.003

Carrigan, C., & McBirney, A. (1997). Comment on "Experimental determination of the thermal conductivity of molten CaMgSi 2 O 6 and the transport of heat through magmas" by Don Snyder, Elizabeth Gier, and Ian Carmichael. *Journal of Geophysical Research: Solid Earth*, *102*(B7), 15077–15080. https://doi.org/10.1029/97jb00650

Chandra, S., & Avedisian, C. T. (1991). On the collision of a droplet with a solid surface. *Proceedings of the Royal Society A: Mathematical, Physical and Engineering Sciences*, *432*(1884), 13–41. https://doi.org/10.1098/rspa.1991.0002

Chen, W. R., & Zhao, L. R. (2015). Review - Volcanic Ash and its Influence on Aircraft Engine Components. *Procedia Engineering*, *99*, 795–803. https://doi.org/10.1016/j.proeng.2014.12.604

Choi, W., Tuteja, A., Mabry, J. M., Cohen, R. E., & McKinley, G. H. (2009). A modified Cassie-Baxter relationship to explain contact angle hysteresis and anisotropy on non-wetting textured surfaces. *Journal of Colloid and Interface Science*, *339*(1), 208–216. https://doi.org/10.1016/j.jcis.2009.07.027

Clanet, C., Béguin, C., Richard, D., & Quéré, D. (2004). Maximal deformation of an impacting drop. *Journal of Fluid Mechanics*, *517*, 199–208. https://doi.org/10.1017/S0022112004000904

Corrigan, R., & DeMiglio, R. (1985). *Effects of precipitation on wind turbine performance.* https://doi.org/NASA-TM-86986

Croce, R., Griebel, M., & Schweitzer, M. A. (2010). Numerical simulation of bubble and droplet deformation by a level set approach with surface tension in three dimensions. *International Journal for Numerical Methods in Fluids*, *62*(9), 963–993. https://doi.org/10.1002/fld.2051

Dacre, H. F., Grant, A. L. M., & Johnson, B. T. (2013). Aircraft observations and model simulations of concentration and particle size distribution in the Eyjafjallajökull volcanic ash cloud. *Atmospheric Chemistry and Physics*, *13*(3), 1277–1291. https://doi.org/10.5194/acp-13-1277-2013

David, R., & Neumann, A. W. (2011). Calculation of contact angle hysteresis on

chemically heterogeneous surfaces. *Abstracts of Papers of the American Chemical Society*, *241*, 351–355.

De Gennes, P. G. (1985). Wetting: Statics and dynamics. *Reviews of Modern Physics*, *57*(3), 827–863. https://doi.org/10.1103/RevModPhys.57.827

Dean, J., Taltavull, C., & Clyne, T. W. (2016). Influence of the composition and viscosity of volcanic ashes on their adhesion within gas turbine aeroengines. *Acta Materialia*, *109*, 8–16. https://doi.org/10.1016/j.actamat.2016.02.011

Dunn, M. G. (2012). Operation of Gas Turbine Engines in an Environment Contaminated with Volcanic Ash. *Journal of Turbomachinery*, *134*(5), 1–18. https://doi.org/10.1115/1.4006236

Dussan, E. B. (1979). On the Spreading of Liquids on Solid Surfaces: Static and Dynamic Contact Lines. *Annual Review of Fluid Mechanics*, *11*(1), 371–400. https://doi.org/10.1146/annurev.fl.11.010179.002103

Dussan, E. B., & Dussan V., E. B. (1976). The moving contact line: the slip boundary condition. *Journal of Fluid Mechanics*, *77*(4), 665–684. https://doi.org/10.1017/S0022112076002838

Eggers, J., Fontelos, M. A., Josserand, C., & Zaleski, S. (2010). Drop dynamics after impact on a solid wall: Theory and simulations. *Physics of Fluids*, *22*(6). https://doi.org/10.1063/1.3432498

Engel, O. G. (1955). Waterdrop collisions with solid surfaces. *Journal of Research of the National Bureau of Standards*, *54*(5), 281. https://doi.org/10.6028/jres.054.033

Eriksson, R., Hayashi, M., & Seetharaman, S. (2003). Thermal Diffusivity Measurements of Liquid Silicate Melts. *International Journal of Thermophysics*, *24*(3), 785–797. https://doi.org/10.1023/A:1024048518617

Extrand, C. W., & Kumagai, Y. (1996). Contact angles and hysteresis on soft surfaces. *Journal of Colloid and Interface Science*, *184*(1), 191–200. https://doi.org/10.1006/jcis.1996.0611

Eyring, H., Henderson, D., & Stover, B. J. (1982). *Statistical mechanics and dynamics* (2nd ed.). John Wiley eds.

Fu, S. P., Sahu, R. P., Diaz, E., Robles, J. R., Chen, C., Rui, X., Klie, R. F., Yarin, A. L., & Abiade, J. T. (2016). Dynamic Study of Liquid Drop Impact on Supercooled Cerium Dioxide: Anti-Icing Behavior. *Langmuir*, *32*(24), 6148–6162. https://doi.org/10.1021/acs.langmuir.6b00847

Gao, X., & Li, R. (2014). Spread and recoiling of liquid droplets impacting solid surfaces. *AIChE Journal*, *60*(7), 2683–2691. https://doi.org/10.1002/aic.14440

Giordano, D., Romano, C., Dingwell, D., Poe, B., & Behrens, H. (2004). The combined

effects of water and fluorine on the viscosity of silicic magmas. *Geochimica et Cosmochimica Acta*, *68*, 5159–5168. https://doi.org/10.1016/j.gca.2004.08.012

Giordano, D., Romano, C., Papale, P., & Dingwell, D. (2004). The viscosity of trachytes, and comparison with basalts, phonolites, and rhyolites. *Chemical Geology*, *213*, 49–61. https://doi.org/10.1016/j.chemgeo.2004.08.032

Giordano, D., Russell, J. K., & Dingwell, D. B. (2008). Viscosity of magmatic liquids: A model. *Earth and Planetary Science Letters*, *271*(1–4), 123–134. https://doi.org/10.1016/j.epsl.2008.03.038

Gordillo, L., Sun, T. P., & Cheng, X. (2018). Dynamics of drop impact on solid surfaces: Evolution of impact force and self-similar spreading. *Journal of Fluid Mechanics*, *840*, 190–214. https://doi.org/10.1017/jfm.2017.901

Griebel, M., & Klitz, M. (2017). CLSVOF as a fast and mass-conserving extension of the level-set method for the simulation of two-phase flow problems. *Numerical Heat Transfer, Part B: Fundamentals*, *71*(1), 1–36. https://doi.org/10.1080/10407790.2016.1244400

Gu, S., & Kamnis, S. (2009). Bonding mechanism from the impact of thermally sprayed solid particles. *Metallurgical and Materials Transactions A: Physical Metallurgy and Materials Science*, *40*(11), 2664–2674. https://doi.org/10.1007/s11661-009-9959-1

Guffanti, M., Casadevall, T., & Budding, K. (2010). Encounters of Aircraft with Volcanic Ash Clouds: A Compilation of Known Incidents, 1953–2009. In *U.S. Geological Survey* (Vol. 14, Issue 3). https://doi.org/10.1007/BF00932611

Guffanti, M., Mayberry, G. C., Casadevall, T. J., & Wunderman, R. (2009). Volcanic hazards to airports. *Natural Hazards*, *51*(2), 287–302. https://doi.org/10.1007/s11069-008-9254-2

Guo, Y., Lian, Y., & Sussman, M. (2016). Investigation of drop impact on dry and wet surfaces with consideration of surrounding air. *Physics of Fluids*, *28*(7). https://doi.org/10.1063/1.4958694

Haller, K. K., Ventikos, Y., Poulikakos, D., & Monkewitz, P. (2002). Computational study of high-speed liquid droplet impact. *Journal of Applied Physics*, *92*(5), 2821–2828. https://doi.org/10.1063/1.1495533

Hess, K.-U. U., & Dingwell, D. B. (1996). Viscosities of hydrous leucogranitic melts: A non-Arrhenian model. *American Mineralogist*, *81*(9–10), 1297–1300. https://doi.org/10.1016/0016-7037(82)90381-7

Hicks, P. D., & Purvis, R. (2010). Air cushioning and bubble entrapment in three-dimensional droplet impacts. *Journal of Fluid Mechanics*, *649*, 135–163. https://doi.org/10.1017/S0022112009994009

Hirt, C. W., & Nichols, B. D. (1979). Volume of Fluid (VOF) Method for the Dynamics of Free Boundaries. *Journal of Computational Physics*, *42*(3), 357–366. https://doi.org/10.1007/s40998-018-0069-1

Hobiger, M., Sonder, I., Büttner, R., & Zimanowski, B. (2011). Viscosity characteristics of selected volcanic rock melts. *Journal of Volcanology and Geothermal Research*, *200*(1–2), 27–34. https://doi.org/10.1016/j.jvolgeores.2010.11.020

Hoffman, R. L. (1975). A study of the advancing interface. I. Interface shape in liquid-gas systems. *Journal of Colloid And Interface Science*, *50*(2), 228–241. https://doi.org/10.1016/0021-9797(75)90225-8

Holmgren, H. (2017). *Modelling of Moving Contact Lines in Two-Phase Flows*. http://urn.kb.se/resolve?urn=urn:nbn:se:uu:diva-329059

Horat, K., & Simmons, G. (1969). THERMAL CONDUCTIVITY OF ROCK-FORMING MINERALS a. *Earth and Planetary Science Letters*, *6*, 359–368.

Horwell, C. J., & Baxter, P. J. (2006). The respiratory health hazards of volcanic ash: A review for volcanic risk mitigation. *Bulletin of Volcanology*, *69*(1), 1–24. https://doi.org/10.1007/s00445-006-0052-y

Hui, H., & Zhang, Y. (2007). Toward a general viscosity equation for natural anhydrous and hydrous silicate melts. *Geochimica et Cosmochimica Acta*, *71*, 403–416. https://doi.org/10.1016/j.gca.2006.09.003

Hulse-Smith, L., Mehdizadeh, N., & Chandra, S. (2005). Deducing drop size and impact velocity from circular bloodstains. *Journal of Forensic Sciences*, *50*(1). https://doi.org/10.1520/JFS2003224

Izbassarov, D., & Muradoglu, M. (2016). Effects of viscoelasticity on drop impact and spreading on a solid surface. *Physical Review Fluids*, *1*(2), 1–18. https://doi.org/10.1103/physrevfluids.1.023302

Jiang, T. S., Soo-Gun, O. H., & Slattery, J. C. (1979). Correlation for dynamic contact angle. *Journal of Colloid And Interface Science*, *69*(1), 74–77. https://doi.org/10.1016/0021-9797(79)90081-X

Ju, J., Yang, Z., Yi, X., & Jin, Z. (2019). Experimental investigation of the impact and freezing processes of a hot water droplet on an ice surface. *Physics of Fluids*, *31*(5). https://doi.org/10.1063/1.5094691

Kendall, G. E., & Rohsenow, W. M. (1978). Department of Mechanical Engineering Massachusetts Institute of Technology Sponsored by National Science Foundation D . S . R . Project No . 85694 March 1978 Department of Mechanical Engineering Massachusetts Institute of Technology Cambridge , Massachuse. *Contract*, *85694*.

Kim, H., & Chun, J. (2001). The recoiling of liquid droplets upon collision with solid surfaces. *Physics of Fluids*, *13*(3), 643–659. https://doi.org/10.1063/1.1344183

Kim, J. (2007). Spray cooling heat transfer: The state of the art. *International Journal of Heat and Fluid Flow*, *28*(4), 753–767. https://doi.org/10.1016/j.ijheatfluidflow.2006.09.003

Kim, S. J., Kim, J., Moon, M. W., Lee, K. R., & Kim, H. Y. (2013). Experimental study of drop spreading on textured superhydrophilic surfaces. *Physics of Fluids*, *25*(9). https://doi.org/10.1063/1.4821985

Kolinski, J. M., Rubinstein, S. M., Mandre, S., Brenner, M. P., Weitz, D. A., & Mahadevan, L. (2012). Skating on a film of air: Drops impacting on a surface. *Physical Review Letters*, *108*(7), 1–5. https://doi.org/10.1103/PhysRevLett.108.074503

Kondo, S., Mamori, H., Fukushima, N., Fukudome, K., & Yamamoto, M. (2018). Numerical simulation of solidification phenomena of single molten droplet on flat plate using E-MPS method. *Journal of Fluid Science and Technology*, *13*(3), 1–8. https://doi.org/10.1299/jfst.2018jfst0013

Krawietz, T. R., Murray, D. K., & Haw, J. F. (1998). Alkali metal oxides, peroxides, and superoxides: A multinuclear MAS NMR study. *Journal of Physical Chemistry A*, *102*(45), 8779–8785. https://doi.org/10.1021/jp9823190

Krieger, I. (1953). *Direct Determination of the Flow Curves of Non-Newtonian Fluids. II. Shearing Rate in the Concentric Cylinder Viscometer*. *24*(2), 135–136.

Laan, N., De Bruin, K. G., Bartolo, D., Josserand, C., & Bonn, D. (2014). Maximum diameter of impacting liquid droplets. *Physical Review Applied*, *2*(4), 1–7. https://doi.org/10.1103/PhysRevApplied.2.044018

Lagubeau, G., Fontelos, M. A., Josserand, C., Maurel, A., Pagneux, V., & Petitjeans, P. (2012). Spreading dynamics of drop impacts. *Journal of Fluid Mechanics*, *713*, 50–60. https://doi.org/10.1017/jfm.2012.431

Lara, C., Pascual, M. J., Prado, M. O., & Durán, A. (2004). Sintering of glasses in the system RO-Al2O3-BaO- SiO2(R=Ca, Mg, Zn) studied by hot-stage microscopy. *Solid State Ionics*, *170*(3–4), 201–208. https://doi.org/10.1016/j.ssi.2004.03.009

Lee, J. B., Derome, D., Guyer, R., & Carmeliet, J. (2016). Modeling the Maximum Spreading of Liquid Droplets Impacting Wetting and Nonwetting Surfaces. *Langmuir*, *32*(5), 1299–1308. https://doi.org/10.1021/acs.langmuir.5b04557

Legendre, D., & Maglio, M. (2015). Comparison between numerical models for the simulation of moving contact lines. *Computers and Fluids*, *113*, 2–13. https://doi.org/10.1016/j.compfluid.2014.09.018

Li, N., Zhou, Q., Chen, X., Xu, T., Hui, S., & Zhang, D. (2008). Liquid drop impact on solid surface with application to water drop erosion on turbine blades, Part I: Nonlinear wave model and solution of one-dimensional impact. *International Journal of Mechanical Sciences*, *50*(10–11), 1526–1542.

https://doi.org/10.1016/j.ijmecsci.2008.08.001

Lim, T., Han, S., Chung, J., Chung, J. T., Ko, S., & Grigoropoulos, C. P. (2009). Experimental study on spreading and evaporation of inkjet printed pico-liter droplet on a heated substrate. *International Journal of Heat and Mass Transfer*, *52*(1–2), 431–441. https://doi.org/10.1016/j.ijheatmasstransfer.2008.05.028

Liu, Y., Tan, P., & Xu, L. (2013). Compressible air entrapment in high-speed drop impacts on solid surfaces. *Journal of Fluid Mechanics*, R9-1-R9-12. https://doi.org/10.1017/jfm.2012.583

Lofgren, G. (1971). Spherulitic textures in glassy and crystalline rocks. *Journal of Geophysical Research*, *76*(23), 5635–5648. https://doi.org/10.1029/jb076i023p05635

Macosko, C. (1994). *Rheology: Principles, Measurements and Applications* (1st ed.). Wiley/VCH.

Mani, M., Mandre, S., & Brenner, M. P. (2010). Events before droplet splashing on a solid surface. *Journal of Fluid Mechanics*, *647*, 163–185. https://doi.org/10.1017/S0022112009993594

Manzello, S. L., & Yang, J. C. (2002). On the collision dynamics of a water droplet containing an additive on a heated solid surface. *Proceedings of the Royal Society A: Mathematical, Physical and Engineering Sciences*, *458*(2026), 2417–2444. https://doi.org/10.1098/rspa.2002.0980

McDonald, A., Lamontagne, M., Moreau, C., & Chandra, S. (2006). Impact of plasma-sprayed metal particles on hot and cold glass surfaces. *Thin Solid Films*, *514*(1–2), 212–222. https://doi.org/10.1016/j.tsf.2006.03.010

Mechnich, P., Braue, W., & Schulz, U. (2011). High-Temperature Corrosion of EB-PVD Yttria Partially Stabilized Zirconia Thermal Barrier Coatings with an Artificial Volcanic Ash Overlay. *American Ceramic Society. Journal of the American Ceramic Society*, *94*(3), 925. https://doi.org/10.1111/j.1551-2916.2010.04166.x

Merriman, J. D., Whittington, A. G., Hofmeister, A. M., Nabelek, P. I., & Benn, K. (2013). Thermal transport properties of major Archean rock types to high temperature and implications for cratonic geotherms. *Precambrian Research*, *232*, 358–372. https://doi.org/10.1016/j.precamres.2013.05.009

Mielke, P., Weinert, S., Bignall, G., & Sass, I. (2016). Thermo-physical rock properties of greywacke basement rock and intrusive lavas from the Taupo Volcanic Zone, New Zealand. *Journal of Volcanology and Geothermal Research*, *324*, 179–189. https://doi.org/10.1016/j.jvolgeores.2016.06.002

Mishchenko, L., Hatton, B., Bahadur, V., Taylor, J. A., Krupenkin, T., & Aizenberg, J. (2010). Design of ice-free nanostructured surfaces based on repulsion of impacting water droplets. *ACS Nano*, *4*(12), 7699–7707. https://doi.org/10.1021/nn102557p

Murase, T., & McBirney, A. R. (1973). Properties of some common igneous rocks and their melts at high temperatures. *Bulletin of the Geological Society of America*, *84*(11), 3563–3592. https://doi.org/10.1130/0016-7606(1973)84<3563:POSCIR>2.0.CO;2

Murugan, M., Ghoshal, A., Walock, M., Nieto, A., Bravo, L., Pegg, R. T., & Rowe, C. (2017). *MICROSTRUCTURE BASED MATERIAL-SAND PARTICULATE INTERACTIONS AND ASSESSMENT OF COATINGS FOR HIGH TEMPERATURE TURBINE BLADES*.

Naraparaju, R., Lau, H., Lange, M., Fischer, C., Kramer, D., Schulz, U., & Weber, K. (2018). Integrated testing approach using a customized micro turbine for a volcanic ash and CMAS related degradation study of thermal barrier coatings. *Surface & Coatings Technology*, *337*, 198–208. https://doi.org/10.1016/j.surfcoat.2018.01.030

Nishi, T., Ohta, H., Sukenaga, S., & Shibata, H. (2018). Estimation of thermal conductivity of silicate melts using three-dimensional thermal resistor network model. *Journal of Non-Crystalline Solids*, *482*(September 2017), 9–13. https://doi.org/10.1016/j.jnoncrysol.2017.11.014

Ogawa, H., Ohta, H., & Waseda, Y. (1993). Thermal diffusivity measurement of LiNbO3 melts doped with MgO by the laser flash method. *Journal of Crystal Growth*, *133*(3–4), 255–260. https://doi.org/10.1016/0022-0248(93)90162-P

Ojovan, M. I. (2008). Viscosity and Glass Transition in Amorphous Oxides. *Advances in Condensed Matter Physics*, *2008*, 1–23. https://doi.org/10.1155/2008/817829

Onorato, P. I. K., Uhlmann, D. R., & Simonds, C. H. (1978). The thermal history of the Manicouagan Impact Melt Sheet, Quebec. *Journal of Geophysical Research: Solid Earth*, *83*(B6), 2789–2798. https://doi.org/10.1029/JB083iB06p02789

Oochi, M., Koshizuka, S., & Sakai, M. (2010). Explicit MPS Algorithm for Free Surface Flow Analysis. *Transactions of the Japan Society for Computational Engineering and Science*, *2010*, 20100013.

Parker, W. J., Jenkins, R. J., Butler, C. P., & Abbott, G. L. (1961). Flash Method of Determining Thermal Diffusivity. *Journal of Applied Physics*, *32*(9), 1679–1684. https://doi.org/10.1007/978-94-007-2739-7_100240

Pasandideh-Fard, M., Chandra, S., & Mostaghimi, J. (2002). A three-dimensional model of droplet impact and solidification. *International Journal of Heat and Mass Transfer*, *45*(11), 2229–2242. https://doi.org/10.1016/S0017-9310(01)00336-2

Pasandideh-Fard, M., Qiao, Y. M., Chandra, S., & Mostaghimi, J. (1996). Capillary effects during droplet impact on a solid surface. *Physics of Fluids*, *8*(3), 650–659. https://doi.org/10.1063/1.868850

Philippi, J., Lagrée, P. Y., & Antkowiak, A. (2016). Drop impact on a solid surface: Short-time self-similarity. *Journal of Fluid Mechanics*, *795*, 96–135.

https://doi.org/10.1017/jfm.2016.142

Pyle, D. M. (1989). The thickness, volume and grainsize of tephra fall deposits. *Bulletin of Volcanology*, *51*(1), 1–15. https://doi.org/10.1007/BF01086757

Rein, M. (1993). *Phenomena of liquid drop impact on solid and liquid surfaces*. *12*, 61–93. https://doi.org/10.1016/0169-5983(93)90106-K

Riboux, G., & Gordillo, J. M. (2014). Experiments of drops impacting a smooth solid surface: A model of the critical impact speed for drop splashing. *Physical Review Letters*, *113*(2), 1–5. https://doi.org/10.1103/PhysRevLett.113.024507

Richard, D., & Quéré, D. (2000). Bouncing water drops. *Europhysics Letters*, *50*(6), 769–775. https://doi.org/10.1209/epl/i2000-00547-6

Rioboo, R., Marengo, M., & Tropea, C. (2002). Time evolution of liquid drop impact onto solid, dry surfaces. *Experiments in Fluids*, *33*(1), 112–124. https://doi.org/10.1007/s00348-002-0431-x

Roisman, I. V., Berberović, E., & Tropea, C. (2009). Inertia dominated drop collisions. I. On the universal flow in the lamella. *Physics of Fluids*, *21*(5). https://doi.org/10.1063/1.3129282

Roisman, I. V., Rioboo, R., & Tropea, C. (2002). Normal impact of a liquid drop on a dry surface: Model for spreading and receding. *Proceedings of the Royal Society A: Mathematical, Physical and Engineering Sciences*, *458*(2022), 1411–1430. https://doi.org/10.1098/rspa.2001.0923

Russell, J. K., Giordano, D., & Dingwell, D. B. (2003). High-temperature limits on viscosity of non-Arrhenian silicate melts. *American Mineralogist*, *88*(8–9), 1390–1394. https://doi.org/10.2138/am-2003-8-924

Saleh, M., Luzin, V., & Spencer, K. (2014). Analysis of the residual stress and bonding mechanism in the cold spray technique using experimental and numerical methods. *Surface and Coatings Technology*, *252*, 15–28. https://doi.org/10.1016/j.surfcoat.2014.04.059

Schiaffino, S., & Sonin, A. A. (1997a). Molten droplet deposition and solidification at low Weber numbers. *Physics of Fluids*, *9*(11), 3172–3187. https://doi.org/10.1063/1.869434

Schiaffino, S., & Sonin, A. A. (1997b). On the theory for the arrest of an advancing molten contact line on a cold solid of the same material. *Physics of Fluids*, *9*(8), 2227–2233. https://doi.org/10.1063/1.869345

Schmidt, P., & Knauss, G. (1976). Prallzerstäubung von Flüssigkeiten bei Nichtbenetzung. *Chemie Ingenieur Technik*, *48*(7), 659. https://doi.org/10.1002/cite.330480724

Schulz, U., & Braue, W. (2013). Degradation of La 2 Zr 2 O 7 and other novel EB-PVD thermal barrier coatings by CMAS (CaO-MgO-Al 2 O 3 -SiO 2) and volcanic ash deposits. *Surface and Coatings Technology*, *235*(C). https://doi.org/10.1016/j.surfcoat.2013.07.029

Scopigno, T., Ruocco, G., Sette, F., & Monaco, G. (2003). Is the Fragility of a Liquid Embedded in the Properties of Its Glass? *Science*, *302*(5646), 849 LP – 852. https://doi.org/10.1126/science.1089446

Sethian, J. A. (1999). *Level Set Methods and Fast Marching Methods: Evolving Interfaces in Computational Geometry, Fluid Mechanics, Computer Vision, and Materials Science* (2nd ed.). Cambridge University Press.

Shakeri, S., & Chandra, S. (2002). Splashing of molten tin droplets on a rough steel surface. *International Journal of Heat and Mass Transfer*, *45*(23), 4561–4575. https://doi.org/https://doi.org/10.1016/S0017-9310(02)00170-9

Shaw, H. R. (1972). Viscosities of magmatic silicate liquids; an empirical method of prediction. In *American Journal of Science* (Vol. 272, Issue 9, pp. 870–893). https://doi.org/10.2475/ajs.272.9.870

Shikhmurzaev, Y. D. (1997). Moving contact lines in liquid/liquid/solid systems. *Journal of Fluid Mechanics*, *334*, 211–249. https://doi.org/10.1017/S0022112096004569

Shinoda, K., Kojima, Y., & Yoshida, T. (2005). In situ measurement system for deformation and solidification phenomena of yttria-stabilized zirconia droplets impinging on quartz glass substrate under plasma-spraying conditions. *Journal of Thermal Spray Technology*, *14*(4), 511–517. https://doi.org/10.1361/105996305X76531

Shinoda, K., & Murakami, H. (2010). Splat morphology of yttria-stabilized zirconia droplet deposited via hybrid plasma spraying. *Journal of Thermal Spray Technology*, *19*(3), 602–610. https://doi.org/10.1007/s11666-009-9460-9

Šikalo, Š., Wilhelm, H. D., Roisman, I. V., Jakirlić, S., & Tropea, C. (2005). Dynamic contact angle of spreading droplets: Experiments and simulations. *Physics of Fluids*, *17*(6), 1–13. https://doi.org/10.1063/1.1928828

Snyder, D., Gier, E., & Carmichael, I. (1994). Experimental determination of the thermal conductivity of molten CaMgSi2O6and the transport of heat through magmas. *Journal of Geophysical Research*, *99*(B8). https://doi.org/10.1029/94jb01018

Snyder, Don, Gier, E., & Carmichael, I. (1997). Reply. *JOURNAL OF GEOPHYSICAL RESEARCH*, *102*(B7), 15077–15080.

Son, Y., & Kim, C. (2009). Spreading of inkjet droplet of non-Newtonian fluid on solid surface with controlled contact angle at low Weber and Reynolds numbers. *Journal of Non-Newtonian Fluid Mechanics*, *162*(1–3), 78–87. https://doi.org/10.1016/j.jnnfm.2009.05.009

Sonder, I., Zimanowski, B., & Büttner, R. (2006). Non-Newtonian viscosity of basaltic magma. *Geophysical Research Letters*, *33*(2), 3–5. https://doi.org/10.1029/2005GL024240

Song, W., Hess, K.-U., Damby, D. E., Wadsworth, F. B., Lavallée, Y., Cimarelli, C., & Dingwell, D. B. (2014). Fusion characteristics of volcanic ash relevant to aviation hazards. *Geophysical Prospecting*, *April*, 6413–6419. https://doi.org/10.1002/2014GL061184.Received

Song, W., Lavallee, Y., Hess, K. U., Kueppers, U., Cimarelli, C., & Dingwell, D. B. (2016). Volcanic ash melting under conditions relevant to ash turbine interactions. *Nature Communications*, *7*, 1–10. https://doi.org/10.1038/ncomms10795

Song, W., Lavallée, Y., Wadsworth, F. B., Hess, K. U., & Dingwell, D. B. (2017). Wetting and Spreading of Molten Volcanic Ash in Jet Engines. *Journal of Physical Chemistry Letters*, *8*(8), 1878–1884. https://doi.org/10.1021/acs.jpclett.7b00417

Song, W., Yang, S., Fukumoto, M., Lavallée, Y., Lokachari, S., Guo, H., You, Y., & Dingwell, D. B. (2019). Impact interaction of in-flight high-energy molten volcanic ash droplets with jet engines. *Acta Materialia*, *171*, 119–131. https://doi.org/10.1016/j.actamat.2019.04.011

Speyer, R. F. (1994). *Thermal Analysis of Materials* (1st ed.). Marcel Dekker.

Stow, C. D., Hadfield, M. G., & Ziman, J. M. (1981). An experimental investigation of fluid flow resulting from the impact of a water drop with an unyielding dry surface. *Proceedings of the Royal Society of London. A. Mathematical and Physical Sciences*, *373*(1755), 419–441. https://doi.org/10.1098/rspa.1981.0002

Suli, L., Zhengying, W., Jun, D., Pei, W., & Bingheng, L. (2017). A Numerical Analysis on the Metal Droplets Impacting and Spreading out on the Substrate. *Rare Metal Materials and Engineering*, *46*(4), 893–898. https://doi.org/10.1016/s1875-5372(17)30118-2

Sun, D. L., & Tao, W. Q. (2010). A coupled volume-of-fluid and level set (VOSET) method for computing incompressible two-phase flows. *International Journal of Heat and Mass Transfer*, *53*(4), 645–655. https://doi.org/10.1016/j.ijheatmasstransfer.2009.10.030

Sussman, M., & Puckett, E. G. (2000). A Coupled Level Set and Volume-of-Fluid Method for Computing 3D and Axisymmetric Incompressible Two-Phase Flows. *Journal of Computational Physics*, *162*, 301–337. https://doi.org/10.1006/jcph.2000.6537

Taltavull, C., Dean, J., & Clyne, T. W. (2016). Adhesion of volcanic ash particles under controlled conditions and implications for their deposition in gas turbines. *Advanced Engineering Materials*, *18*(5), 803–813. https://doi.org/10.1002/adem.201500371

Tang, C., Qin, M., Weng, X., Zhang, X., Zhang, P., Li, J., & Huang, Z. (2017). Dynamics

of droplet impact on solid surface with different roughness. *International Journal of Multiphase Flow*, *96*, 56–69. https://doi.org/10.1016/j.ijmultiphaseflow.2017.07.002

Thornber, C. R., & Huebner, J. S. (1985). Dissolution of olivine in basaltic liquids: experimental observations and applications. *American Mineralogist*, *70*(9–10), 934–945.

Thoroddsen, S. T., Etoh, T. G., & Takehara, K. (2003). Air entrapment under an impacting drop. *Journal of Fluid Mechanics*, *478*, 125–134. https://doi.org/10.1017/S0022112002003427

Thoroddsen, S. T., Etoh, T. G., Takehara, K., Ootsuka, N., & Hatsukih, Y. (2005). The air bubble entrapped under a drop impacting on a solid surface. *Journal of Fluid Mechanics*, *545*, 203–212. https://doi.org/10.1017/S0022112005006919

van Dam, D. B., & Le Clerc, C. (2004). Experimental study of the impact of an ink-jet printed droplet on a solid substrate. *Physics of Fluids*, *16*, 3403–3414. https://doi.org/10.1063/1.1773551

van Manen, S. M., & Wallin, E. (2012). Ground temperature profiles and thermal rock properties at Wairakei, New Zealand. *Renewable Energy*, *43*, 313–321. https://doi.org/10.1016/j.renene.2011.11.032

Venkatesan, J., & Ganesan, S. (2019). Computational modeling of impinging viscoelastic droplets. *Journal of Non-Newtonian Fluid Mechanics*, *263*(September 2018), 42–60. https://doi.org/10.1016/j.jnnfm.2018.11.001

Vetere, F., Behrens, H., Holtz, F., & Neuville, D. (2006). Viscosity of andesitic melts—new experimental data and a revised calculation model. *Chemical Geology*, *228*, 233–245. https://doi.org/10.1016/j.chemgeo.2005.10.009

Visser, C. W., Frommhold, P. E., Wildeman, S., Mettin, R., Lohse, D., & Sun, C. (2015). Dynamics of high-speed micro-drop impact: Numerical simulations and experiments at frame-to-frame times below 100 ns. *Soft Matter*, *11*(9), 1708–1722. https://doi.org/10.1039/c4sm02474e

Visser, C. W., Tagawa, Y., Sun, C., & Lohse, D. (2012). Microdroplet impact at very high velocity. *Soft Matter*, *8*(41), 10732–10737. https://doi.org/10.1039/c2sm26323h

Vogel, A., Diplas, S., Durant, A. J., Azar, A. S., Sunding, M. F., Rose, W. I., Sytchkova, A., Bonadonna, C., Krüger, K., & Stohl, A. (2017). Reference data set of volcanic ash physicochemical and optical properties. *Journal of Geophysical Research: Atmospheres*, *122*(17), 9485–9514. https://doi.org/10.1002/2016JD026328

Vosteen, H., & Rudiger, S. (2003). *Influence of temperature on thermal conductivity , thermal capacity and thermal diffusivity for different types of rock*. *28*, 499–509. https://doi.org/10.1016/S1474-7065(03)00069-X

Walsh, W. S., Thole, K. A., & Joe, C. (2006). Effects of Sand Ingestion on the Blockage

of Film-Cooling Holes. *Volume 3: Heat Transfer, Parts A and B, 2006*, 81–90. https://doi.org/10.1115/GT2006-90067

Walzel, P. (1980). Zerteilgrenze beim Tropfenprall. *Chemie Ingenieur Technik*, *52*(4), 338–339. https://doi.org/10.1002/cite.330520412

Wang, Y., & Bourouiba, L. (2017). Drop impact on small surfaces: Thickness and velocity profiles of the expanding sheet in the air. *Journal of Fluid Mechanics*, *814*, 510–534. https://doi.org/10.1017/jfm.2017.18

Wildeman, S., Visser, C. W., Sun, C., & Lohse, D. (2016). On the spreading of impacting drops. *Journal of Fluid Mechanics*, *805*, 636–655. https://doi.org/10.1017/jfm.2016.584

Wilson, T. M., Stewart, C., Sword-Daniels, V., Leonard, G. S., Johnston, D. M., Cole, J. W., Wardman, J., Wilson, G., & Barnard, S. T. (2012). Volcanic ash impacts on critical infrastructure. *Physics and Chemistry of the Earth*, *45–46*, 5–23. https://doi.org/10.1016/j.pce.2011.06.006

Wirth, W., Storp, S., & Jacobsen, W. (1991). Mechanisms controlling leaf retention of agricultural spray solutions. *Pesticide Science*, *33*, 411–420. https://doi.org/10.1002/ps.2780330403

Worthington, B. A. M. (1876). *On the Forms assumed by Drops of Liquids falling vertically on a horizontal Plate*. 261–271.

Xiong, W., & Cheng, P. (2018). Numerical investigation of air entrapment in a molten droplet impacting and solidifying on a cold smooth substrate by 3D lattice Boltzmann method. *International Journal of Heat and Mass Transfer*, *124*, 1262–1274. https://doi.org/10.1016/j.ijheatmasstransfer.2018.04.056

Yokoi, K., Vadillo, D., Hinch, J., & Hutchings, I. (2009). Numerical studies of the influence of the dynamic contact angle on a droplet impacting on a dry surface. *Physics of Fluids*, *21*(7). https://doi.org/10.1063/1.3158468

Zable, J. L. (1977). Splatter during ink jet printing. *IBM Journal of Research and Development*, *21*, 315–320. https://doi.org/10.1147/rd.214.0315

Zhao, R., Zhang, Q., Tjugito, H., & Cheng, X. (2015). Granular impact cratering by liquid drops: Understanding raindrop imprints through an analogy to asteroid strikes. *Proceedings of the National Academy of Sciences of the United States of America*, *112*(2), 342–347. https://doi.org/10.1073/pnas.1419271112

Zhou, Q., Li, N., Chen, X., Xu, T., Hui, S., & Zhang, D. (2008). Liquid drop impact on solid surface with application to water drop erosion on turbine blades , Part II : Axisymmetric solution and erosion analysis. *International Journal of Mechanical Sciences*, *50*, 1543–1558. https://doi.org/10.1016/j.ijmecsci.2008.08.002